Spring 2019

Nanoscale Control of Metal Oxideand Carbonaceous Functional Materials

Benjamin W. Lamm

NANOSCALE CONTROL OF METAL OXIDE AND CARBONACEOUS FUNCTIONAL MATERIALS

by

Benjamin W Lamm

Bachelor of Arts
Illinois Wesleyan University, 2014

Submitted in Partial Fulfillment of the Requirements

For the Degree of Doctor of Philosophy in

Chemistry

College of Arts and Sciences

University of South Carolina

2019

Accepted by:

Morgan Stefik, Major Professor

Aaron K. Vannucci, Committee Member

Brian C. Benicewicz, Committee Member

John W. Weidner, Committee Member

Cheryl L. Addy, Vice Provost and Dean of the Graduate School

DEDICATION

To my wife. Your support has been invaluable; your wit, inevitable; and your presence, delightful.

ACKNOWLEDGEMENTS

I would like to acknowledge the contributions made to the works published here: my lab-mate and friend, Dr. Amrita Sarkar; my PI, Dr. Morgan Stefik; and the collaborators from other universities that made important contributions to the experimental and written portions of this work – Dr. Pratap Rao and Lite Zhou at Worcester Polytechnic Institute, Dr. Wilson Smith and Bartek Trześniewski at Delft University of Technology, and Dr. Henning Döscher at the Fraunhofer Institute for Systems and Innovation Research ISI.

I also acknowledge the support and guidance provided by the members of my committee – Drs. Aaron Vannucci, Brian Benicewicz, and John Weidner. The track of my research progress and scientific writing skills were invaluably improved by their contributions.

The friends I have made in my group have also been so important to me. Amrita Sarkar, Kayla Lantz, Zachary Marsh, and newer additions (Eric Williams, Taylor Larison, and Wessel van den Bergh) have helped this research tangibly as well as making graduate school enjoyable – or at the very least, more bearable.

I cannot overstate the support provided by my wife Meghan Lamm. You have supported me, driven me to do better, and have kept me grounded when I have gotten too carried away. I would not have made it here without you.

Finally, I would like to acknowledge the support staff of our department. While administrative work is something many would prefer to ignore, your work is what allows researchers – PI's and graduate students alike – to do the work they do.

ABSTRACT

The controlled fabrication of nanometer scale devices is of fundamental concern for numerous technologies, from separations to electronics and catalysis. The complexity of device architectures calls for the development of synthetic methods that independently control each feature: pore dimensions, wall thickness, and any subsequent functional nanomaterial layers (e.g. photoactive electrocatalysts). Precision control over these orthogonal methods can be used to integrate 3D and 1D nanostructures.

This dissertation presents the development of techniques useful in fabricating highly controlled nanoscale devices. The growth of single-phase bismuth vanadate ($BiVO_4$) by atomic layer deposition (ALD) is demonstrated for the first time, allowing for the conformal growth of ultrathin $BiVO_4$ on arbitrary substrates. A new tin oxide underlayer (SnO_2) was developed to act as a hole-blocking underlayer concomitantly with ultrathin $BiVO_4$ is to fabricate space-efficient photoanodes on a high-aspect ratio 3D substrate, combining the advantages gained by reducing $BiVO_4$ thickness and preserving optical thickness. The heterojunction $SnO_2/BiVO_4$ space-efficient photoanode achieved the highest reported applied-bias photon-to-charge efficiency for any photoanode material synthesized via ALD. Lastly, the first demonstration of persistent micelle templates (PMT) with carbonaceous materials is reported, demonstrating independent control over important feature sizes, such as wall thickness and pore size, to adjust the capacity and charge/discharge rates of carbon-based supercapacitors.

TABLE OF CONTENTS

LIST OF TABLES

LIST OF FIGURES

LIST OF SCHEMES

CHAPTER 1:
INTRODUCTION AND BACKGROUND[1]

[1] Adapted with permission from Lamm, B.; Trześniewski, B.; Döscher, H.; Smith, W.; Stefik, M. *ACS Energy Lett.* **2018**, *3*, 112-124. Copyright 2018 American Chemical Society.

Research Objective

Controlled fabrication of nanometer-scale structures in devices is of fundamental concern for numerous technologies, such as electronics, catalysis, or purification. Multiple transport events occur at various locations within device architecture, requiring discrete control over independent features of mesoporous materials (Figure 1.1). For example, the rate of diffusion for catalyst reactants and products like water and oxygen is affected by the pore size (Figure 1.1a). If the pore is too small, compounds are slow to diffuse to the catalyst surface or are unable to reach exposed surfaces at all; alternatively, if the pores are too large, then the space is not efficiently utilized, lowering the overall efficiency of the device. Additionally, the thickness of the active layer (Figure 1.1c) is selected by balancing carrier transport properties, such as the charge carrier separation efficiencies, and absorptivity; and the wall thickness of the porous structure (Figure 1.1b) is optimized based on space efficiency and conductivity, where thicker walls generally improve conductivity while increased volume of inactive material lowers the space efficiency. Control over these device dimensions can be achieved through multiple routes, including soft templating with block-copolymers and atomic layer deposition. In these examples, block polymer templates can create structures with high levels of organization on the nanometer scale whereas atomic layer deposition (ALD) can infiltrate such structures to grow uniform ultrathin coatings.

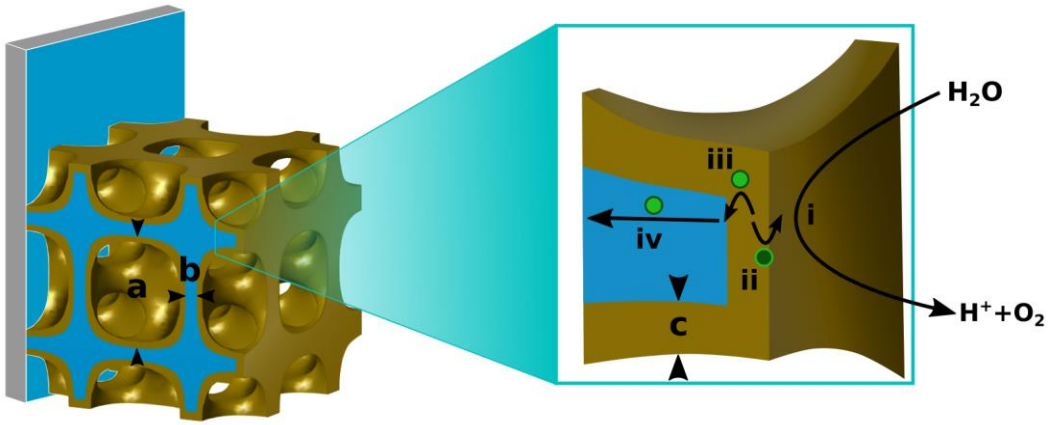

Figure 1.1: Scheme depicting relevant feature sizes and transport events. The size of pores (a) and walls (b) are set during synthesis of the blue conductive substrate, while the thickness of the active material (c) is controlled by the active layer deposition process. These features directly affect the efficiencies of transport processes, such as (i) diffusion of catalyst substrates and products to and from the surface, separation of (ii) holes and (iii) electrons within the active material, and (iv) conduction of electrons to the circuit within the substrate.

Functional materials, such as electrocatalysts, operate on a balance of pathways for concomitant processes. In photoelectrochemical (PEC) water splitting, sunlight is used to drive the formation of oxygen and hydrogen gasses from water. In the case of bismuth vanadate ($BiVO_4$), a short electron transport length (~70 nm) requires a thin layer of material to improve electronic efficiency while an optical absorption length of ~700 nm requires a far higher optical thickness.[1] The mismatch between these two defining feature sizes, requiring simultaneously thin physical layers with high optical thickness, inspired the development of ultrathin $BiVO_4$ on high-aspect ratio substrates. Typical methods utilize variations on the sol-gel process common in metal organic synthesis or multi-step electrodepositions;[2] however, despite significant improvements to performance, precise control over the appropriate dimensions could not be achieved by these methods, especially in conjunction with "hole-blocking" underlayers (such as SnO_2) that have been used to improve electron transfer efficiencies. This dissertation addresses this mismatch by demonstrating the first ALD deposition of single-phase $BiVO_4$ and utilizing it in space-

efficient heterojunction photoanodes for solar water splitting.[3,4] Background for these topics will be further described later in this chapter.

In another direction, block copolymers have been used in persistent micelle templating (PMT) to organize tunable mesoporous carbons, allowing independent control over pore size and wall thickness for these devices. Organic templates such as block copolymers (BCPs) have been used as structure directing agents to synthesize mesoporous metal oxides and carbons for several decade.[5] However, this method of soft templating has historically suffered from two major problems. As BCPs self-assemble to equilibrium-driven morphologies, changing the loading of metal oxide precursors causes a shift in the resulting morphology (1) such that the final structure dimensions – e.g. pore and wall thickness – change dependently with precursor loading. Secondly, changes to solvent conditions can cause a shift in the equilibrium phase (2) such that the final morphology structured can shift dramatically. To expand the utility of soft-templating methods, persistent micelle templating (PMT) was developed.[5–8] This technique allows the independent tuning of wall thickness and pore size of templated metal oxides. However, PMT to date has only been demonstrated for metal oxide templating (e.g. TiO_2, Nb_2O_5) and is sensitive to solvent conditions, primarily water content.[5,7] This dissertation discusses the development of carbon PMT (CPMT) using glassy-core micelles and phenolic carbon precursors.

Dissertation Outline

This dissertation focuses on the controlled fabrication of nanoscale materials employing (1) the development of SF-ALD for the growth of single-phase $BiVO_4$ for photoelectrochemical water splitting, (2) the utilization of ultrathin $BiVO_4$ and SnO_2 in space-efficient photoanodes, and (3) PMT of carbonaceous materials for tunable porous carbon electrodes. The primary discussion follows the development a novel synthesis for

thin layers of $BiVO_4$ for use as a photoanode, culminating in the construction of a space-efficient heterojunction photoanode. The secondary discussion examines the expansion of PMT to carbon-based devices, demonstrating for the first time the independent control of wall thickness and pore size in porous carbons.

Following this outline, the remainder of this chapter will be devoted to providing background on the researches on $BiVO_4$ as a photoelectrode. Topics therein include a brief overview of $BiVO_4$ as used in solar water splitting with a more in-depth discussion of postsynthetic improvements to $BiVO_4$ photoanodes. These changes affect either charge injection or charge separation efficiencies, resulting in distinct chemical changes that are difficult to identify with traditional characterization techniques.

In Chapter 2, the atomic layer deposition of bismuth vanadates is improved by a surface-functionalization step during deposition (SF-ALD) resulting in the first ALD process for single-phase scheelite $BiVO_4$. Besides the synthetic novelty of this technique, this study also identifies a photoelectrochemical activation technique that results in a threefold improvement to charge separation. These improvements are tentatively attributed to changes in oxidation state of bismuth and vanadium defects within $BiVO_4$.

Chapter 3 utilizes the SF-ALD of $BiVO_4$ in a heterojunction photoanode with tin oxide (SnO_2) to realize space efficient host-guest photoanodes. The utilization of ALD for synthesis of both SnO_2 and $BiVO_4$ resulted in a lower SnO_2 defect density than is observed in SnO_2 synthesized via spray pyrolysis or spin coating, allowing for a significantly thinner underlayer (8 nm vs 65-80 nm). This ultrathin underlayer film is especially of interest in high aspect ratio substrates, such as antimony-doped tin oxide nanotubes (ATO NTs), greatly improving the space efficiency of $SnO_2/BiVO_4$ heterojunction photoanodes. The

final host-guest architectures were demonstrated to achieve an applied bias photon-to-charge efficiency of 0.71%, a new record for a photoanode absorber prepared by ALD.

Whereas Chapters 2 and 3 are devoted to the controlled conformal deposition of $BiVO_4$ via ALD, Chapter 4 focuses on the fabrication of porous carbons with independent control over wall thickness and pore size. Synthetically this is achieved by condensation polymerization of resorcinol and formaldehyde in the presence of persistent micelle templates. Future directions of development of this concept are discussed.

Finally, this dissertation will conclude with a summary of the results and possible future works in Chapter 5. Collectively, this dissertation discusses the improved structure control for nanometer-scale porous materials.

Background on $BiVO_4$ Research: Emerging Postsynthetic Improvements of $BiVO_4$ Photoanodes for Solar Water Splitting

Abstract

Solar-assisted water splitting with bismuth vanadate ($BiVO_4$) photoanodes has progressed significantly with many efforts devoted to improving charge separation and surface charge injection through synthetic methods, including dopants and catalytic layers. In contrast, postsynthetic treatments occur after the synthesis of electrodes. Recently, such postsynthetic treatments based upon illumination, chemistry, electrochemistry, or combinations thereof have led to dramatic improvements in the performance and efficiency of $BiVO_4$ photoanodes. This perspective summarizes recent $BiVO_4$ postsynthetic treatments with mechanistic details and highlights important future directions. One broad challenge is that multiple interpretations of defect changes may be consistent with routine XPS data. Further experiments are suggested to better differentiate between the proposed defect changes. Also, performance changes are considered separately with respect to charge separation and charge injection efficiencies as well as within the context of known

synthetic modifications. The emergence of postsynthetic treatments highlights new opportunities to understand and improve photoelectrodes. Similar mechanisms may be of further utility as researchers turn more focus towards the development of novel multinary metal oxide photoabsorbers to produce solar fuels. Lastly, postsynthetic treatments also elucidate possible electrode changes under extended service and can provide new strategies to enable extended device performance.

Introduction

Monoclinic bismuth vanadate ($BiVO_4$) is a promising and widely studied photoanode for solar-assisted water splitting,[9,10] made from cheap source compounds. $BiVO_4$ has an indirect bandgap energy of approximately 2.4-2.5 eV (~500-520 nm band edge),[2,11] with absorption into the visible and UV range of light, and with a maximum theoretical photocurrent of ~7 mA cm^{-2} under 1 sun AM 1.5G illumination. Additionally, a wider direct bandgap (ca. 2.7 eV) is also present in $BiVO_4$.[11] The conduction band edge (CB) lies near 0 V_{RHE} (versus reversible hydrogen electrode), placing the valence band edge (VB) near 2.4 V_{RHE}, and providing significant excess potential for holes to photooxidize water while electrons maintain a potential appropriate for hydrogen evolution at the counter electrode with moderate external bias. A thorough review of $BiVO_4$ photoelectrochemical (PEC) properties and challenges was recently published.[2] Postsynthetic treatments have recently emerged as a way to significantly improve PEC performance with treatments that occur after the synthesis of electrodes. These postsynthetic treatments are based upon illumination, chemistry, electrochemistry, or combinations thereof, improving the PEC performance of active materials in ways that typically cannot be achieved via direct fabrication methods. This perspective highlights recent findings with $BiVO_4$ postsynthetic treatments and identifies important avenues of future inquiries.

The efficiency of solar fuels production requires consideration of both the photocurrent and the applied voltage bias. The role of photocurrent is apparent and linearly scales with the energy stored. Most oxide-based PEC devices require some externally applied voltage bias (E_{app}). Thus, the resulting fuel contains energy from both the external voltage source and the PEC device itself. The use of excessive bias voltage diminishes the balance of solar energy stored. The applied bias photon-to-current efficiency (ABPE) takes this important applied potential into account when expressing the efficiency of conversion from solar to chemical energy:[12,13]

$$\mathrm{ABPE}(\%) = \left[\frac{(J_{photo})(\mathrm{mA\ cm^{-2}}) \times (E_{rc} - E_{app})(\mathrm{V})}{P_{photo}(\mathrm{mW\ cm^{-2}})}\right]_{\mathrm{AM\ 1.5G}} \times 100 \qquad (1.1)$$

where J_{photo} is the measured photocurrent at a particular applied potential (E_{app}), P_{photo} is the power density of AM 1.5G (100 mW cm^{-2}), and E_{rc} corresponds to the cell potential of the redox couple; 1.23 V_{RHE} corresponds to the standard cell potential for water splitting.[2] It is important to distinguish between the ABPE calculated with a 2-electrode configuration (E_{app} is between the working and counter electrodes) for overall water-splitting ABPE versus the ABPE calculated with a 3-electrode configuration (E_{app} is between the working and reference electrodes). The ABPE values in Figure 1.2b were calculated from 3-electrode data to provide a level comparison between samples since 3-electrode data is the most readily available in publications. Photocurrents as high as 6.7 mA cm^{-2} (~90% of the theoretical limit) have been reported for $BiVO_4$ with E_{app}=1.23 V_{RHE};[14] however, operation at this voltage corresponds to an ABPE of 0% (Figure 1.2a).[3] Including both photocurrent and applied voltage shows maximum demonstrated ABPE values of 2.2-2.3% for $BiVO_4$

[2] Other units may be appropriately used.
[3] Data were extracted from published figures using ScanIt 2.0 software.

(Figure 1.2b; 0.6 V_{RHE}, 3.2-3.4 mA cm^{-2}).[13,15] A simple theoretical upper limit of 6.4-7.7% ABPE for water splitting may be estimated by considering the theoretical photocurrent limit (6.2-7.5 mA cm^{-2} for a bandgap of 2.5-2.4 eV, respectively) and band positions (neglecting HER and OER overpotential losses; i.e. photocurrent saturation at 0.2 V_{RHE} with 100% fill factor). Clearly, there remains much room for ABPE improvement by focusing on improving low-bias-voltage operation. Design strategies should thus work to maximize both charge separation and charge injection of $BiVO_4$ with low applied bias voltage.

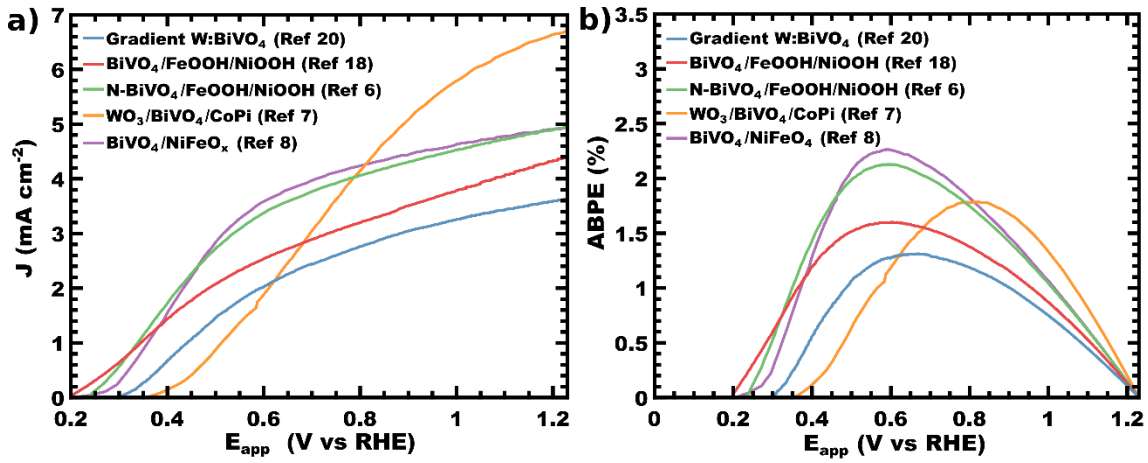

Figure 1.2 a) J-V characteristics of $BiVO_4$ photoanodes and b) applied bias photocurrent conversion efficiencies of high performing $BiVO_4$-based photoanodes. All data were obtained with a 3-electrode configuration to exclude variable counter electrode contributions.

Overview of photoelectrochemical processes in $BiVO_4$

For any photoelectrode material, the overall PEC performance, measured by J_{photo}, is determined by the combination of several phenomena, including the charge separation efficiency, the charge injection efficiency, and light harvesting efficiency (LHE), and can be expressed as follows (Equation 1.2). Here, J_{abs} is the photon absorption rate expressed as a current density (determined from LHE and the illumination spectrum), and φ_{sep} and

φ_{inj} are the charge separation and charge injection efficiencies, respectively (Figure 1.3a).[16,17]

$$J_{photo}(V) = J_{abs} \cdot \phi_{sep}(V) \cdot \phi_{inj}(V) \quad (1.2)$$

For pure $BiVO_4$, φ_{sep} is often limited by bulk recombination and trapping of charge carriers (Figure 1.3b)[18–23] whereas φ_{inj} is typically limited by slow water oxidation kinetics and surface recombination (Figure 1.3c), although these can effectively be mitigated with the addition of co-catalyst layers.[24–26] The efficiency of each step is dependent on physical and chemical processes within the bulk or at the surface of the material. The relative rates of water oxidation (k_{wo}) and recombination (k_{rec}) determine the charge injection efficiency φ_{inj} at the surface (assuming 100% faradaic efficiency) (Equation 1.3).[24,26]

$$\phi_{inj}(V) = \frac{k_{wo}(V)}{k_{rec}(V)+k_{wo}(V)} \quad (1.3)$$

Charge separation is accomplished by a combination of drift from an external applied potential or from the internal potential from the space charge layer (SCL), as well as diffusive charge transport. For pristine (undoped) $BiVO_4$, the SCL width can be as high as 90 nm;[24] this would enhance φ_{sep} of very thin, <90 nm, films. In contrast, thicker films (>200 nm) are needed to achieve reasonable LHE values, dimensions where φ_{sep} is considerably reduced since most carriers are produced outside of the SCL. This may be mitigated by enhancing the extent of band bending with gradient-doping.[27] Use of a large external bias voltage can enhance charge separation at the cost of significant loss of overall ABPE. The separation of charge carriers produced far from the SCL is limited by low carrier conductivity as well as recombination sites within the film or at the substrate-$BiVO_4$ interface.[18,20] Here, since $BiVO_4$ is normally operated with bias voltage, improvements to

conductivity (product of mobility and carrier concentration) can improve charge separation.

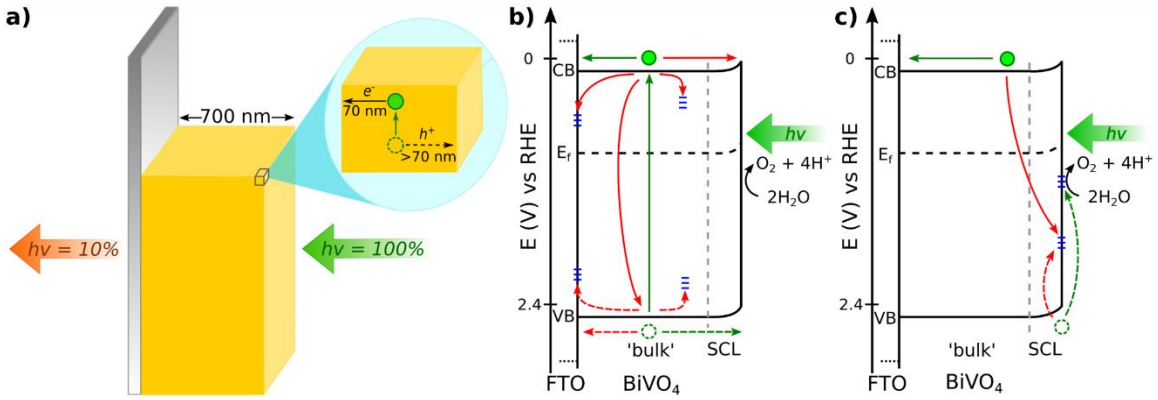

Figure 1.3 For solid films, there is a trade-off between light harvesting efficiency and charge separation efficiency. Band diagrams of $BiVO_4$ showing step-wise processes towards water splitting with b) light harvesting and charge separation (φ_{sep}) followed by c) charge injection (φ_{inj}). The green paths support water splitting whereas the red paths are loss pathways.

Defining synthetic vs. postsynthetic modification

Synthetic strategies to improve the PEC properties of $BiVO_4$ – such as nanostructuring films, designing heterostructures, applying oxygen evolution catalysts (OECs), adding dopants to $BiVO_4$, among others – have been developed and used to great effect, and were reviewed elsewhere.[2,28,29] Postsynthetic treatments have been concurrently developed and have enabled many of the highest photocurrents reported to date.[13–15] These treatments are applied after the synthesis of $BiVO_4$, and are based upon illumination, chemistry, electrochemistry, or combinations thereof. Postsynthetic treatments are intended to modify the defect chemistry of existing material rather than to deposit additional material. For this reason, treatments that deposit metallic elements are not considered as postsynthetic treatments. For example, here we consider annealing $BiVO_4$ under H_2 or N_2 gases to be postsynthetic treatments whereas the deposition of passivation or catalytic layers (e.g.

FeOOH, CoPi, etc.) is a synthetic treatment. Broadly, postsynthetic treatments affect φ_{sep}, φ_{inj}, or both to improve the overall ABPE performance of $BiVO_4$.

An electrochemical treatment of Mo:$BiVO_4$ was reported in 2011;[30] this was followed by H_2-annealed $BiVO_4$ in 2013 and subsequent followups.[31–34] In 2015, N_2-annealed $BiVO_4$ was demonstrated to attain one of the highest ABPEs on record,[13] second only to a report on electrochemically-treated catalyzed $BiVO_4$ in 2016.[15] Two illumination-dependent treatments, UV-curing and photocharging of $BiVO_4$, were published in 2015,[35,36] with later follow-up reports.[37,38] In 2016, a significantly accelerated PEC activation used a combination of light, electrolyte, and applied potential.[3]

The defect changes during postsynthetic treatments are sometimes subject to multiple equivocal interpretations as many of the proposed mechanisms are consistent with the often-limited experimental data. For example, the addition of both hydrogen interstitials[37] and hydrogen anti-site on oxygen,[33] and both the addition[31] and removal[33] of oxygen vacancies have been supported by similar shifts in vanadium X-ray photoelectron spectroscopy (XPS) data; such contradictory defect chemistries clearly require additional investigation. Multiple intrinsic defects (e.g. oxygen, bismuth, or vanadium vacancies ($v_O^{\bullet\bullet}$, $v_{Bi}^{'''}$, and $v_V^{'''''}$), interstitials ($O_{int}^{''}$, $Bi_{int}^{\bullet\bullet\bullet}$, and $V_{int}^{\bullet\bullet\bullet\bullet\bullet}$), and anti-sites ($Bi_V^{''}$ and $V_{Bi}^{\bullet\bullet\bullet}$)) and extrinsic defects (e.g. hydrogen interstitial, $H_{int}^{\bullet}$, or substitution, $H_O^{\bullet\bullet\bullet}$) are proposed to exist in $BiVO_4$, either directly after synthesis or after exposure to PEC conditions (i.e. illumination and electrolyte).[33,34,37] Additionally, defect clusters – e.g. double or triple vacancies like $v_{Bi}^{'''}v_O^{\bullet\bullet}$, $v_{Bi}^{'''}v_O^{\bullet\bullet}v_{Bi}^{'''}$, or $v_{Br}^{\bullet}v_{Bi}^{'''}v_O^{\bullet\bullet}$ – are also proposed to affect the catalytic activity of semiconductor photoelectrodes.[39] Differentiating between these numerous possible defect chemistries will require more detailed follow up studies using experimental

techniques that can probe local electronic environments, and subsequently study charge carrier kinetics to elucidate defect activity (e.g. as trap, donor, and/or catalytic sites). Furthermore, the synthetic route dependence on subsequent postsynthetic behaviors is rarely considered – is it not reasonable that the native material defects should affect the results of a postsynthetic treatment?

The emergence of postsynthetic treatments highlights new opportunities to understand and improve photoelectrodes. Similar mechanisms may be of further utility as researchers turn more focus towards the development of novel multinary metal oxide photoabsorbers where, like $BiVO_4$, there is a combinatorial expansion of the candidate point defect chemistries. Lastly, postsynthetic treatments also elucidate possible electrode changes under extended service and can provide new strategies to enable extended device performance. This perspective will provide an overview of a variety of reported postsynthetic treatments and attempt to describe unifying features between treatments as well as paths forward towards a deeper understanding.

Postsynthetic improvement of charge separation

Synthetic approaches to improve φ_{sep} are based on two main approaches: increasing the free carrier density by substituting V with higher valent metals (e.g. Mo, W)[17,20,27,30,40–43] and limiting recombination at the back-interface by adding "hole blocking layers," such as SnO_2 or WO_3, between $BiVO_4$ and the substrate.[14,18–20,44,45] Postsynthetic techniques have recently emerged with similarly significant improvements to charge separation.

Postsynthetic removal of recombination sites

Bismuth vanadate photoelectrodes have been synthesized using numerous techniques including sol-gel,[17,46] spray pyrolysis,[18] electrodeposition and conversion,[15,25,47] magnetron sputter deposition,[43,48,49] chemical vapor deposition (CVD),[50] and atomic layer deposition

(ALD),[3,51] where each method results in varying performance, partially due to the nature of the inherent defects. The combination of mobility and carrier lifetime results in a limited ~70 nm transport length of electrons within $BiVO_4$, with holes able to diffuse farther.[20] This characteristic is why numerous $BiVO_4$ publications report higher photocurrents with back-side illumination to minimize the transport distance for electrons.

Many of these synthetic techniques have been utilized to minimize the transport lengths of charge carriers. The nanostructuring of pure $BiVO_4$ improves minority (hole) carrier transport to the surface,[15,25] whereas host-guest approaches are needed to improve electron transport to the substrate.[14,45,52–55] Thus far, the methods used for the production of $BiVO_4$ host-guest nanostructures have all utilized non-uniform depositions or cathodic electrodepositions that limit the use of hole-blocking layers at the $BiVO_4$-substrate interface.[14,45,52,53] Atomic layer deposition (ALD) stands out as a method to fabricate conformal $BiVO_4$ coatings within complex device architectures while retaining compatibility with hole-blocking layers and radial dopant profiles.[51] Surface functionalized ALD (SF-ALD) was recently shown to enable phase pure scheelite $BiVO_4$.[3]

The φ_{sep} of SF-ALD $BiVO_4$ was remarkably sensitive to postsynthetic treatment. Postsynthetic enhancements were maximized with a treatment that involved exposing the sample to AM 1.5G simulated illumination while applying an external bias of 0.6 V_{RHE} for 1 h. Corresponding to this treatment (PEC activation), film optical absorptance decreased, φ_{sep} increased, and both absorbed and incident photon-to-charge efficiencies increased (APCE and IPCE, respectively; Figure 1.4a), with an increase of APBE from 0.18 to 0.28% for 75 nm-thick films in electrolyte with hole scavenger (sulfite, E_{rc} = 0.93 V_{RHE} in Equation 1.1).[3,56] Note that φ_{inj} is assumed to be unity in the presence of hole scavenger;

no water oxidation data was presented. The simultaneous increase of transparency with photocurrent is counterintuitive given the relationship between LHE and photocurrent in Equation 1.2. This effect is attributed to the removal of metallic defects during treatment (*vide infra*), which is expected to improve φ_{sep} by removing photoabsorbing trap sites, thus decreasing the overall optical absorption. The postsynthetic enhancements were shown to be stable for at least 17 h. During PEC activation, an oxidative photocurrent was observed to increase and plateau; this was attributed to the combined oxidation of hole scavenger and $BiVO_4$ defects. XPS (Figure 1.4b) analysis suggested that reduced metal defects in calcined SF-ALD samples (Bi^0 and V^{4+}) were fully oxidized (Bi^{3+} and V^{5+}) following PEC activation. The ALD of bismuth titanates with the same Bi^{3+} precursor was previously shown to result in a mixture of Bi^{3+} and Bi^0,[57] highlighting the connection of synthetic route with point defect chemistries. Related postsynthetic treatments such as UV-curing and photocharging also involve illumination;[36,37] however, control experiments demonstrated that the applied bias with PEC activation leads to larger improvements to φ_{sep} and occur much faster within 1 hr. The ability of bismuth vanadate to self-heal may explain its label as a "defect tolerant" material.[20] More work is needed to establish the precise nature of the defects present in the untreated $BiVO_4$, and to determine if any other phenomenon are taking place; e.g., hydrogen or proton uptake or surface state alteration.[33,34,37]

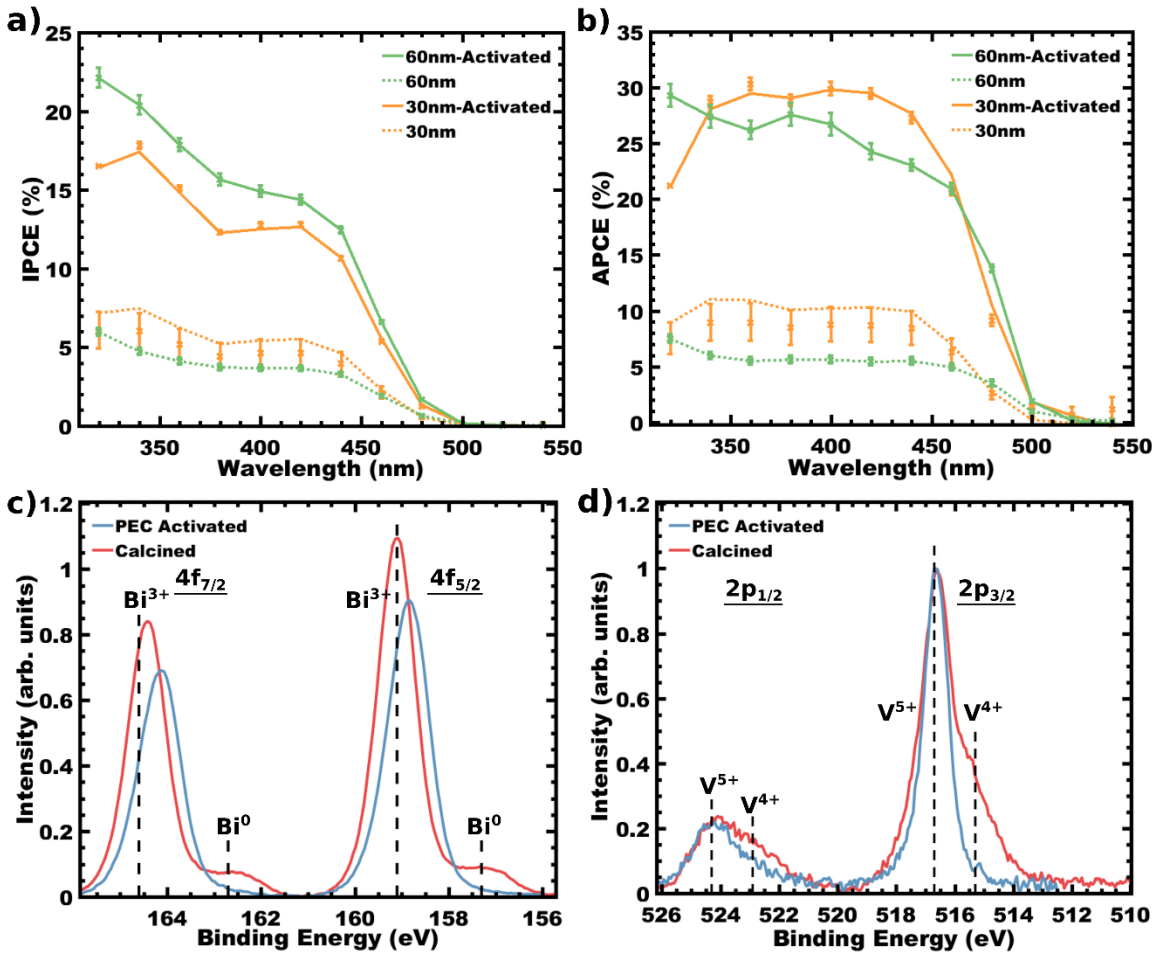

Figure 1.4: Effect of a post-synthetic PEC activation treatment on 30 and 60 nm films prepared by SF-ALD; a) IPCE, b) APCE, and XPS of c) Bi 4f and d) V 2p comparing as-made and activated SF-ALD $BiVO_4$. Reproduced with permission from Reference 3 - Published by The Royal Society of Chemistry.

Annealing $BiVO_4$ films in H_2 was found to increase the concentration of V^{4+} species while removing or passivating trap states.[31,33,34] H_2-annealing has been demonstrated to improve the onset potential and photocurrent of the photoelectrodes (93 mV shift to onset potential and increase to photocurrent from 1.23 to 1.43 mA cm^{-2} at 1.23 V_{RHE} between as-grown and 290 ^oC H_2-annealed $BiVO_4$, respectively),[31,33] corresponding to an increase in APBE for sulfite oxidation from 0.18 to 0.27% between as made and H_2-annealed $BiVO_4$. Optimal annealing conditions were reported as 15 min at 290 ^oC under 1 atm of H_2.[33] H_2 annealing primarily improves φ_{sep}; however, a decrease in φ_{inj} was also reported,[34] possibly

due to surface H affecting water oxidation kinetic activity.[34,58,59] Additionally, changes to the surface hydroxyl (-OH) concentration were reported;[32] such alterations were reported to affect φ_{inj} in $BiVO_4$.[35,36] This treatment was found to improve photocurrent regardless of synthetic procedure,[34] and was helpful in improving the photocurrent of other photoanode materials.[60–62] In the initial report,[31] density functional theory (DFT) calculations suggested that elemental H was occupying both interstitial and oxygen sites within the $BiVO_4$ lattice, with both types of defects expected to act as shallow donors. A follow-up report identified two local hydrogen environments by ^{1}H-NMR spectroscopy that were attributed to interstitial hydrogen (H_{int}) and substitutional hydrogen (H_O).[33] Notably, H_O also had a trace presence in as-made $BiVO_4$. This was further supported by a second follow-up report that quantitatively analyzed the loading of hydrogen into $BiVO_4$ by ^{15}N nuclear reaction analysis, finding about 5x the amount of hydrogen in annealed films (0.7 vs 0.14 at% for H-$BiVO_4$ and $BiVO_4$, respectively).[34] Initially, the partial reduction of V from 5+ to 4+ was attributed to the formation of oxygen vacancies, v_O.[31] However, subsequent investigations correlated H_2-annealing to a reduced photoluminescence (attributed to removal of v_O)[33] and increase in charge carrier lifetime, suggesting a decrease in trap concentration by the removal or passivation of traps (proposed to be interstitial V or V anti-site on Bi, V_{int} or V_{Bi}).[34] Follow-up reports also agree on the presence of one of the aforementioned hydrogen defects (H_{int}, bonded to a bridging O), and that increasing the v_O content is not the source of improved φ_{sep}. There remains some question as to the nature of the trap states removed or passivated (e.g. v_O, V_{int}, or V_{Bi}).[33,34] Furthermore, there is disagreement as to the effect of H_2-annealing on charge carrier conductivity.[33,34] Considering that both v_O and H_O can yield the same XPS observation of

partially reduced vanadium, follow up studies on hydrogenated photoelectrode materials would benefit by parsing the multiple causal pathways with further measurements such as electron energy loss spectroscopy (EELS)[63–65] or X-ray absorption near edge structure (XANES)[66] to probe changes to local electronic environment caused by specific defect chemistries.

Postsynthetic production of free carriers

Doping $BiVO_4$ with metals and non-metals – commonly W and Mo – has been widely utilized to synthetically alter the carrier density and conductivity of $BiVO_4$-based photoanodes.[18,20,30,35,40–43,67] Recently, several postsynthetic techniques have been utilized to similarly increase free carrier density.[13,15,68] It has been suspected that V^{4+} plays a role in the native conductivity of $BiVO_4$ photoanodes,[69] typically attributed to the formation of O vacancies (v_O) as a shallow donor state.[70] Consequently, several postsynthetic treatments have related effects to conductivity and ABPE to alterations in V oxidation state.[15,31,68] However, recent work has shown that the mobility of charge carriers in $BiVO_4$ is not improved by increasing v_o concentration,[33,34] suggesting that an alternative mechanism may be present.

To achieve one of the highest reported ABPEs, researchers activated their electrodes with a simple cyclic voltammetry treatment in alkaline media prior to depositing the catalytic Ni-borate layer.[15] This treatment (five cycles of voltammetric scans from 0 to 1 V_{RHE} at 40 mV s^{-1}) was suggested to involve the reversible redox between V^{5+} and V^{4+}. Improvements to φ_{sep} following this treatment were attributed to an improved (lower gradient) distribution of V^{4+} near the surface of the film.[15] The authors noted that others had observed a 5 nm "reduction shell" at the surface of $BiVO_4$; however, those observations were on commercial powders that had not carried out PEC, and the scanning transmission

electron microscopy (STEM) imaging may have itself induced changes.[64] Within this reduction shell, vanadium primarily exists in the 4+ state – compared to the 5+ state of bulk V – producing a n^+-n homojunction that is deleterious to charge separation.[15,64] It was also noted that onset potential was affected by vanadium redox changes. An anodic shift to onset potential was observed with starting potentials of 0.05 to 0.25 V_{RHE} in current-potential scans, indicating overly-reduced V^{4+} produces charge recombination sites.[15] An alternative mechanism for film activation could involve the incorporation of hydrogen defects (H_{int} or H_o, for example), which would also reduce vanadium while introducing shallow donors; further measurements could clarify the changes to defect chemistry caused by such treatments. Calculation of the relative ABPE enhancement would require electrochemical data from the as-made sample.[15]

Doping $BiVO_4$ with N_2 (N-$BiVO_4$) was also shown to primarily improve photocurrent and φ_{sep}.[13] Charge injection efficiency was calculated to slightly increase as well. This treatment was reported to incorporate N in the lattice, accompanied by the generation of v_o. Using Kröger-Vink notation, the proposed reaction was:[13]

$$3O_O^x + N_2(g) \rightarrow 2N_O' + v_O^{\bullet\bullet} + 1.5O_2(g) \quad (1.4)$$

where O_O^x denotes oxygen on an oxygen site, N_O' denotes nitrogen on an oxygen site, and $v_O^{\bullet\bullet}$ denotes an oxygen vacancy. N-$BiVO_4$ was achieved by annealing under N_2 at 350 ^oC for 2 h. N-$BiVO_4$ resulted in a reduced bandgap (~0.2 eV less) compared to untreated $BiVO_4$ by increasing the VB maximum, as suggested by DFT calculations and IPCE measurements. Whereas v_O are proposed by some to yield localized trap states in $BiVO_4$,[13,33] the v_O production in N-$BiVO_4$ was also accompanied by a shift of the valence band towards the conduction band, enhancing activation of v_O as donor states. The charge

mobility increased by 25%, corresponding to an improvement in φ_{sep} from 88 to 94% at 1.0 V_{RHE}. The concomitant reduction of bandgap notably also improved optical absorbance.[13] The authors noted that the changes in the XPS spectrum were not suggestive of changes to the Bi nor V oxidation states, unlike several other postsynthetic treatments discussed thus far. Overall, N-$BiVO_4$ produced one of the highest ABPEs reported to date (2.16%); in comparison, untreated $BiVO_4$ samples demonstrated an ABPE of 1.63%. Additionally, the photocurrent for sulfite oxidation was stable for 50 h without decay;[13] and water oxidation photocurrents decayed after 30 h due to film degradation (perhaps caused by the use of a phosphate buffer).[13,15,71] Further investigation into the defect chemistry specific to $BiVO_4$ synthesized in this manner (i.e. electrodeposition and conversion) could be particularly insightful, given the exceptionally high performance (APBE) of this and similar reports (for example, references [15] and [25]).

Although the partial reduction of vanadium species is often correlated with improved PEC properties (e.g. φ_{sep} or φ_{inj}), the direct (electro)chemical reduction of $BiVO_4$ is not as effective.[68] For example, $BiVO_4$ was reduced electrochemically for 3 min at ca. -0.3 V_{RHE} followed by chemical reduction in 0.1 M $NaBH_4$ for 3 min which enhanced the photocurrent from 0.5 to 1.4 mA cm^{-2} at 1.2 V_{RHE} and was ascribed to an enhanced free-carrier density from the production of v_O and the associated reduced vanadium oxidation states, as evidenced by XPS.[68] ABPE increased from 0.04 to 0.16% following this combined treatment. However, the benefits of this treatment were stable for only 40 min before the photocurrent began to decay significantly, returning to the initial (untreated) photocurrent after 75 min. The instability of this treatment might be due to the over-reduction of $BiVO_4$,[33] possibly resulting in the re-oxidation of species within the electrode.

Additionally, more mild reducing treatments (e.g. annealing in Ar to induce v_o formation or less aggressive electrochemical treatment) have resulted in little to no change to $BiVO_4$ water oxidation performance.[30,34]

Briefly we note that the conductivity of $BiVO_4$ may also be enhanced thermally or by significantly increasing photon flux. The low minority carrier mobility in $BiVO_4$ is caused by localization of the carriers as small polarons.[72] A modest temperature increase from 10 to 42 °C was shown to activate minority carrier hopping in $BiVO_4$ and significant enhance the PEC activity from 1.8 to 4.0 mA cm^{-2} at 1.0 V_{RHE}.[42] Similarly, increasing the concentration of incident photons (from ~10^{18} photons cm^{-2} s^{-1} for AM 1.5 to ~10^{24}-10^{28} photons cm^{-2} s^{-1}) can overcome trapping mechanisms for both charge carriers and significantly enhance mobility.[20,22,23,34]

Summary

Conventional methods of improving φ_{sep} in $BiVO_4$-based photoanodes have primarily been confined to hetero-metal dopants and hole blocking layers.[18,40,45] Postsynthetic techniques that have recently emerged can supplement or replace synthetic approaches by removing common and/or synthesis-specific bulk defects, and increasing the free carrier density.[3,13,15,31,33,34] The development of these postsynthetic techniques continues to improve the understanding of $BiVO_4$ defect chemistry and highlights the differences between various synthetic methods.[3,33,34]

It is important to note that two of the techniques discussed produced stable improvements through mild (photo)electrochemical treatments.[3,15] One may expect that these treatments only affect the near-surface, however the improvements to φ_{sep} suggest that bulk changes may be occurring e.g. intercalation of hydrogen. Further data are needed to better understand these changes.

Postsynthetic improvement of charge injection at the surface

Postsynthetic treatments have been developed to modify the surface and near-surface regions of $BiVO_4$-based electrodes. As described briefly in the introduction, the φ_{inj} suffers from slow water oxidation kinetics, which causes an accumulation of holes within the SCL, particularly at BiO_8 polyhedra.[73] This accumulation makes the back-recombination of holes and electrons kinetically viable.[24] Recombination can also occur at surface defects at the $BiVO_4$-electrolyte interface.[30,41,74] Furthermore, the build-up of holes within the SCL and near the surface of $BiVO_4$-based photoanodes was linked to photocorrosion,[2,9] in particular when immersed in alkaline electrolytes.[71,75] Clearly, the best strategies to improve φ_{inj} and prevent electrode degradation should involve either increasing the rate of water oxidation or decreasing the rate of near-surface recombination (Equation 1.3). Commonly, layers of additional materials as protective layers or catalysts – e.g. amorphous TiO_2,[41,44,75] CoPi,[17,19,76] NiOOH,[13,25] etc.[15,74,75,77–79] – are used to either block native defects, store holes to mitigate side reactions, or to catalyze the water oxidation reaction; however, simple postsynthetic modifications have also been used to mitigate surface defects.[30,36,37,74]

Removal of surface recombination sites

Surface recombination sites can be removed or blocked by simple postsynthetic treatments in both doped and pristine $BiVO_4$. These treatments provide simple routes to decrease k_{rec} and improve φ_{inj}, as described in Equation 1.3. Simulations of $BiVO_4$ surfaces suggest that hole localization and subsequent recombination at the electrode-electrolyte interface is caused by native crystal distortions;[73] while experimental evidence supports a second recombination mechanism via segregated surface species.[30]

Ion segregation, or enrichment of a material constituent, at the surface of photoelectrodes has been known to form recombination centers.[30,80] In the case of Mo-doped $BiVO_4$ (Mo:$BiVO_4$), Mo^{6+} aggregates at the surface were dissolved by an electrochemical treatment of 30 cyclic voltammetry scans from -0.3 – 1.16 V_{RHE}, causing the photocurrent at ~1.2 V_{RHE} to approximately double when illuminated from the front of the photoelectrode, based on XPS and PEC characterization, corresponding to an increase in ABPE from 0.09 to 0.24%. Comparatively, non-doped $BiVO_4$ electrodes showed no effect on photocurrent following the same electrochemical treatment, suggesting that the untreated Mo^{6+} locations are recombination sites at the semiconductor/electrolyte interface.[30] Additionally, Mott-Schottky analysis suggested that bulk properties (e.g. carrier concentration) were not altered by the treatment; i.e. only φ_{inj} was affected.[30] Interestingly, a Bi-rich surface layer was observed following the electrochemical treatment, suggesting that V was also dissolved from the surface. The effect on photocurrent or stability caused by dissolving V from the surface or the enrichment of Bi at the surface was not reported,[30] though it should be noted that Bi-enriched $BiVO_4$ surfaces were previously shown to improve photocurrent stability.[81] It should also be noted that while this treatment and the EC/chemical treatment discussed in the previous section[68] both apply cathodic potentials to reduce electrode material, the potential discussed here was only applied for a brief time before sweeping to higher (oxidizing) voltages, compared to holding -0.3 V_{RHE} for 3 min.[30,68] For this treatment, cathodic potentials (versus V^{4+}/V^{5+}, E_{app} < ~0.1 V_{RHE})[15] are only applied for ~6.5 s per scan before the sweep becomes anodic (~36.5 s for 0.1 < V_{RHE} < 1.2). It would seem that any reduction of V or other species within these $BiVO_4$ films is reversed by the oxidation involved in each sweep, with the exception of surface

Mo^{6+} which is apparently dissolved irreversibly into solution. Additional differing results between this treatment and the previously discussed EC scanning treatment[15] can be at least partially explained by the electrolytes used (sodium sulfate at pH 6.5 versus potassium borate at pH 9.4), as pH is known to strongly affect postsynthetic treatment.[37] However, direct experimental comparison would be needed to confirm these hypotheses. This electrochemical treatment was found to be stable after storing treated electrodes in air or vacuum for 12 h.[30]

While not strictly a postsynthetic treatment by our definition, etching of an NiO_x catalytic layer on $BiVO_4$ was proposed to block recombination sites ascribed to BiO_8 polyhedra at the electrode surface.[73,74] Computational modelling suggested that lattice distortions within the first ~2 nm of $BiVO_4$ surfaces create an environment favorable for hole trapping.[73] Bi^{3+} surface sites were reportedly blocked by the selective etching of nickel borate surface layers in a potassium phosphate solution.[74] The etching procedure exposed VO_4 sites while the remaining, non-catalytic NiO_x was primarily located on BiO_8 sites. The resulting films exhibited a significant improvement to φ_{inj}, improving the stable photocurrent at 1.23 V_{RHE} from 0.34 mA cm^{-2} to 1.09 mA cm^{-2},[74] and improving ABPE to 0.39% from 0.07 and 0.15% for untreated and NiO_x catalyzed films, respectively. A small improvement of φ_{sep} for both catalytic and etched $NiO_x/BiVO_4$ samples over bare $BiVO_4$ can be observed in photocurrent data with hole scavenger (sulfite) present.[74] This work emphasizes the crucial role of surface termination, particularly with multinary materials. Future work on this treatment could be directed towards improving the treatment route – e.g. by directing the passivating material to the recombination sites initially and removing

the need to etch – and investigating the surface chemistry of $BiVO_4$ (for example, the role of different exposed metal sites and the passivation mechanism of NiO_x sites).

These postsynthetic techniques target both the electrode-electrolyte interface and improve φ_{inj} by removing or blocking surface recombination sites, and represent facile approaches to enhance the performance of both doped and pristine $BiVO_4$ photoanodes.[30,74] These diverse results highlight that there is not a specific ideal surface termination since both Bi and V surface-rich terminations were observed with improved charge injection, depending on the particular report.

Near-surface doping and surface state alteration

In the near-surface regime (i.e. 2-10 nm),[73] partial reduction of V through photochemical treatment has been associated with improved φ_{sep} and φ_{inj}.[35–37] Photochemical treatments have been demonstrated with both ultra-violet (UV) and visible light and the resulting effects can be achieved either in or out of electrolyte, depending on the report.[35–37] Soaking $BiVO_4$ in $AgNO_3$ can also improve φ_{inj} significantly.[81]

Relatively early in the PEC research on $BiVO_4$, it was noticed that the photocurrent in pristine $BiVO_4$ decayed as much as 50% within 30 min, yet the photocurrent could be partially restored by cyclic voltammetry or storing the electrodes in the dark for 24 h.[81] Based on the existing knowledge of photoelectrode surface modifications, this work exposed $BiVO_4$ to a number of metal salts (0.01 M, 12 h) to adsorb metal ions into $BiVO_4$. Of the different salts tested, $AgNO_3$ solutions showed the most improvement in photocurrent. Following $AgNO_3$ treatment, φ_{inj} was improved to near-unity and φ_{sep} was slightly improved at high potentials (1.15-1.55 V_{RHE}); APBE was improved from 0.06 to

0.21%.[4] $BiVO_4$ treated with $AgNO_3$ demonstrated a stable photocurrent (1 h) plateauing at nearly twice the saturation photocurrent of untreated $BiVO_4$. Following an XPS analysis on the effect of 1 h of photoreaction (e.g. PEC water splitting) on treated and untreated $BiVO_4$, it was found that V dissolved from the surface of both treated and untreated samples; however, the surface of treated $BiVO_4$ was capped by a Bi-rich layer. The surface of $AgNO_3$ treated $BiVO_4$ was etched following photoreaction; beneath the surface, Bi and V were found to be stoichiometrically matched even with 1.8 at% Ag^+ present, and Bi was found to be both in the normal Bi^{3+} and reduced Bi^0 oxidation states; here it should be noted that by incorporating metal species to $BiVO_4$, this treatment is not strictly a postsynthetic treatment. The researchers attributed the improved photocurrent and stability to both the protective Bi-rich surface layer and the Ag^+ ion exchange layer formed at the surface of $AgNO_3$ treated $BiVO_4$.[81] Additionally, it was hypothesized that the addition of Ag^+ to the near-surface region of $BiVO_4$ would raise the VB maximum within this spatial region;[2,82] thus narrowing the bandgap and improving charge separation as well as absorption. Further evidence would be needed to support this hypothesis.

For W-doped $BiVO_4$ (W:$BiVO_4$), curing electrodes in air with UV light (~10 mW cm^{-2}, 20 h) significantly enhanced both φ_{sep} and φ_{inj} (Figure 1.5a).[35] The improvement of φ_{sep} was demonstrated by comparing photocurrents before and after treatment in the presence of a hole scavenger (H_2O_2). Evidence of φ_{inj} improvement was shown by the change in photovoltage from 0.17 to 0.41 V,[35,83] as well as the comparison of water oxidation photocurrents in relation to the photocurrents in a hole scavenger. UV-cured W:$BiVO_4$ films showed an improved ABPE for water oxidation (0.20%) over untreated samples

[4] Photocurrent was measured using an unfiltered Xe lamp with ca. 2.6 x AM 1.5G intensity. Therefore, 260 mW cm^{-2} was assumed as the illumination power.

(0.07%). The improvements of φ_{inj} were attributed to a change in the ratio of dangling to bridging (oxy)hydroxyl group surface groups at the electrolyte-electrode interface, where the amount of bridging O was increased following UV-curing. Alterations to film crystallinity and texture were also observed, and would be expected to affect φ_{sep}.[35] Further analysis on the effects of this treatment (e.g. defect chemistry, carrier kinetics) in relation to other photo(electro)chemical treatments could offer important insights into the differences between pristine and doped $BiVO_4$.

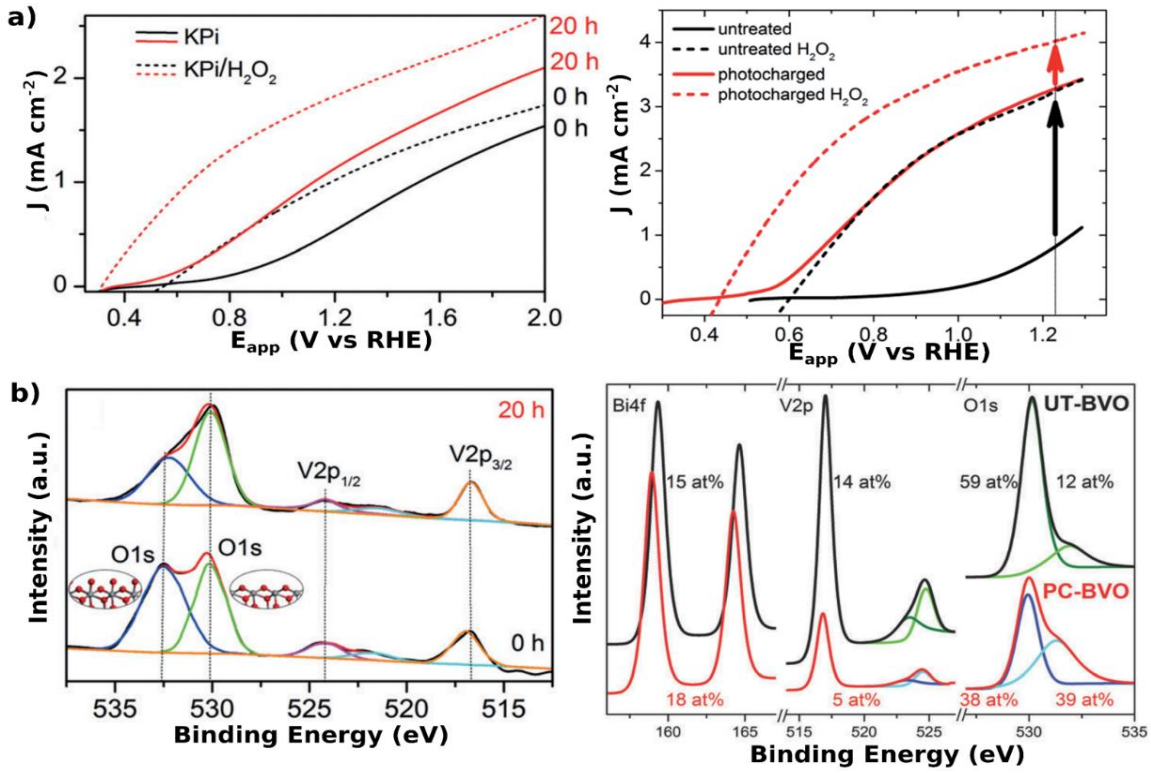

Figure 1.5 Photocharging *versus* UV-treated $BiVO_4$. a) left: Photocurrent densities of $BiVO_4$ photoanodes, before and after UV curing, with (solid) and without 0.1 m H_2O_2 (dashed), and right: J-V scans of $BiVO_4$ under back-side illumination. Arrows denote catalytic limitations for untreated (black) and photocharged (red) material. b) XPS of $BiVO_4$ with 0 h (black) and 20 h (red) UV curing (left); and of $BiVO_4$ photoanodes before and after photocharging in 0.1 M PBA buffer, pH 10 (right). Except where noted, samples measured in 0.1 M KPi and AM 1.5G illumination. Left-hand figures reproduced with permission from Reference 35 (© 2016 WILEY-VCH Verlag GmbH & Co. KGaA, Weinheim). Figure a(right) and b(right) reproduced with permission from References 36 and 37, respectively - Published by The Royal Society of Chemistry.

A separate light-based treatment was demonstrated to address the limitations of $BiVO_4$, denoted as 'photocharging',[36,37] which uses long-time exposure of the $BiVO_4$ photoanodes to AM 1.5G illumination under open circuit conditions in a cell filled with electrolyte. Photocharging leads to greatly enhanced photocurrent, a strong cathodic shift of the photocurrent onset, and improved J-V fill factor (Figure 1.5b). The photocharging-driven activation of $BiVO_4$ photoanodes is facilitated especially under alkaline conditions, with slightly alkaline electrolyte (pH 10) showing the greatest performance enhancements and slightly acidic media (pH 4) showing no effect following photocharging;[37] photocharged samples in pH 10 buffer were found to have an ABPE of 1.67%, versus an ABPE of 0.16% for untreated films. It is worth noting here that not all basic media are appropriate for $BiVO_4$-based electrodes; phosphate buffers especially are known to etch $BiVO_4$ to the detriment of film performance and stability.[15,71] The combination of requirements – principally alkaline electrolyte and visible light illumination – led to the conclusion that photogenerated holes ($h^{\bullet}$) and hydroxide ions cause two main effects; i) hydrogenation of the near-surface region, proposed as the formation of interstitial positively charged defects ($H_{int}^{\bullet}$), resulting in V^{4+} and oxygen vacancies ($v_O^{\bullet\bullet}$), and ii) saturation of the electrode surface with hydroxyl groups, which act as intermediates in the OER.[37] The proposed defect chemistry reaction, described using Kröger-Vink notation and shown in Equation

These surface and near-surface alterations result in a record high photocurrent for undoped and uncatalyzed $BiVO_4$ of 4.3 mA cm^{-2} at 1.23 V_{RHE}, an onset potential of 0.25 V_{RHE} corresponding to a doubling of the photovoltage, improved φ_{inj} and φ_{sep}, and near-unity internal quantum efficiency.[36,37] Electrochemical impedance spectroscopy (EIS) characterization suggests that photocharging leads to the formation of a surface capacitive layer, which has the ability to accumulate holes, and hence reduces the surface recombination. The formation of this capacitive layer involves the increase of hydroxyl groups at the surface and the partial reduction of vanadium 5+ to 4+, as supported by X-ray photoelectron spectroscopy (XPS) and X-ray absorption spectroscopy (XAS) measurements,[37] and more recently by intensity modulated photocurrent spectroscopy (IMPS).[38] IMPS results further elucidated that φ_{inj} improvements (caused by the aforementioned surface state changes) increased charge transfer while decreasing recombination (k_{WO} and k_{rec} in Equation 1.3, respectively).[38]

Contrary to the UV-curing study, which can enhance performance even when illuminated in air, photocharging could only be performed in an aqueous solution. While the surface states were observed to change following both treatments, the trends were opposite; i.e. increasing amount of dangling –OH surface sites in case of photocharging in an electrolyte and passivation of –OH in case of UV-curing in air (Figure 1.5b).[35,37] These differences between UV-cured W:$BiVO_4$ and photocharged $BiVO_4$ might be caused by either the differences in deposition method (sol-gel spin coating vs spray pyrolysis, respectively) which can cause different intrinsic surface or bulk defects,[36] or by the addition of W to $BiVO_4$ in the UV-curing case which is known to form extrinsic trap states.[20,34] As noted previously, doping $BiVO_4$ can cause significant alterations to the surface of $BiVO_4$;[30]

furthermore, doping $BiVO_4$ with W is known to form additional trap states (versus pristine $BiVO_4$), adversely affecting charge carrier mobilities and lifetimes.[20] More work is needed to confirm either of these hypotheses. Notably, the mechanism proposed for photocharging is very similar to that for H_2-annealed $BiVO_4$ and the role of hydrogen in $BiVO_4$, as discussed in the previous section.[33] Both treatments – H_2 annealing and photocharging – are proposed to introduce hydrogen defects (H_O, H_{int}) and v_O, as well as altering the surface states at the semiconductor-electrolyte interface. Both treatments have also been shown to improve φ_{sep} and increase the concentration of surface dangling –OH groups,[32,36] which were shown to improve φ_{inj} in photocharged samples.[37] In addition to the treatment conditions, the most significant difference between the electrodes is the localization of vanadium reduction to the near-surface (top 5-10 nm, based on XPS, XAS, and XANES results) of photocharged $BiVO_4$ compared to no reported localization in H_2-annealed $BiVO_4$. Similarities also exist between the photocharging treatment and some of the (photo)electrochemical treatments discussed in the previous section.[3,15,36,37] All of these treatments take place, optimally, in alkaline media and are accompanied by changes in the V oxidation state for an overall enhancement of photocurrent and improved onset potential. Indeed, the photocharging effect works best in alkaline media and not at all in acidic media.[37] Additionally, the initial report on photocharged $BiVO_4$ indicated that the treatment was reversible (i.e. unstable) when stored in the dark overnight in buffer;[36] however, EC-treated $BiVO_4$ was reported as stable over extended measurements (10 h PEC, 10 days in borate electrolyte), perhaps owing to the deposition of a catalytic layer following the electrochemical treatment.[15]

These similarities point towards a relationship between three effective postsynthetic treatments for improving the PEC efficiency of $BiVO_4$, where H_2 annealing, photocharging, and electrochemical treatments achieve similar results based on possibly related underlying mechanisms.[3,15,33,34,37] Further data are needed to develop a deeper understanding and to find the most effective treatments for further performance gains. Bringing new measurement techniques to bare on $BiVO_4$ will certainly help illuminate changes.[84–86]

Summary

Postsynthetic treatments offer powerful ways of removing a variety of surface recombination sites and improving (near)-surface kinetic properties of $BiVO_4$-based photoanodes. Importantly, the type of defect present (and therefore the synthetic method utilized) has a significant impact on the effectiveness of a given technique. For example, two similar treatments – UV curing and photocharging – are not interchangeable and seem to have opposite effects on different $BiVO_4$-based electrodes.[37] Likewise, two seemingly disparate treatments – PEC activation (oxidation) and electrochemical cycling – both improve electrodes similarly, presumably because the initial-state after synthesis has different native defects.[3,30] Therefore, as research on $BiVO_4$ electrodes continues, it is important to carefully characterize the types and location of defects present within $BiVO_4$ before and after treatments. This is especially important when comparing different synthetic routes, but is equally relevant for the same synthesis where small changes to instrumentation can produce significantly different materials.[34]

Theoretical limits

Enhanced theoretical models[87] based on the detailed balance concept[88] predict fundamental prospects of solar water splitting devices and enable precise guidance for their

development.[89] These models include fundamentally inevitable losses such as radiative recombination, thermalization, and transmission. However, oxide materials with highly non-ideal semiconductor properties, such as $BiVO_4$, still represent significant challenges for both theoretical prediction and experimental implementation. Figure 1.6a compares the idealized optoelectronic performance limit for $BiVO_4$ (black line, in a hypothetical PV configuration) with present day record current-voltage characteristics (red/blue lines, PEC configuration, see also Figure 1.2). The theoretical calculation (black line, Figure 1.6a) assumes idealized material by neglect of nonradiative recombination, of lattice imperfections, and of system losses (including catalysis, band offsets, resistances, etc.) that largely diminish the performance of experimental $BiVO_4$ PEC devices. Fundamentally, its 2.4 eV band gap (E_{bg}) enables $BiVO_4$ to provide up to 2.1 V open circuit voltage (V_{oc}) and 14.5% PV efficiency at a load of about 1.95 V (maximum power point, mpp). In the light of more than 700 mV sacrificial overvoltage (in excess of the thermodynamic water splitting potential of 1.23 V) even bias-free PEC operation of a single-junction absorber may appear conceivable. However, a single-junction approach has not been achieved in practice due to major material deficiencies (recombination and poor band alignment) demanding a much higher overvoltage budget.

Experimental PEC performance of $BiVO_4$ (Figures. 1.2 & 1.6a) lags far behind that ideal, but at least positive net energy contributions (up to ~2% APBE, see above)[13,15] have been realized. Present and future development deals with three major bottlenecks restricting solar-to-hydrogen (STH) energy conversion with $BiVO_4$: (i) non-radiative recombination, (ii) unfavorable band alignment, and (iii) an excessively large band gap energy. Engineering solutions such as host-guest architecture[14,45,55] decouple the mismatch

of diffusion and absorption lengths enabling impressive photocurrents (Figure 1.6a, line III).[5] Gradient doping improves charge carrier extraction,[27] and thus effectively further suppresses the impact of non-radiative recombination events towards a more rectangular IV characteristic (Figure 1.6a, line IV). Both concepts also promise minor improvements of the photocurrent onset potential (Figure 1.6a, line III), but are limited by the intrinsically non-ideal band alignment of $BiVO_4$ to the water oxidation/reduction potentials.

A priori, the transfer between absolute PV (upper axis) and relative PEC (lower axis) potential metrics (Figure 1.6a, line I) remains unclear. Despite its high band gap and theoretical voltage prospects, $BiVO_4$ is considered incapable of driving unbiased water splitting as its band edges do not straddle both water splitting half-reaction potentials.[90] However, appropriate engineering solutions such as surface modification with dipoles[91] or a buried p-n junction[89] may lessen or even resolve the misalignment. Tandem operation represents a more practical solution already demonstrated today.[27,92,93] Utilization of inevitable transmission losses (photons <2.4 eV) by a subsequently absorbing bottom PV structure may provide plenty additional (built-in bias) voltage. Figure 1.6b maps detailed balance tandem STH efficiency limits over both top and bottom absorber band gaps. Optimum structures may tolerate up to 2.3 V of overvoltage loss before severely restricting the performance prospects. The popular concept of combining $BiVO_4$ with multiple bottom junctions accommodates even higher losses.[27,92,93] Achieved performance gains indirectly demonstrate insufficient material quality of concurrent $BiVO_4$, where its I-V characteristics virtually never saturate to a light-limited photocurrent regime with low applied bias.

[5] We cannot exclude a certain level of overestimation in literature data,[92] but the significance of the achievements remains obvious.

Engineering concepts promise to combine more ideal performance with better photocurrent onset.

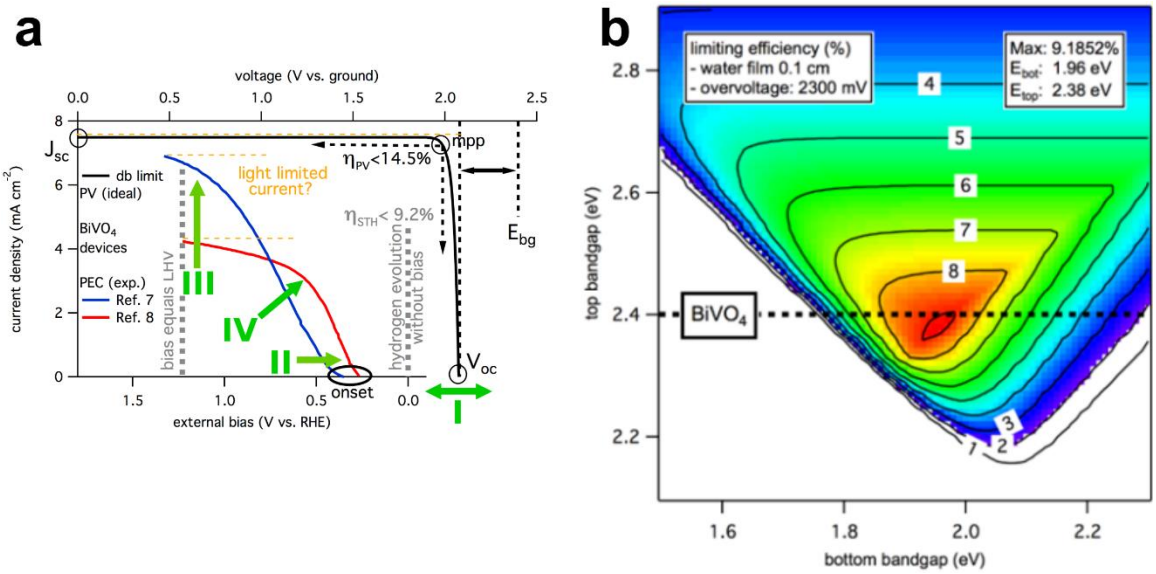

Figure 1.6 (a) Comparison of I-V characteristics of experimental $BiVO_4$ PEC devices (blue/red, bottom axis) relative to the theoretical detailed balance limit for $BiVO_4$ photovoltaics (black, top axis); and (b) detailed balance contour plots of the fundamental solar-to-hydrogen conversion efficiency limit for dual-junction water-splitting devices over the bandgap energies of top and bottom absorber material for thin (1 mm) illumination length through the electrolyte and high (2300 mV) overvoltage loss.

Conclusions

Bismuth vanadate is a well-studied and interesting material for use in solar-assisted water splitting. Recently, a variety of postsynthetic modifications have emerged to improve the ABPE performance of $BiVO_4$. Postsynthetic treatments have provided insights into $BiVO_4$ defect chemistry at the surface and within the bulk of the material, yielding significant enhancements to charge injection and charge separation, respectively. Importantly, it has become apparent that probing the oxidation states by XPS alone cannot distinguish between the multiple posited changes to defect chemistries. For example thermal hydrogenation,[31,33,34] proton intercalation,[36,37] production of oxygen vacancies,[13,31,36,37] and electrochemical reduction[15,68] all are expected to yield reduced

vanadium states. XPS measurements of vanadium oxidation states alone are not sufficient to distinguish between these various defect mechanisms. New insights will be drawn from future studies that attempt to parse these multiple causal pathways in the presently reported observations. Techniques to probe local electronic environments, e.g. solid-state NMR (^{1}H, ^{51}V, and ^{209}Bi),[33,94–96] Raman and IR spectroscopy,[94,97] electron energy loss spectroscopy (EELS),[63–65] STEM,[64,98] and X-ray absorption near edge structure (XANES)[66] – could be used in conjunction with computational methodologies to identify changes to specific defect chemistries. Here, inelastic X-ray techniques have yielded recent insights into changes at the $BiVO_4$/electrolyte interface[84,86] and to electronic structure with changing defect chemistry.[11,85,99,100] Once the defects are identified with specificity, then techniques that probe charge carrier dynamics (such as transient diffuse reflectance and time-resolved conductivity)[23,34] or trap states (such as photoluminescence)[33] could provide valuable insights into the role of those defects sites (e.g. catalytic site, trap site, and/or donor). Beyond immediate performance, postsynthetic treatments may also elucidate possible electrode changes under extended service and provide new strategies to enable extended device performance, furthering the development of commercial PEC water splitting devices.

Acknowledgements

We would like to acknowledge support from the University of South Carolina for startup funds and the USC ASPIRE grant, and from the Leon Schechter Endowed Fellowship for Polymer Nanocomposites.

References

(1) Lamm, B.; Trześniewski, B. J.; Döscher, H.; Smith, W. A.; Stefik, M. Emerging Postsynthetic Improvements of BiVO 4 Photoanodes for Solar Water Splitting. *ACS*

Energy Lett. **2018**, *3*, 112–124.

(2) Park, Y.; McDonald, K. J.; Choi, K.-S. Progress in Bismuth Vanadate Photoanodes for Use in Solar Water Oxidation. *Chem. Soc. Rev.* **2013**, *42*, 2321–2337.

(3) Lamm, B.; Sarkar, A.; Stefik, M. Surface Functionalized Atomic Layer Deposition of Bismuth Vanadate for Single-Phase Scheelite. *J. Mater. Chem. A* **2017**, *5*, 6060–6069.

(4) Lamm, B.; Zhou, L.; Rao, P.; Stefik, M. Atomic Layer Deposition of Space-Efficient SnO 2 Underlayers for BiVO 4 Host-Guest Architectures for Photoassisted Water Splitting. *ChemSusChem* **2019**. DOI: 10.1002/cssc.201802566.

(5) Sarkar, A. Block Copolymer Control of Nanoscale Porous Materials, University of South Carolina, 2018.

(6) Lantz, K. A.; Sarkar, A.; Littrell, K. C.; Li, T.; Hong, K.; Stefik, M. Cavitation Enables Switchable and Rapid Block Polymer Exchange under High-χ N Conditions. *Macromolecules* **2018**, *51*, 6967–6975.

(7) Sarkar, A.; Evans, L.; Stefik, M. Expanded Kinetic Control for Persistent Micelle Templates with Solvent Selection. *Langmuir* **2018**, *34*, 5738–5749.

(8) Sarkar, A.; Stefik, M. How to Make Persistent Micelle Templates in 24 Hours and Know It Using X-Ray Scattering. *J. Mater. Chem. A* **2017**, *5*, 11840–11853.

(9) Kudo, A.; Ueda, K.; Kato, H.; Mikami, I. Photocatalytic O_2 Evolution under Visible Light Irradiation on $BiVO_4$ in Aqueous $AgNO_3$ Solution. *Catal. Letters* **1998**, *53*, 229–230.

(10) Tokunaga, S.; Kato, H.; Kudo, A. Selective Preparation of Monoclinic and Tetragonal $BiVO_4$ with Scheelite Structure and Their Photocatalytic Properties.

Chem. Mater. **2001**, *13*, 4624–4628.

(11) Cooper, J. K.; Gul, S.; Toma, F. M.; Chen, L.; Liu, Y.-S. S.; Guo, J.; Ager, J. W.; Yano, J.; Sharp, I. D. Indirect Bandgap and Optical Properties of Monoclinic Bismuth Vanadate. *J. Phys. Chem. C* **2015**, *119*, 2969–2974.

(12) Walter, M. G.; Warren, E. L.; McKone, J. R.; Boettcher, S. W.; Mi, Q.; Santori, E. A.; Lewis, N. S. Solar Water Splitting Cells. *Chem. Rev.* **2010**, *110*, 6446–6473.

(13) Kim, T. W.; Ping, Y.; Galli, G. A.; Choi, K.-S. Simultaneous Enhancements in Photon Absorption and Charge Transport of Bismuth Vanadate Photoanodes for Solar Water Splitting. *Nat. Commun.* **2015**, *6*, 8769.

(14) Pihosh, Y.; Turkevych, I.; Mawatari, K.; Uemura, J.; Kazoe, Y.; Kosar, S.; Makita, K.; Sugaya, T.; Matsui, T.; Fujita, D.; *et al.* Photocatalytic Generation of Hydrogen by Core-Shell $WO_3/BiVO_4$ Nanorods with Ultimate Water Splitting Efficiency. *Sci. Rep.* **2015**, *5*, 11141.

(15) Kuang, Y.; Jia, Q.; Nishiyama, H.; Yamada, T.; Kudo, A.; Domen, K. A Front-Illuminated Nanostructured Transparent $BiVO_4$ Photoanode for >2% Efficient Water Splitting. *Adv. Energy Mater.* **2016**, *6*, 1501645.

(16) Dotan, H.; Sivula, K.; Grätzel, M.; Rothschild, A.; Warren, S. C. Probing the Photoelectrochemical Properties of Hematite (α-Fe_2O_3) Electrodes Using Hydrogen Peroxide as a Hole Scavenger. *Energy Environ. Sci.* **2011**, *4*, 958–964.

(17) Zhong, D. K.; Choi, S.; Gamelin, D. R. Near-Complete Suppression of Surface Recombination in Solar Photoelectrolysis by "Co-Pi" Catalyst-Modified W:$BiVO_4$. *J. Am. Chem. Soc.* **2011**, *133*, 18370–18377.

(18) Liang, Y.; Tsubota, T.; Mooij, L. P. A.; van de Krol, R. Highly Improved Quantum

Efficiencies for Thin Film BiVO4 Photoanodes. *J. Phys. Chem. C* **2011**, *115*, 17594–17598.

(19) Abdi, F. F.; Van De Krol, R. Nature and Light Dependence of Bulk Recombination in Co-Pi-Catalyzed $BiVO_4$ Photoanodes. *J. Phys. Chem. C* **2012**, *116*, 9398–9404.

(20) Abdi, F. F.; Savenije, T. J.; May, M. M.; Dam, B.; van de Krol, R. The Origin of Slow Carrier Transport in BiVO 4 Thin Film Photoanodes: A Time-Resolved Microwave Conductivity Study. *J. Phys. Chem. Lett.* **2013**, *4*, 2752–2757.

(21) Ravensbergen, J.; Abdi, F. F.; van Santen, J. H.; Frese, R. N.; Dam, B.; van de Krol, R.; Kennis, J. T. M. Unraveling the Carrier Dynamics of $BiVO_4$: A Femtosecond to Microsecond Transient Absorption Study. *J. Phys. Chem. C* **2014**, *118*, 27793–27800.

(22) Butler, K. T.; Dringoli, B. J.; Zhou, L.; Rao, P. M.; Walsh, A.; Titova, L. V. Ultrafast Carrier Dynamics in $BiVO_4$ Thin Film Photoanode Material: Interplay between Free Carriers, Trapped Carriers and Low-Frequency Lattice Vibrations. *J. Mater. Chem. A* **2016**, *4*, 18516–18523.

(23) Suzuki, Y.; Murthy, D. H. K.; Matsuzaki, H.; Furube, A.; Wang, Q.; Hisatomi, T.; Domen, K.; Seki, K. Rational Interpretation of Correlated Kinetics of Mobile and Trapped Charge Carriers: Analysis of Ultrafast Carrier Dynamics in $BiVO_4$. *J. Phys. Chem. C* **2017**, *121*, 19044–19052.

(24) Ma, Y.; Pendlebury, S. R.; Reynal, A.; Le Formal, F.; Durrant, J. R. Dynamics of Photogenerated Holes in Undoped $BiVO_4$ Photoanodes for Solar Water Oxidation. *Chem. Sci.* **2014**, *5*, 2964–2973.

(25) Kim, T. W.; Choi, K.-S. K.-S. Nanoporous $BiVO_4$ Photoanodes with Dual-Layer

Oxygen Evolution Catalysts for Solar Water Splitting. *Science.* **2014**, *343*, 990–994.

(26) Zachäus, C.; Abdi, F. F.; Peter, L. M.; van de Krol, R. Photocurrent of $BiVO_4$ Is Limited by Surface Recombination, Not Surface Catalysis. *Chem. Sci.* **2017**, *8*, 3712–3719.

(27) Abdi, F. F.; Han, L.; Smets, A. H. M.; Zeman, M.; Dam, B.; van de Krol, R. Efficient Solar Water Splitting by Enhanced Charge Separation in a Bismuth Vanadate-Silicon Tandem Photoelectrode. *Nat. Commun.* **2013**, *4*, 2195–2202.

(28) Tolod, K.; Hernández, S.; Russo, N. Recent Advances in the $BiVO_4$ Photocatalyst for Sun-Driven Water Oxidation: Top-Performing Photoanodes and Scale-Up Challenges. *Catalysts* **2017**, *7*, 13.

(29) Tan, H. L.; Amal, R.; Ng, Y. H. Alternative Strategies in Improving the Photocatalytic and Photoelectrochemical Activities of Visible Light-Driven $BiVO_4$: A Review. *J. Mater. Chem. A* **2017**, *5*, 16498–16521.

(30) Luo, W.; Li, Z.; Yu, T.; Zou, Z. Effects of Surface Electrochemical Pretreatment on the Photoelectrochemical Performance of Mo-Doped $BiVO_4$. *J. Phys. Chem. C* **2012**, *116*, 5076–5081.

(31) Wang, G.; Ling, Y.; Lu, X.; Qian, F.; Tong, Y.; Zhang, J. Z.; Lordi, V.; Rocha Leao, C.; Li, Y. Computational and Photoelectrochemical Study of Hydrogenated Bismuth Vanadate. *J. Phys. Chem. C* **2013**, *117*, 10957–10964.

(32) Singh, A. P.; Kodan, N.; Dey, A.; Krishnamurthy, S.; Mehta, B. R. Improvement in the Structural, Optical, Electronic and Photoelectrochemical Properties of Hydrogen Treated Bismuth Vanadate Thin Films. *Int. J. Hydrogen Energy* **2015**, *40*, 4311–4319.

(33) Cooper, J. K.; Scott, S. B.; Ling, Y.; Yang, J.; Hao, S.; Li, Y.; Toma, F. M.; Stutzmann, M.; Lakshmi, K. V.; Sharp, I. D. Role of Hydrogen in Defining the N-Type Character of $BiVO_4$ Photoanodes. *Chem. Mater.* **2016**, *28*, 5761–5771.

(34) Jang, J.-W. W.; Friedrich, D.; Müller, S.; Lamers, M.; Hempel, H.; Lardhi, S.; Cao, Z.; Harb, M.; Cavallo, L.; Heller, R.; *et al.* Enhancing Charge Carrier Lifetime in Metal Oxide Photoelectrodes through Mild Hydrogen Treatment. *Adv. Energy Mater.* **2017**, *7*, 1701536.

(35) Li, T.; He, J.; Peña, B.; Berlinguette, C. P. Curing $BiVO_4$ Photoanodes with Ultraviolet Light Enhances Photoelectrocatalysis. *Angew. Chemie Int. Ed.* **2016**, *55*, 1769–1772.

(36) Trześniewski, B. J.; Smith, W. A. Photocharged BiVO 4 Photoanodes for Improved Solar Water Splitting. *J. Mater. Chem. A* **2016**, *4*, 2919–2926.

(37) Trześniewski, B. J.; Digdaya, I. A.; Nagaki, T.; Ravishankar, S.; Herraiz-Cardona, I.; Vermaas, D. A.; Longo, A.; Gimenez, S.; Smith, W. A. Near-Complete Suppression of Surface Losses and Total Internal Quantum Efficiency in $BiVO_4$ Photoanodes. *Energy Environ. Sci.* **2017**, *10*, 1517–1529.

(38) Liu, E. Y.; Thorne, J. E.; He, Y.; Wang, D. Understanding Photocharging Effects on Bismuth Vanadate. *ACS Appl. Mater. Interfaces* **2017**, *9*, 22083–22087.

(39) Ding, J.; Dai, Z.; Tian, F.; Zhou, B.; Zhao, B.; Zhao, H.; Chen, Z.; Liu, Y.; Chen, R. Generation of $V_{Br}^{\bullet}V_{Bi}^{'''}V_O^{\bullet\bullet}$ Defect Cluster for $^1O_2$ Production in Molecular Oxygen Activation of Photocatalysis. *J. Mater. Chem. A* **2017**. DOI: 10.1039/C7TA08117K.

(40) Parmar, K. P. S.; Kang, H. J.; Bist, A.; Dua, P.; Jang, J. S.; Lee, J. S. Photocatalytic and Photoelectrochemical Water Oxidation over Metal-Doped Monoclinic $BiVO_4$

Photoanodes. *ChemSusChem* **2012**, *5*, 1926–1934.

(41) Eisenberg, D.; Ahn, H. S.; Bard, A. J. Enhanced Photoelectrochemical Water Oxidation on Bismuth Vanadate by Electrodeposition of Amorphous Titanium Dioxide. *J. Am. Chem. Soc.* **2014**, *136*, 14011–14014.

(42) Zhang, L.; Ye, X.; Boloor, M.; Poletayev, A.; Melosh, N. A.; Chueh, W. C. Significantly Enhanced Photocurrent for Water Oxidation in Monolithic Mo:$BiVO_4$/SnO_2/Si by Thermally Increasing the Minority Carrier Diffusion Length. *Energy Environ. Sci.* **2016**, *9*, 2044–2052.

(43) Gutkowski, R.; Khare, C.; Conzuelo, F.; Kayran, Y. U.; Ludwig, A.; Schuhmann, W. Unraveling Compositional Effects on the Light-Induced Oxygen Evolution in Bi(V–Mo–X)O_4 Material Libraries. *Energy Environ. Sci.* **2017**, *10*, 1213–1221.

(44) Kalanur, S. S.; Yoo, I.-H.; Park, J.; Seo, H. Insights into the Electronic Bands of WO_3/$BiVO_4$/TiO_2, Revealing High Solar Water Splitting Efficiency. *J. Mater. Chem. A* **2017**, *5*, 1455–1461.

(45) Shi, X.; Choi, I. Y.; Zhang, K.; Kwon, J.; Kim, D. Y.; Lee, J. K.; Oh, S. H.; Kim, J. K.; Park, J. H. Efficient Photoelectrochemical Hydrogen Production from Bismuth Vanadate-Decorated Tungsten Trioxide Helix Nanostructures. *Nat. Commun.* **2014**, *5*, 4775–4783.

(46) Galembeck, A.; Alves, O. L. $BiVO_4$ Thin Film Preparation by Metalorganic Decomposition. *Thin Solid Films* **2000**, *365*, 90–93.

(47) Seabold, J. A.; Choi, K.-S. Efficient and Stable Photo-Oxidation of Water by a Bismuth Vanadate Photoanode Coupled with an Iron Oxyhydroxide Oxygen Evolution Catalyst. *J. Am. Chem. Soc.* **2012**, *134*, 2186–2192.

(48) Chen, L.; Alarcón-Lladó, E.; Hettick, M.; Sharp, I. D.; Lin, Y.; Javey, A.; Ager, J. W. Reactive Sputtering of Bismuth Vanadate Photoanodes for Solar Water Splitting. *J. Phys. Chem. C* **2013**, *117*, 21635–21642.

(49) Gong, H.; Freudenberg, N.; Nie, M.; Van De Krol, R.; Ellmer, K. $BiVO_4$ Photoanodes for Water Splitting with High Injection Efficiency, Deposited by Reactive Magnetron Co-Sputtering. *AIP Adv.* **2016**, *6*, 045108.

(50) Alarcón-Lladó, E.; Chen, L.; Hettick, M.; Mashouf, N.; Lin, Y.; Javey, A.; Ager, J. W. $BiVO_4$ Thin Film Photoanodes Grown by Chemical Vapor Deposition. *Phys. Chem. Chem. Phys.* **2014**, *16*, 1651–1657.

(51) Stefik, M. Atomic Layer Deposition of Bismuth Vanadates for Solar Energy Materials. *ChemSusChem* **2016**, *9*, 1727–1735.

(52) Zhang, L.; Reisner, E.; Baumberg, J. J. Al-Doped ZnO Inverse Opal Networks as Efficient Electron Collectors in $BiVO_4$ Photoanodes for Solar Water Oxidation. *Energy Environ. Sci.* **2014**, *7*, 1402.

(53) Su, J.; Guo, L.; Bao, N.; Grimes, C. A. Nanostructured $WO_3/BiVO_4$ Heterojunction Films for Efficient Photoelectrochemical Water Splitting. *Nano Lett.* **2011**, *11*, 1928–1933.

(54) Zhou, L.; Zhao, C.; Giri, B.; Allen, P.; Xu, X.; Joshi, H.; Fan, Y.; Titova, L. V.; Rao, P. M. High Light Absorption and Charge Separation Efficiency at Low Applied Voltage from Sb-Doped SnO2/BiVO4 Core/Shell Nanorod-Array Photoanodes. *Nano Lett.* **2016**, *16*, 3463–3474.

(55) Zhou, L.; Yang, Y.; Zhang, J.; Rao, P. M. Photoanode with Enhanced Performance Achieved by Coating $BiVO_4$ onto ZnO-Templated Sb-Doped SnO_2 Nanotube

Scaffold. *ACS Appl. Mater. Interfaces* **2017**, *9*, 11356–11362.

(56) *CRC Handbook of Chemistry and Physics*; Hayes, W.; Lide, D. R., Eds.; 92nd ed.; Taylor & Francis: Boca Raton, 2011.

(57) Schuisky, M.; Kukli, K.; Ritala, M.; Hårsta, A.; Leskelä, M. Atomic Layer CVD in the Bi–Ti–O System. *Chem. Vap. Depos.* **2000**, *6*, 139–145.

(58) Fidelsky, V.; Toroker, M. C. Enhanced Water Oxidation Catalysis of Nickel Oxyhydroxide through the Addition of Vacancies. *J. Phys. Chem. C* **2016**, *120*, 25405–25410.

(59) Diaz-Morales, O.; Ferrus-Suspedra, D.; Koper, M. T. M. The Importance of Nickel Oxyhydroxide Deprotonation on Its Activity towards Electrochemical Water Oxidation. *Chem. Sci.* **2016**, *7*, 2639–2645.

(60) Wang, G.; Ling, Y.; Wang, H.; Yang, X.; Wang, C.; Zhang, J. Z.; Li, Y. Hydrogen-Treated WO_3 Nanoflakes Show Enhanced Photostability. *Energy Environ. Sci.* **2012**, *5*, 6180.

(61) Wang, G.; Wang, H.; Ling, Y.; Tang, Y.; Yang, X.; Fitzmorris, R. C.; Wang, C.; Zhang, J. Z.; Li, Y. Hydrogen-Treated TiO_2 Nanowire Arrays for Photoelectrochemical Water Splitting. *Nano Lett.* **2011**, *11*, 3026–3033.

(62) Lu, X.; Wang, G.; Xie, S.; Shi, J.; Li, W.; Tong, Y.; Li, Y. Efficient Photocatalytic Hydrogen Evolution over Hydrogenated ZnO Nanorod Arrays. *Chem. Commun.* **2012**, *48*, 7717.

(63) Zhao, Z.; Li, Z.; Zou, Z. Structure and Energetics of Low-Index Stoichiometric Monoclinic Clinobisvanite $BiVO_4$ Surfaces. *RSC Adv.* **2011**, *1*, 874.

(64) Rossell, M. D.; Agrawal, P.; Borgschulte, A.; Hébert, C.; Passerone, D.; Erni, R.

Direct Evidence of Surface Reduction in Monoclinic $BiVO_4$. *Chem. Mater.* **2015**, *27*, 3593–3600.

(65) Torruella, P.; Coll, C.; Martín, G.; López-Conesa, L.; Vila, M.; Díaz-Guerra, C.; Varela, M.; Ruiz-González, M. L.; Piqueras, J.; Peiró, F.; *et al.* Assessing Oxygen Vacancies in Bismuth Oxide through EELS Measurements and DFT Simulations. *J. Phys. Chem. C* **2017**. DOI: 10.1021/acs.jpcc.7b06310.

(66) Pattengale, B.; Ludwig, J.; Huang, J. Atomic Insight into the W-Doping Effect on Carrier Dynamics and Photoelectrochemical Properties of $BiVO_4$ Photoanodes. *J. Phys. Chem. C* **2016**, *120*, 1421–1427.

(67) Nair, V.; Perkins, C. L.; Lin, Q.; Law, M. Textured Nanoporous Mo:$BiVO_4$ Photoanodes with High Charge Transport and Charge Transfer Quantum Efficiencies for Oxygen Evolution. *Energy Environ. Sci.* **2016**, *9*, 1412–1429.

(68) Qin, D.-D.; Wang, T.; Song, Y.-M.; Tao, C.-L. Reduced Monoclinic $BiVO_4$ for Improved Photoelectrochemical Oxidation of Water under Visible Light. *Dalt. Trans.* **2014**, *43*, 7691.

(69) Venkatesan, R.; Velumani, S.; Tabellout, M.; Errien, N.; Kassiba, A. Dielectric Behavior, Conduction and EPR Active Centres in $BiVO_4$ Nanoparticles. *J. Phys. Chem. Solids* **2013**, *74*, 1695–1702.

(70) Yin, W.-J.; Wei, S.-H.; Al-Jassim, M. M.; Turner, J.; Yan, Y. Doping Properties of Monoclinic $BiVO_4$ Studied by First-Principles Density-Functional Theory. *Phys. Rev. B* **2011**, *83*, 155102.

(71) Toma, F. M.; Cooper, J. K.; Kunzelmann, V.; McDowell, M. T.; Yu, J.; Larson, D. M.; Borys, N. J.; Abelyan, C.; Beeman, J. W.; Yu, K. M.; *et al.* Mechanistic Insights

into Chemical and Photochemical Transformations of Bismuth Vanadate Photoanodes. *Nat. Commun.* **2016**, *7*, 12012.

(72) Rettie, A. J. E.; Chemelewski, W. D.; Emin, D.; Mullins, C. B. Unravelling Small-Polaron Transport in Metal Oxide Photoelectrodes. *J. Phys. Chem. Lett.* **2016**, *7*, 471–479.

(73) Kweon, K. E.; Hwang, G. S. Surface Structure and Hole Localization in Bismuth Vanadate: A First Principles Study. *Appl. Phys. Lett.* **2013**, *103*, 131603.

(74) Liang, Y.; Messinger, J. Improving $BiVO_4$ Photoanodes for Solar Water Splitting through Surface Passivation. *Phys. Chem. Chem. Phys.* **2014**, *16*, 12014.

(75) McDowell, M. T.; Lichterman, M. F.; Spurgeon, J. M.; Hu, S.; Sharp, I. D.; Brunschwig, B. S.; Lewis, N. S. Improved Stability of Polycrystalline Bismuth Vanadate Photoanodes by Use of Dual-Layer Thin TiO_2/Ni Coatings. *J. Phys. Chem. C* **2014**, *118*, 19618–19624.

(76) Jeon, T. H.; Choi, W.; Park, H. Cobalt–phosphate Complexes Catalyze the Photoelectrochemical Water Oxidation of $BiVO_4$ Electrodes. *Phys. Chem. Chem. Phys.* **2011**, *13*, 21392.

(77) Lai, Y.-H. H.; Palm, D. W.; Reisner, E. Multifunctional Coatings from Scalable Single Source Precursor Chemistry in Tandem Photoelectrochemical Water Splitting. *Adv. Energy Mater.* **2015**, *5*, 1501668.

(78) Choi, S. K.; Choi, W.; Park, H. Solar Water Oxidation Using Nickel-Borate Coupled $BiVO_4$ Photoelectrodes. *Phys. Chem. Chem. Phys.* **2013**, *15*, 6499.

(79) Ding, C.; Shi, J.; Wang, D.; Wang, Z.; Wang, N.; Liu, G.; Xiong, F.; Li, C. Visible Light Driven Overall Water Splitting Using Cocatalyst/$BiVO_4$ Photoanode with

Minimized Bias. *Phys. Chem. Chem. Phys.* **2013**, *15*, 4589.

(80) Li, M.; Luo, W.; Liu, B.; Zhao, X.; Li, Z.; Chen, D.; Yu, T.; Xie, Z.; Zhang, R.; Zou, Z. Remarkable Enhancement in Photocurrent of $In_{0.20}Ga_{0.80}N$ Photoanode by Using an Electrochemical Surface Treatment. *Appl. Phys. Lett.* **2011**, *99*, 112108.

(81) Sayama, K.; Nomura, A.; Arai, T.; Sugita, T.; Abe, R.; Oi, T.; Iwasaki, Y.; Abe, Y.; Sugihara, H. Photoelectrochemical Decomposition of Water into H_2 and O_2 on Porous $BiVO_4$ Thin-Film Electrodes under Visible Light and Significant Effect of Ag Ion Treatment. *J. Phys. Chem. B* **2006**, *110*, 11352–11360.

(82) Walsh, A.; Yan, Y.; Huda, M. N.; Al-Jassim, M. M.; Wei, S.-H. Band Edge Electronic Structure of $BiVO_4$: Elucidating the Role of the Bi s and V d Orbitals. *Chem. Mater.* **2009**, *21*, 547–551.

(83) Rajeshwar, K. Fundamentals of Semiconductor Electrochemistry and Photoelectrochemistry. In *Encyclopedia of Electrochemistry*; Wiley-VCH Verlag GmbH & Co. KGaA: Weinheim, Germany, 2007; pp. 1–51.

(84) Starr, D. E.; Favaro, M.; Abdi, F. F.; Bluhm, H.; Crumlin, E. J.; van de Krol, R. Combined Soft and Hard X-Ray Ambient Pressure Photoelectron Spectroscopy Studies of Semiconductor/Electrolyte Interfaces. *J. Electron Spectros. Relat. Phenomena* **2017**. DOI: 10.1016/j.elspec.2017.05.003.

(85) Jovic, V.; Laverock, J.; Rettie, A. J. E.; Zhou, J.-S.; Mullins, C. B.; Singh, V. R.; Lamoureux, B.; Wilson, D.; Su, T.-Y.; Jovic, B.; *et al.* Soft X-Ray Spectroscopic Studies of the Electronic Structure of M:$BiVO_4$ (M = Mo, W) Single Crystals. *J. Mater. Chem. A* **2015**, *3*, 23743–23753.

(86) Favaro, M.; Abdi, F. F.; Lamers, M.; Crumlin, E. J.; Liu, Z.; van de Krol, R.; Starr,

D. E. Light-Induced Surface Reactions at the Bismuth Vanadate/Potassium Phosphate Interface. *J. Phys. Chem. B* **2018**, *122*, 801–809.

(87) Döscher, H.; Geisz, J. F.; Deutsch, T. G.; Turner, J. A. Sunlight Absorption in Water – Efficiency and Design Implications for Photoelectrochemical Devices. *Energy Environ. Sci.* **2014**, *7*, 2951–2956.

(88) Shockley, W.; Queisser, H. J. Detailed Balance Limit of Efficiency of P-n Junction Solar Cells. *J. Appl. Phys.* **1961**, *32*, 510–519.

(89) Young, J. L.; Steiner, M. A.; Döscher, H.; France, R. M.; Turner, J. A.; Deutsch, T. G. Direct Solar-to-Hydrogen Conversion via Inverted Metamorphic Multi-Junction Semiconductor Architectures. *Nat. Energy* **2017**, *2*, 17028.

(90) Zhou, M.; Bao, J.; Bi, W.; Zeng, Y.; Zhu, R.; Tao, M.; Xie, Y. Efficient Water Splitting via a Heteroepitaxial $BiVO_4$ Photoelectrode Decorated with Co-Pi Catalysts. *ChemSusChem* **2012**, *5*, 1420–1425.

(91) Garner, L. E.; Steirer, K. X.; Young, J. L.; Anderson, N. C.; Miller, E. M.; Tinkham, J. S.; Deutsch, T. G.; Sellinger, A.; Turner, J. A.; Neale, N. R. Covalent Surface Modification of Gallium Arsenide Photocathodes for Water Splitting in Highly Acidic Electrolyte. *ChemSusChem* **2017**, *10*, 767–773.

(92) Döscher, H.; Young, J. L.; Geisz, J. F.; Turner, J. A.; Deutsch, T. G. Solar-to-Hydrogen Efficiency: Shining Light on Photoelectrochemical Device Performance. *Energy Environ. Sci.* **2016**, *9*, 74–80.

(93) Zhang, K.; Ma, M.; Li, P.; Wang, D. H.; Park, J. H. Water Splitting Progress in Tandem Devices: Moving Photolysis beyond Electrolysis. *Adv. Energy Mater.* **2016**, *6*, 1600602.

(94) Hardcastle, F. D.; Wachs, I. E.; Eckert, H.; Jefferson, D. A. Vanadium (V) Environments in Bismuth Vanadates: A Structural Investigation Using Raman Spectroscopy and Solid State ^{51}V NMR. *J. Solid State Chem.* **1991**, *90*, 194–210.

(95) Morgan, K.; Sayer, B. G.; Schrobilgen, G. J. Bismuth NMR Spectroscopy: ^{209}Bi and ^{19}F High-Resolution NMR Spectra of the Hexafluorobismuthate(V) Ion. *J. Magn. Reson.* **1983**, *52*, 139–142.

(96) Hamaed, H.; Laschuk, M. W.; Terskikh, V. V.; Schurko, R. W. Application of Solid-State ^{209}Bi NMR to the Structural Characterization of Bismuth-Containing Materials. *J. Am. Chem. Soc.* **2009**, *131*, 8271–8279.

(97) Frost, R. L.; Henry, D. A.; Weier, M. L.; Martens, W. Raman Spectroscopy of Three Polymorphs of $BiVO_4$: Clinobisvanite, Dreyerite and Pucherite, with Comparisons to $(VO_4)_3$-Bearing Minerals: Namibite, Pottsite and Schumacherite. *J. Raman Spectrosc.* **2006**, *37*, 722–732.

(98) Tate, M. L.; Blom, D. A.; Avdeev, M.; Brand, H. E. A.; McIntyre, G. J.; Vogt, T.; Evans, I. R. New Apatite-Type Oxide Ion Conductor, $Bi_2La_8[(GeO_4)_6]O_3$: Structure, Properties, and Direct Imaging of Low-Level Interstitial Oxygen Atoms Using Aberration-Corrected Scanning Transmission Electron Micr. *Adv. Funct. Mater.* **2017**, *27*, 1605625.

(99) Cooper, J. K.; Gul, S.; Toma, F. M.; Chen, L.; Glans, P.-A.; Guo, J.; Ager, J. W.; Yano, J.; Sharp, I. D. Electronic Structure of Monoclinic $BiVO_4$. *Chem. Mater.* **2014**, *4*, 5365–5373.

(100) Resasco, J.; Zhang, H.; Kornienko, N.; Becknell, N.; Lee, H.; Guo, J.; Briseno, A. L.; Yang, P. $TiO_2/BiVO_4$ Nanowire Heterostructure Photoanodes Based on Type II

Band Alignment. *ACS Cent. Sci.* **2016**, *2*, 80–88.

CHAPTER 2:
SURFACE FUNCTIONALIZED ATOMIC LAYER DEPOSITION OF BISMUTH VANADATE FOR SINGLE-PHASE SCHEELITE[6]

[6] Reproduced from Lamm, B.; Sarkar, A.; Stefik, M. *J. Mater. Chem. A.* **2017**, *5*, 6060-6069 with permission from The Royal Society of Chemistry.

Abstract

Monoclinic bismuth vanadate is one of the most promising oxide photoanodes for solar –assisted water splitting. To date, the atomic layer deposition of bismuth vanadates has relied on the catalytic codeposition of $BiPh_3$ with VTIP to produce vanadium-rich compounds that undergo spinodal decomposition to multiphase mixtures upon crystallization. A surface functionalization (SF) step of ROH/VTIP/H_2O was developed to inhibit V_2O_5 deposition for adjustable Bi:V stoichiometry. Ethanol, 2-propanol, and methanol were each found to inhibit V_2O_5 deposition, in order of increasing effect. Applying this SF step with ternary Bi-V-O depositions (ROH/VTIP/H_2O/$BiPh_3$/H_2O) enabled composition tuning. The use of methanol enabled 45.9:54.1 Bi:V atomic ratio as-deposited, and was crystallizable to phase-pure scheelite, depending on the thickness. The resulting films were applied towards photo-assisted water splitting with a hole-scavenging sulfite where films up to 60 nm thick were free from apparent charge transport limitations. The optoelectronic properties were markedly improved by a novel photoelectrochemical activation step.

Introduction

Solar photoelectrochemistry (PEC) is an attractive source for sustainable fuels such as hydrogen.[1] Bismuth vanadate was first demonstrated as a photocatalyst for water oxidation in 1998, with the monoclinic-scheelite phase (m-$BiVO_4$) showing the highest efficiency.[2,3] The m-$BiVO_4$ phase has a band gap of 2.4 eV,[3,4] a conduction band edge near 0 V vs the reversible hydrogen electrode (RHE)[5] and a valence band edge near 2.4 V vs RHE. Thus electrons in the conduction band have appropriate potential to support the hydrogen evolution reaction (0 V vs RHE) at the counter electrode with a small applied bias and holes in the valence band have ample potential to support the oxygen evolution reaction

(1.23 V vs RHE) at the semiconductor-electrolyte interface. Electrons and holes generated by photoabsorption are thus able to support photoassisted water splitting with a low onset potential (ca. 0.25 V vs RHE) for the photoanode. The performance of $BiVO_4$ photoanodes has progressed quickly with many recent advances.[4–9]

For solar-fuel applications, bismuth vanadate requires an optical thickness of ~700 nm for efficient light harvesting near the band edge (discussed in SI) that is much larger than the sum of the depletion width and the limiting carrier diffusion length.[5,10] Thus, many recent devices with record photocurrents used $BiVO_4$ thin films supported upon transparent, conductive scaffolds. Such "host-guest" or extremely thin absorber approaches have been largely successful at decoupling optical absorption from carrier transport.[11–13] Thus far, all $BiVO_4$ host-guest reports have utilized non-uniform depositions or used cathodic depositions that limited the use of hole blocking layers at the host-guest interface.[7,8,14,15] In contrast, atomic layer deposition (ALD) enables controlled growth onto arbitrary 3D porous scaffolds independent of substrate electronic properties, bringing distinct advantages to the development of efficient host-guest nanostructures. Such structures have been developed for optoelectronics including α-Fe_2O_3,[16,17,26–35,18–25] Cu_2O,[36–39] and other photoelectrodes.[40–42]

Thus far, all reports of ALD bismuth vanadates had >65 at%V, leading to spinodal decomposition into $BiVO_4$ with an additional V_2O_5 phase.[43] With conventional ALD, the amount of material deposited per cycle is fixed due to a self-limiting reaction of each precursor at surface saturation. The deposition rate is a constant for each precursor/oxidant combination under steady state.[44] While this is a significant benefit for conformal thin-film growth, the quantized nature of deposition limits stoichiometry tuning. Surface-

functionalized atomic layer deposition (SF-ALD) enables further stoichiometry tuning by modifying the amount of material deposited per cycle. SF-ALD can thus reduce the amount of material deposited by partially blocking deposition sites. For example, alcohols can undergo a condensation reaction with surface hydroxyl groups to inhibit the deposition of the subsequent metal precursor.[44–46] The subsequent oxidant pulse removes the remaining ligands from the metal as well as the SF-species. Since the SF step is self-limiting, the overall deposition remains conformal and self-limiting, but with more granular control over the amount deposited. Although SF-ALD was developed to modify the extent of doping,[44–46] it is also conceptually suitable for tuning the stoichiometry of multi-metal compounds.

Here, SF-ALD with alkyl alcohols (ROH) enables the most Bi-rich depositions of bismuth vanadate to date, including nearly stoichiometric $BiVO_4$. Crystallization of the amorphous films led to the phase-pure photoactive form of m-$BiVO_4$, depending on film thickness. In addition, a PEC activation treatment was found to significantly improve PEC efficiency.

Experimental

Materials

Triphenyl bismuth ($BiPh_3$, 99%) and vanadium(V) triisopropoxy oxide (VTIP, 98+%) were used as received from STREM. Deionized (DI) water was prepared using a Siemens Labostar model; where specified, deionized ultra-filtered (DIUF) water (Fisher) was used in place of DI water. Methanol (ACS Grade, Fisher), 2-propanol (70% lab grade, BDH), ethanol (95%, Fisher), H_3BO_3 (ACS Grade, VWR Life Science), HNO_3 (Fisher, Optima grade), Na_2SO_3 (ACS Grade, Macron), and KOH (ACS Grade, Fisher) were used as-received. TEC-15 fluorine-doped tin oxide coated glass (FTO) was purchased from Hartford Glass. The FTO substrates were cleaned extensively before use with 2-propanol

and DI water before sonication in soapy water (Decon Contrex, 2 wt%), followed by additional rinses with water and 2-propanol, followed by sonication in 2-propanol. Polished n-doped silicon wafers with (100) orientation were purchased from University Wafers, USA. The cleaned FTO substrates and silicon wafers were calcined using a Barnstead Thermolyne muffle furnace at 450 ^{o}C for 1 hr immediately prior to use. High-temperature grade Kapton tape was purchased from McMaster-Carr, USA. Ultra-high purity nitrogen (99.999%) and oxygen (99.5%) were used as received from Praxair.

Atomic Layer Deposition of Bismuth Vanadate Films

Samples were masked using Kapton tape to define the deposition region. Samples for composition analysis were masked on the bottom to avoid diffusion gradients along the back of the films. Samples on FTO were masked on the back and partially on the front to provide clean electrical contacts for PEC measurements. The $BiPh_3$ and VTIP were each loaded into separate stainless-steel cylinders in an argon glovebox. Water and the alcohol in use (ROH; ethanol, 2-propanol, or methanol) were loaded into separate stainless steel cylinders under normal atmosphere. The cylinders were sealed and connected to and Arradiance Gemstar-8 reactor. Nitrogen was used as both the carrier gas and the purging gas. Precursor dosing was controlled using Swagelok ALD valves. The $BiPh_3$ and VTIP cylinders were heated to 130 and 45 ^{o}C, respectively. The reactor was set to 130 ^{o}C, both metal precursors had a pulse time of 2 s, ROH had a pulse time of 25 ms, and water had a pulse time of 25 ms. A vapor-boosting 20 ms pulse of nitrogen was added to the $BiPh_3$ cylinder just prior to each pulse. The reactor chamber was isolated before each pulse to contain the precursors for 1 s after exposure ("exposure mode"). The excess precursors were purged after each exposure using 200 sccm nitrogen for 10 s. The deposition was organized into a macrocycle of $(ROH/VTIP/water/BiPh_3/water)_a$ where ROH was used to

control composition and 'a' controlled total thickness deposited. A comprehensive ALD protocol is provided in the Supporting Information (Table B.2).

SF-ALD sample PEC performance was compared to the performance of previously reported samples synthesized via conventional ALD (Figure B.4).[43] The reported ALD procedure is identical to the SF-ALD procedure described above, sans alcohol surface functionalization. Conventional ALD samples (**ALD**) of 55.6 nm thickness were calcined at 450 ^{o}C for 1 h and etched in 1 M NaOH to remove excess V_2O_5. SF-ALD samples (**60nm-8k**, described in the text) were measured following the standard activation treatment, *vide infra*.

In Situ Deposition Monitoring

Quartz crystal microbalances (QCMs) assembled in an array were used to monitor ALD depositions in situ across the reaction chamber. It is important to note that while data were collected in real time, certain variables – such as precursor pulsing, varying flow rates, and proportional-integral-derivative (PID) controller cycles – caused thermal transients that obfuscated the very small signals for mass change during individual pulses. Accordingly, average deposition rates were determined using a least squares fit analysis for linear deposition rates. A total of 500-2000 (SF)-ALD cycles were performed for each experiment to provide accurate measurements of growth per cycle (GPC). The QCM crystals were installed in a low-profile plate inside the deposition chamber and electrical connections were fed through an auxiliary port. The QCM array (custom design, Colnatec) utilized a special sealing interface to eliminate the need for inert gas purging on the back side of the crystals. Radiation-compensated (RC) cut quartz crystals were used with aluminum contacts (Colnatec). The native oxide on the Al top contact of the crystals led to the facile

establishment of linear QCM response, as shown elsewhere.[43] QCM deposition data were calibrated by SEM observations of film thickness.

Composition Analysis

Samples were digested with 4 M nitric acid (~5 mL) in Teflon vessels at 180 ^{o}C for 5 hr. The resulting solution was diluted to 50 mL using DI water. A Finnigan ELEMENT XR double-focusing magnetic sector field-inductively coupled plasma-mass spectrometer (SF-ICP-MS) was used for analyzing V (51, LR), Bi (209, LR), and internal standard Rh (103 LR). A Micromist U-series nebulizer (GE, Australia) was operated at 0.2 mL min^{-1} with a quartz torch and an injector (Thermo Fisher Scientific, USA) for sample introduction. The gas flow was set to 1.08 mL min^{-1}. The forwarding power was 1250 W. Composition analysis was based on a five-point calibration curve for both V and Bi. The calibration range was from 10 to 600 ppb. The R^2 values for the initial calibration curves were greater than 0.999.

Film Treatments

The ALD films were heated to induce crystallization. Samples were heated at 5 ^{o}C/min to 200 ^{o}C, followed by 10 ^{o}C/min to 450 ^{o}C, held constant at 450 ^{o}C for 1 hr, and allowed to cool in the furnace.

Diffraction

X-ray diffraction experiments were conducted using a SAXSLab Ganesha at the South Carolina SAXS Collaborative. A Xenocs GeniX 3D microfocus source was used with a Cu target to generate a monochromatic beam with a 0.154 nm wavelength. The instrument was calibrated using silicon powder (NIST 640e). Scattering data were processed from the scattering vector $q = 4\pi\lambda^{-1}\sin\theta$ where λ is the X-ray wavelength and 2θ is the total scattering angle. A Pilatus 300 K detector (Dectris) was used to collect the two-dimensional (2D) scattering patterns. Samples were measured at an incident angle of 8^{o} relative to the film

plane. SAXSGUI software was used to radially integrate the 2D patterns to reduced 1D profiles. The conversion of the resulting intensity versus q data was converted to 2θ using the above formula.

Photoelectrochemical and Electrochemical Measurements

Linear sweep voltammograms were measured using a three-electrode potentiostat (BioLogic SP-150) with a Ag/AgCl/KCl (saturated) reference electrode (Pine Instruments) and a platinum wire counter electrode (Pine Instruments). Samples on FTO substrates were clamped with a titanium sheet to provide an ohmic contact. The electrodes were placed into a cell made of polyether ether ketone (PEEK) with a fused-silica window. Simulated sunlight was generated using a 75 W xenon lamp (OBB, Horiba) that passed through a water infrared filter (OBB, Horiba), a KG-3 filter (317-710 nm pass, Edmund Optics), and a BG-40 filter with an antireflective coating (335-610 nm pass, Thorlabs). This combination of filters removed much of the UV light where the Xe lamp has the most spectral mismatch from the AM 1.5 spectrum. The transmitted light was collimated using a fused-silica lens (Thorlabs) and passed through an engineered diffuser with a top-hot profile to provide a homogeneous intensity profile with a slight 10^{o} divergence. The transmitted light was corrected for brightness in the 335-610 nm spectral range to generate a photocurrent identical to AM 1.5 sunlight. The illumination intensity was measured using a calibrated UV-enhanced silicon photodiode (Thorlabs) equipped with a neutral reflective filter (optical density 1.0, Thorlabs) to maintain a linear and calibrated photodiode response. This calibration practice provides accurate solar simulation in terms of both spectral distribution and brightness with a minimal correction factor.[47]

PEC measurements were performed in 1 M potassium borate with or without 0.2 M sodium sulfite (Na_2SO_3) as hole scavenger at pH 9.35. It has been well established that

potassium phosphate buffers dissolve $BiVO_4$ at working pH values;[9,48,49] however, $BiVO_4$ photoanodes are stable in alkaline borate buffers. The potassium borate solution was prepared by adjusting the pH of 1 M H_3BO_3 in DIUF water to 9.35 ± 0.02 with KOH as confirmed by a calibrated Thermo Scientific OrionStar A211 pH meter. The sulfite acted as a hole scavenger to provide quantitative charge injection from the semiconductor to the electrolyte for the measurement of film performance without catalysts. The samples were scanned from -0.600 to 0.650 V vs Ag/AgCl reference electrode at 10 mV s^{-1}. Multiple scans were completed at each condition to confirm reproducibility and the second scan results were reported. Film stability was measured by chronoamperometry (CA) at 0.6 V vs RHE under simulated AM 1.5 illumination to measure the photocurrent stability of SF ALD **30nm-4k** film over 17 hrs. The film was freshly calcined prior to the stability measurement.

Quantum efficiencies were calculated based on CA measurements made with monochromatic light while using the same potassium borate buffer described above. Illumination was generated using a 150 W xenon lamp (OBB, Horiba) that passed through an 180° monochromator with a 5 mm slit width and 1200 grates mm^{-1} diffraction grating (OBB, Horiba). Transmitted light was collimated using a fused-silica lens (Thorlabs) and passed through an engineered diffusor with a top-hat profile to provide a homogenous intensity profile with a slight 10° divergence. CA measurements were recorded at -0.153 V vs Ag/AgCl reference unless otherwise noted. All electrochemical potentials E were reported versus the reversible hydrogen electrode (RHE) using the formula E(vs RHE) = E(vs Ag/AgCl)+E_{ref}(Ag/AgCl)+0.059 V * pH where E_{ref} = 0.197 V in this case.

For both CA and LSV measurements, representative samples of a given set were plotted with the mean (indicated as 'x') and bars for the error of the mean.

Prior to LSV and CA measurements, films were exposed to an external bias of 0.6 V vs RHE (-0.153 V vs Ag/AgCl) under AM 1.5 illumination for 1 hour. To compare different aspects of film activation (Figure 2.8), freshly calcined samples were measured for UV-vis absorptance and CA data (**Control**). Following this, these same samples were either allowed to soak in potassium borate solution for 1 hr (**Soak**), applied 0.6 V vs RHE for 1 hr in dark (**EC-Only**), exposed to AM 1.5 solar simulator for 1 hr (**Photo-Only**), or treated with the standard PEC activation treatment (**PEC**) before measuring LSV and CA once more (except in the case of **Soak**, where only CA was measured). Additionally, another set of freshly calcined samples were soaked in electrolyte for 1 hr followed by LSV and CA (**LSV-Only**, Figure B.4) to observe the effects of LSV measurement, which is a combination of phot- and electrochemical treatments. It is important to note that for this series of measurements, samples all came from the same 4,000-cycle SF-ALD film; additionally, for each test condition samples were selected from a variety of locations within the film to avoid local thickness or crystal quality variance within the film.

Optoelectronic Properties

The optical response of thin films was measured using a Shimadzu UV-2450. A sandwich configuration of FTO-water-fused quartz was used to minimize light scattering differences between the blank measurement of bare FTO and samples coated onto FTO. Identical measurements on FTO were used to establish the baseline for the measurement of the optical properties of the deposited films alone.

X-ray Photoelectron Spectroscopy

A Kratos Axis UltraDLD instrument equipped with a monochromated copper K-α X-ray source (wavelength of 0.154056 nm-1, operating at 10 kV and 15 mA). A hybrid lens mode was employed during analysis, with an analysis area of approximately 700 μm x 300 μm. The XPS spectra for all samples were taken at a photoemission angle of 0°, relative to the surface normal. A Kratos charge neutralizer system was used on all samples with a filament current of between 1.8 - 2.1 A and a charge balance of 3.6 V.

Morphology

A Zeiss Ultra Plus scanning electron microscope (SEM) was operated at 5 kV using an in-lens secondary electron detector to observe the film surface and cross-sectional acquisition. ALD growth rates were calculated based upon cross-sectional SEM imaging of films in the 50-100 nm thickness range.

Results and Discussion

Effect of Alcohol on Surface Functionalization

The ALD growth of bismuth vanadates (BVO) has not yet enabled phase pure scheelite due to limited stoichiometry control. We briefly note that bismuth vanadates are a class of compounds with various Bi:V ratios. The prior report of ALD BVO utilized triphenyl bismuth ($BiPh_3$), vanadium triisopropoxy oxide (VTIP), and water. To the best of our knowledge, this remains the only prior reported ALD of BVO. Here, the film stoichiometry was >65 at%V-rich and required a post-treatment etch of V_2O_5 to achieve phase-pure m-$BiVO_4$ films.[43] Increasing the pulse ratio to favor Bi had limited benefits since the Bi-deposition is catalytically dependent on V-OH species.[43] SF-ALD provides a novel and time-efficient alternative to improve the Bi:V stoichiometry by reducing the amount of VTIP deposited in each cycle. Starting from a prior ALD protocol for V_2O_5,[43,50] a pulse of different alcohols were used to inhibit the subsequent VTIP deposition with a [ROH-VTIP-

W]$_x$ deposition cycle. The specific alcohols investigated included ethanol, 2-propanol, and methanol (EtOH, iPrOH, and MeOH, respectively). Starting from a V_2O_5 growth-per cycle (GPC) of 0.22 Å/cycle, the alcohols were found to have increasing inhibition effect in order of EtOH, iPrOH, and MeOH (Figure 2.1 and Table 2.1). The alcohol pulse length was found to saturate growth inhibition well within 25 ms (Figure B.1). MeOH had the largest effect on VTIP deposition with the lowest GPC. This deviates from prior reported SF-ALD trends with these alcohols applied towards other materials.[44,45] Many aspects determine the efficacy of a particular SF-species, including the density and type of remaining active sites, side reactions between precursor and inhibitor, and inhibitor displacement by precursor.[45]

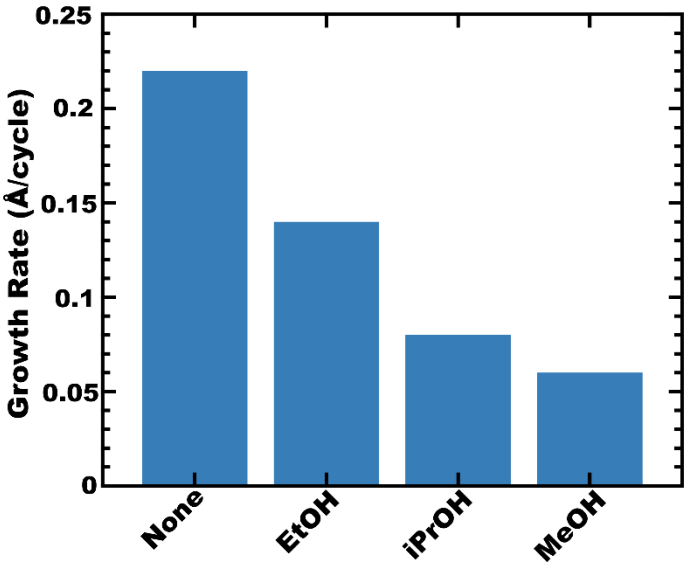

Figure 2.1 (SF)-ALD growth rates of V_2O_5 using different alcohols for surface functionalization with deposition cycles of [ROH-VTIP-W]$_x$. Sample 'none' corresponds to normal ALD with a deposition cycle of [VTIP-W]$_x$; the remaining samples refer to ROH in the SF-ALD deposition cycle of [ROH-VTIP-W]$_x$.

Table 2.1 Growth rates of V_2O_5 with different alcohols used for surface functionalization.

Sample Name	Deposition Cycle	Growth Rate (Å/cyc)
ALD-V_2O_5	$[VTIP\text{-}W]_x$	0.22
EtOH-V_2O_5	$[EtOH\text{-}VTIP\text{-}W]_x$	0.14
iPrOH-V_2O_5	$[iPrOH\text{-}VTIP\text{-}W]_x$	0.08
MeOH-V_2O_5	$[MeOH\text{-}VTIP\text{-}W]_x$	0.06

The SF-ALD of BVO was examined with the same series of alcohols examined above. The SF-ALD deposition sequence was $[ROH\text{-}VTIP\text{-}W\text{-}BiPh_3\text{-}W]_x$. The use of EtOH, iPrOH, and MeOH for SF-ALD were found to result in increasingly Bi-rich depositions (Figure 2.2 and Table 2.2), following a consistent trend with GPC for SF-ALD of V_2O_5. The samples prepared using MeOH had stoichiometries closest to the 1:1 $BiVO_4$ compound, with 45.9 at%Bi and 54.1 at%V determined by mass-spectrometry (MS). For the remainder of this paper we thus focus exclusively on ternary BVO produced by SF-ALD with MeOH (MeOH-BVO). Cross-sectional SEM confirmed conformal deposition on both Si and FTO substrates (Figure 2.3a-d). Measurements from the flat Si substrate were used to determine the growth rate of 7.5 nm for every 1,000 cycles of SF-ALD. This corresponds to a GPC of 0.075 Å/cycle that is remarkably quite similar to 0.07 Å/cycle from conventional ALD.[43] The combination of a similar GPC with enhanced Bi content suggests that the SF step not only inhibits VTIP deposition, but also that the resulting surface, after hydrolysis, enhances the following $BiPh_3$ deposition. Such mechanistic changes could be attributed to a combination of steric effects with the spatial distribution of active V-OH surface sites for $BiPh_3$ catalytic deposition.

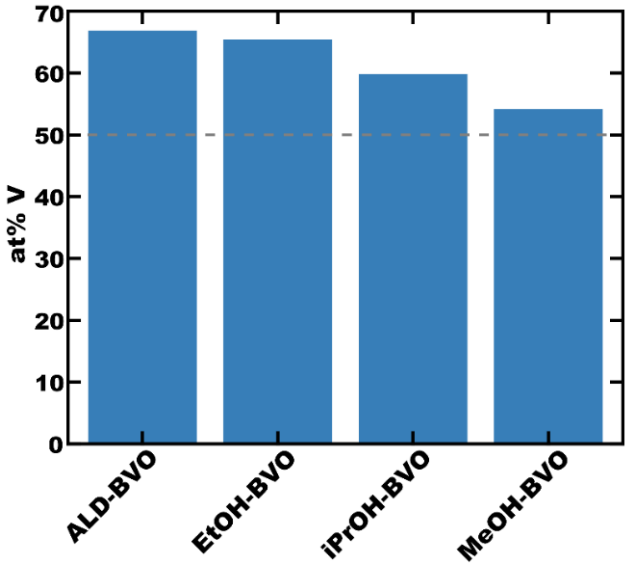

Figure 2.2 Compositions for (SF)-ALD of BiVxOy prepared with different alcohols for surface functionalization using deposition cycles of [ROH-VTIP-W-BiPh3-W]x.

Table 2.2 Composition of (SF)-ALD BVO films with different alcohols used for surface functionalization.

Sample Name	Deposition Cycle	at%Bi	at%V
ALD-BVO	$[VTIP\text{-}W\text{-}BiPh_3\text{-}W]_x$	33.2%	66.8%
EtOH-BVO	$[EtOH\text{-}VTIP\text{-}W\text{-}BiPh_3\text{-}W]_x$	34.6%	65.4%
iPrOH-BVO	$[iPrOH\text{-}VTIP\text{-}W\text{-}BiPh_3\text{-}W]_x$	40.2%	59.8%
MeOH-BVO	$[MeOH\text{-}VTIP\text{-}W\text{-}BiPh_3\text{-}W]_x$	45.9%	54.1%

The crystallization of MeOH-BVO films was examined by grazing incidence wide-angle X-ray scattering (GI-WAXS) and SEM after high temperature calcination. The as-deposited films were amorphous, similar to the prior reported bismuth vanadate films by conventional ALD (Figure 2.3).[43] After heating to 450 ^{o}C for 1 hr the MeOH-BVO films exhibited strong reflections consistent with nearly phase-pure m-$BiVO_4$. In contrast, the ALD-BVO sample exhibited a pattern consistent with a mixture of m-$BiVO_4$, tetragonal bismuth vanadate (t-$BiVO_4$), and orthorhombic vanadium oxide (o-V_2O_5), consistent with the significant excess of vanadium detected by MS. The MS data also indicated a 4.1 at%V

excess for the MeOH-BVO samples. This slight excess of vanadium did not result in an observable V_2O_5 phase for films ≤30 nm (Figure B.2). Additional GI-WAXS data for MeOH-BVO films on FTO substrates matched that of films on Si, albeit with additional substrate peaks (Figure B.3). Film calcination also resulted in minor morphology changes from crystallite formation. Films calcined on FTO substrates remained fairly uniform whereas films on Si substrates underwent dewetting (Figure 2.4e,f). MeOH-BVO samples enabled the crystallization of phase-pure and nearly stoichiometric m-$BiVO_4$.

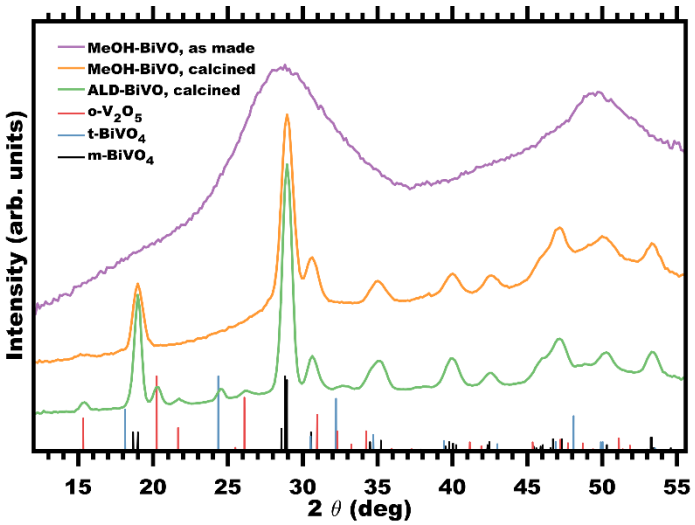

Figure 2.3 GI-WAXS of MeOH-BVO films, both as-made and calcined. For comparison, a calcined film from ALD-BVO is presented. All samples had x=4,000 deposition cycles. Graphs were offset vertically for clarity and fit data correspond to PDF#14-0688, 83-1812, and 89-0611, respectively. The calcination step was to 450 ^oC at 10 ^oC/min with a 60 min hold.

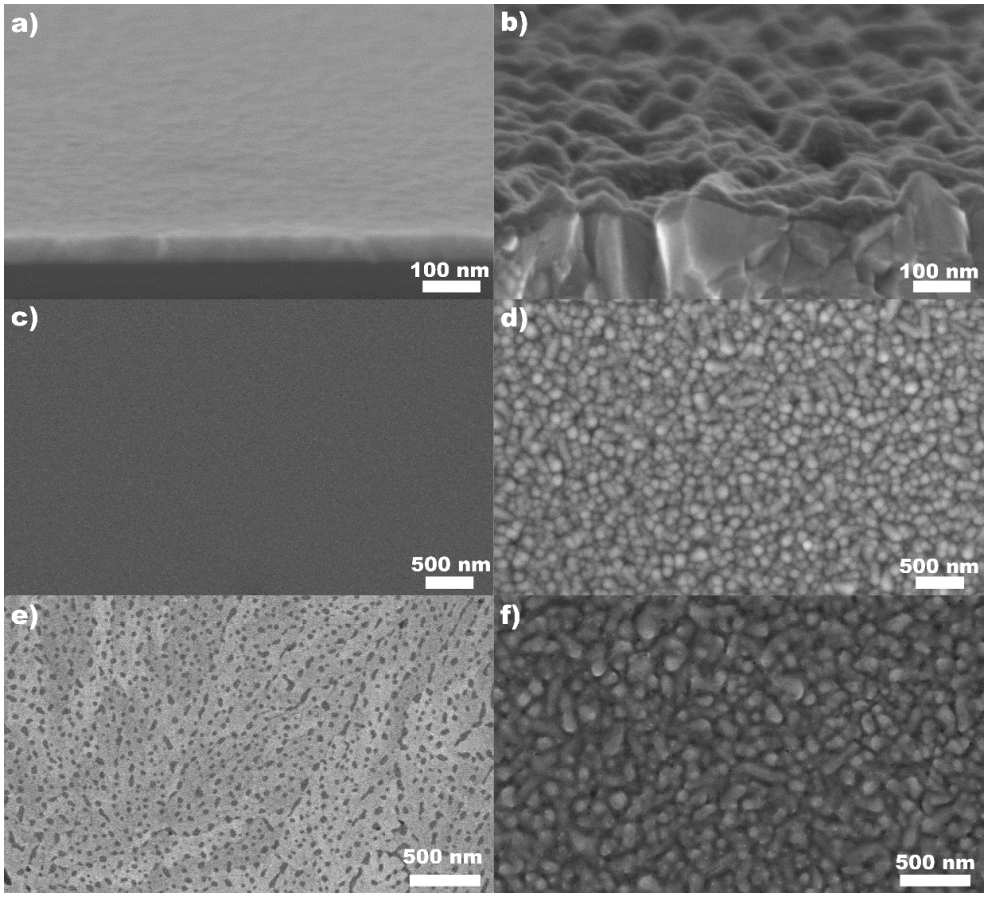

Figure 2.4 SEM of bismuth vanadates prepared by MeOH-BVO on Si (a,c,e) and FTO substrates (b,d,f). As-made films are shown in cross-section (top row, a,b) and top view (middle row, c,d). Crystallized films heated to 450 °C are shown in top view (bottom row, e,f). The deposition cycle was [MeOH-VTIP-W-$BiPh_3$-W]$_x$ where x was either 3,000 (b,e,f) or 6,000 (a,c,d).

PEC Performance vs Thickness

The calcined MeOH-BVO films were applied towards solar-assisted PEC water splitting with thickness ranging from 7.5 to 75 nm. With a GPC of 0.075 Å/cycle, this corresponds to samples made using 1,000-10,000 SF-ALD cycles. Here, the thickest samples examined were commensurate to the reported electron diffusion length of ca. 70-75 nm in $BiVO_4$.[5,8,51,52] The PEC performance is a product of several terms, including the light harvesting efficiency (LHE), the charge separation efficiency, and the charge injection efficiency (Equation 2.1), where J_{PEC} is the measured photocurrent density, J_{abs} is the

photon absorption rate expressed as current density (determined from LHE), φ_{sep} is the carrier separation efficiency, and φ_{inj} is the charge injection efficiency.[5,53–55]

$$J_{PEC}=J_{abs}\times\phi_{sep}\times\phi_{inj} \quad (2.1)$$

Here, the PEC performance was measured in the presence of a hole-scavenging sulfite electrolyte to pin the charge injection efficiency at 100% (φ_{inj} = 1). Thus, the measured photocurrents represent the voltage dependent product of light harvesting efficiency and charge separation efficiency. For this sample series, the photocurrent monotonically increased with sample thickness (Table 2.3 and Figure 2.5), corresponding to the expected trend in light harvesting efficiency, as confirmed by UV-vis measurements (Figure 2.6a). The highest photocurrent was measured with sample **75nm-10k** with 0.69 and 1.21 mA/cm^2 at 0.60 and 1.23 V vs RHE, respectively. For thicknesses from 15-60 nm the photocurrent performance monotonically increases with one exception, *vide infra*, and notably all exhibited performance that was independent of the illumination direction. In contrast, after 60 nm of thickness there is a statistically significant difference where backside illumination results in more photocurrent than front side illumination. Since m-$BiVO_4$ has a lower electron diffusion length (majority carrier) than hole diffusion length (minority carrier), one expects better performance when carriers are generated closer to the electron-accepting FTO contact. This observation shows the transition to transport limited performance occurs between 60 and 75 nm, similar to prior estimations.[5,10] The thinnest 7.5 nm film produced negligible photocurrent presumably due to poor crystallization (Figure B.2a) or excessive recombination due to the FTO proximity.[30,56,57] Such a "dead layer" effect has been noted before for PEC thin films, including Fe_2O_3 and $BiVO_4$.[22,30,55–58] In contrast to prior reports, however, MeOH-BVO yields photoactive films when >15

nm whereas a different synthesis route required >50 nm.[55] A notable curiosity was the similar photocurrent response from both **30nm-4k** and **45nm-6k**. This exception to the trend discussed above was confirmed with multiple sample measurements produced from multiple SF-ALD depositions. There is a change in the GI-WAXS patterns between these two samples where a second phase of o-V_2O_5 is apparent in >30 nm film (Figure B.2b). This suggests a threshold thickness for accommodation of the excess 4.1 at%V as amorphous V_2O_5 or within the m-$BiVO_4$ lattice. At this transition, the second phase and the associated interfaces lowered the charge separation efficiency to a similar extent as the increase in the light harvesting efficiency, resulting in comparable performance. From these results, it is concluded that MeOH-BVO films <75 nm are viable thin films for host-guest applications.

Table 2.3 A series of films with different thicknesses were prepared using the MeOH-BVO protocol. All samples were calcined after growth via the deposition cycle of [MeOH-VTIP-W-$BiPh_3$-W]$_x$ with varying values for x.

Sample Name	**Film Thickness (nm)***	**X, number of deposition cycles (k cycles)**	**Photocurrent** at 0.6 V vs RHE**	**Photocurrent** at 1.23 V vs RHE**
7.5nm-1k	7.5	1	0.098±0.002	0.035±0.005
15nm-2k	15	2	0.08±0.01	0.22±0.01
22.5nm-3k	22.5	3	0.14±0.02	0.34±0.05
30nm-4k	30	4	0.35±0.02	0.70±0.02
45nm-6k	45	6	0.30±0.02	0.67±0.03
60nm-8k	60	8	0.42±0.03	0.81±0.03
75nm-10k	75	10	0.69±0.04	1.21±0.04
*Film thickness calculated from the product of the growth-per-cycle with the number of cycles (GPC*x) **Mean back-side photocurrent (mA/cm^2)				

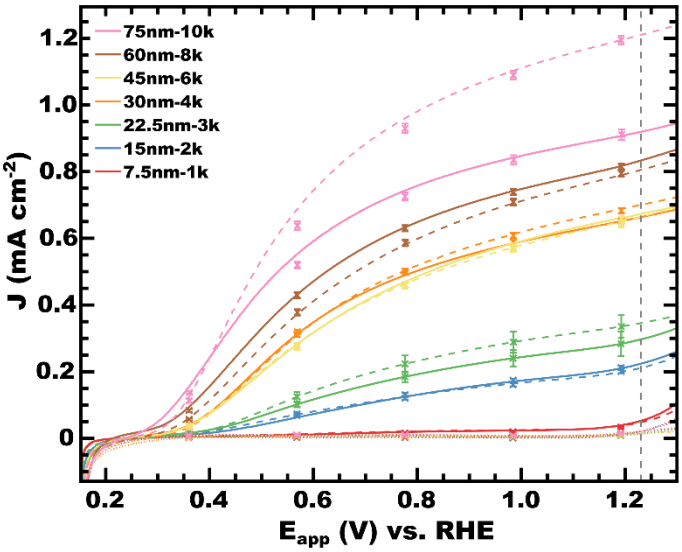

Figure 2.5 Photocurrent response for calcined MeOH-BVO films of as a function of film thickness and applied potential. The electrolyte was 1.0 M potassium borate with a pH of 9.36 with 0.2 M Na_2SO_3 as hole scavenger. The dark current (dotted), photocurrent with backside illumination (dashed) and photocurrent with front side illumination (solid) are presented. The film thickness is specified in the legend followed by the corresponding number of MeOH-BVO deposition cycles x.

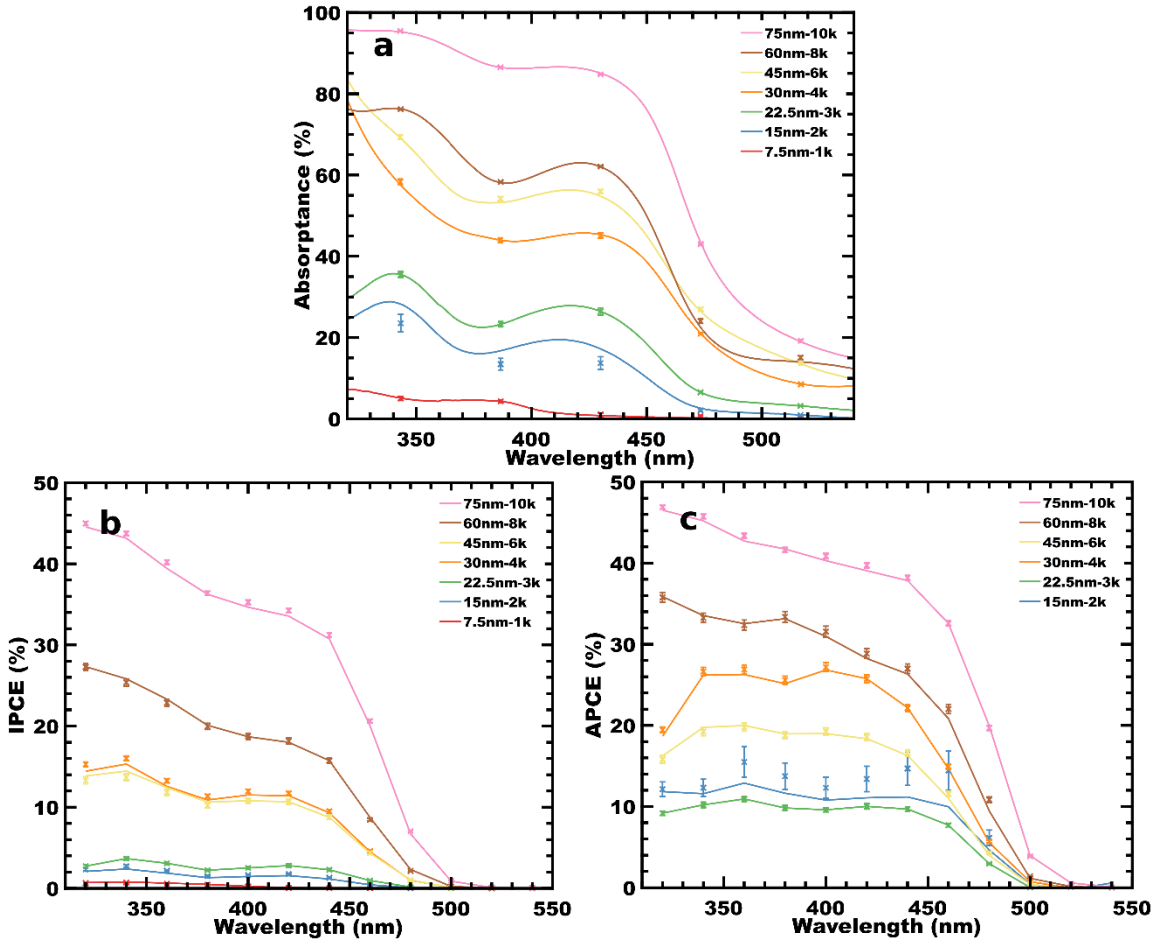

Figure 2.6 The (a) absorptance, (b) incident photon-to-current efficiency and (c) absorbed photon-to-current efficiency are shown for calcined MeOH-BVO films of various thicknesses. The IPCE and APCE were measured 0.6 V vs RHE in 1.0 M potassium borate with 0.2 M Na_2SO_3 as hole scavenger. The film thickness is specified in the legend followed by the corresponding number of MeOH-BVO deposition cycles, x.

Further PEC insights were gained by examining the wavelength dependent incident photon-to-current efficiency (IPCE, Figure 2.6b) and the absorbed photon-to-current efficiency (APCE, Figure 2.6c). As expected, IPCE increases with thickness, albeit with the same performance overlap observed in the J-V data and discussed above. This is consistent with the expectation of improved LHE with thicker films. The APCE was calculated by normalizing the IPCE with the LHE, resulting in the wavelength dependent φ_{sep} for each sample. The monotonic trend of higher APCE with thicker films was attributed

to lower recombination rates in thicker films (due to the distance from the FTO/$BiVO_4$ interface). This observation suggests the future development of hole-blocking layers to mitigate recombination at the FTO interface.

To confirm the validity of these measurements, the photocurrent at 0.6 V vs RHE ($J_{J\text{-}V}$) was compared to the integrated product of IPCE with the AM 1.5 spectrum (J_{IPCE}, Table B.1). The photocurrents were matched within 15% for sample **75nm-10k**. However, it was apparent that thinner films exhibited a greater difference that was attributed to the varying intensity between the simulated AM 1.5 spectrum used for J-V and the monochromator used IPCE measurements. Previous reports indicated a significant dependence of m-$BiVO_4$ quantum efficiencies with illumination intensity.[10,51]

The PEC performance of SF-ALD $BiVO_4$ electrodes were compared to $BiVO_4$-V_2O_5 electrodes prepared by conventional ALD that were subsequently etched yield a porous film of phase-pure scheelite.[46] Please note that conventional ALD routes do not yet exist for phase pure $BiVO_4$ without subsequent etching. Comparing films of similar thickness, these two synthesis methods result in similar plateau photocurrents with the SF-ALD BiVO4 exhibiting an improved onset potential 120 mV lower (Figure B.4). The photocurrent stability of SF-ALD $BiVO_4$ films was examined under continuous illumination for 17 hrs (Figure B.5). After the initial PEC activation (t = 1 h), the photocurrent decreased by 11% over this period.

The SF-ALD $BiVO_4$ films presented here are promising for application towards host-guest composites. Prior works have demonstrated mesoporous films with photocurrents over 3 mA/cm^2 at potentials as low as 0.6 V vs RHE.[5,9] In the past year, photocurrents at the thermodynamic water splitting potential of 1.23 V vs RHE of ≥5 mA/cm^2 have been

reported with host-guest composites.[8,9] These prior works used cathodic electrodeposition to produce $BiVO_4$ films and thus are not ideally suited for elaboration with hole blocking materials at the FTO-$BiVO_4$ interface. In contrast, the SF-ALD route presented here is compatible with arbitrary substrates, independent of their electronic properties. We anticipate that future studies with the SF-ALD of $BiVO_4$ onto high surface area conductive substrates (such as nanostructured $Sb:SnO_2$)[59] will lead to improvements in overall performance.

Effects of PEC Activation Treatment

A pronounced effect of PEC measurement time was noted for the performance of the above-discussed films. In all cases, the photocurrent continuously increased with measurement time until a plateau. Improvements as large as 380% were found in some cases. We thus developed a PEC activation treatment to quickly stabilize film performance before the above measurements were performed. Recent reports with other fabrication routes have also indicated that various pretreatments improve PEC performance. Pretreatments have been reported using controlled reduction and/or oxidation of V cations,[9,60] ultraviolet light,[61] and open-circuit exposure to AM 1.5 illumination.[62] It was suggested that the elimination of surface oxygen by producing oxygen vacancies is the source of improved PEC performance.[9,60–64]

A PEC activation treatment was developed to establish stable photocurrents before performance measurements (described in Experimental). The improved IPCE after PEC activation treatment was surprising since the films had uniformly reduced optical absorption (Figure 2.7a). The extent of change in performance was found to vary with film thickness. For 30 nm films the IPCE and APCE increased by 2.6x and 3.1x with the PEC activation treatment. For 60 nm films the IPCE and APCE increased by 3.8x and 4.1x with

the PEC activation treatment (Table 2.4 and Figure 2.7). We note that GI-WAXS of calcined MeOH-BVO films presented above indicated a change from single-phase m-$BiVO_4$ for ≤30 nm thick films to a mixture of m-$BiVO_4$ and o-V_2O_5 for ≥45 nm thick films (Figure B.2). These thicker films with crystalline o-V_2O_5 exhibited the most change during PEC activation treatment, suggesting a dependence on the nature of the slight V-excess with MeOH-BVO deposition.

Table 2.4 The effectiveness of sample activation pretreatment varied with film thickness. All samples were calcined after growth from the same MeOH-BVO deposition cycle: [MeOH-VTIP-W-BiPh3-W]x where x was either 4k or 8k corresponding respectively to the 30 and 60 nm films.

Sample Name	Treatment	Film Thickness
30nm	None. Used directly following calcination	30 nm
30nm-Activated	1hr at 0.6 V vs RHE with AM 1.5 illumination	30 nm
60nm	None. Used directly following calcination	60 nm
60nm-Activated	1 hr at 0.6 V vs RHE with AM 1.5 illumination	60 nm

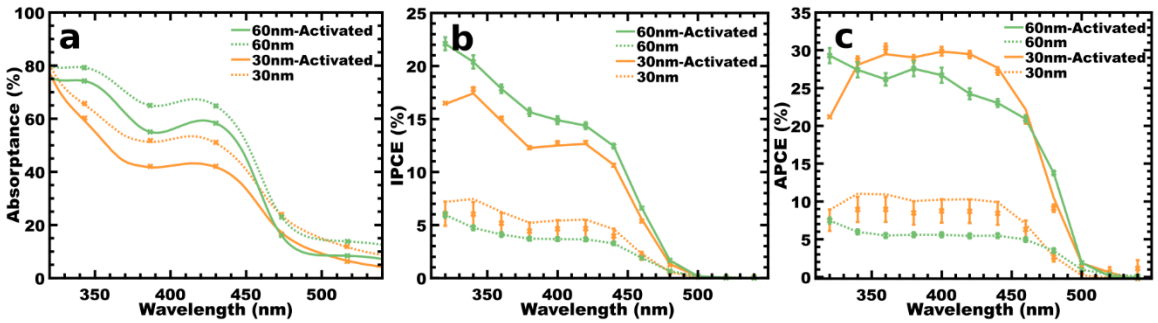

Figure 2.7 The effect of PEC activation treatment on (a) absorptance, (b) IPCE, and (c) APCE varied with film thickness. IPCE and APCE were measured at 0.6 V vs RHE in 1.0 M potassium borate with 0.2 M Na_2SO_3 as hole scavenger.

To evaluate the efficacy of this multicomponent PEC activation treatment, multiple control experiments were run to isolate the effects of each component of the treatment. Measurements were performed on photo-only treated (**Photo-Only**), electrochemical-only (**EC-Only**) treated, and electrolyte-only (**Soak**) treatments (Table 2.5, see Experimental for details). As seen in Figure 2.8b and c, each aspect of the PEC activation treatment

improves both the IPCE and APCE performance of the films to some degree. The largest effect was found for the complete treatment (**Activated**). All treatment conditions, except **Soak**, reduced the absorptance of the films (Figure 2.8a). Thus the improvement with Soak may be attributed to surface changes such as the hydrolytic formation of hydroxyl groups and is not consistent with dissolution nor significant internal changes to oxidation states. In contrast, all other components of the PEC activation treatment (**Photo-Only** and **EC-Only**) resulted in a concomitant reduction of absorptance with the improved performance. Previous reports have indicated that the V oxidation state in $BiVO_4$ plays an important role with some hints of an optimal V^{+4}/V^{+5} ratio.[9,60,62] It was also demonstrated that AM 1.5 illumination under open circuit can markedly improve some films where it was suggested that removing surface states assisted to unpin the Fermi level.[62,65] Fermi level pinning from surface states has been identified in other photoanode materials, including Fe_2O_3 and TiO_2.[66,67] However, the changes in absorptance observed with **Photo-Only**, **EC-Only**, and **Activated** are consistent with additional bulk redox changes within the films.

Table 2.5 The effect of each component of the PEC activation were investigated separately. All samples are calcined MeOH-BVO films prepared with $[MeOH\text{-}VTIP\text{-}W\text{-}BiPh_3\text{-}W]_{4,000}$ resulting in a thickness of 30 nm.

Sample Name	Treatment
Control	None
Soak	Soaked in electrolyte for 1 hr (open circuit, no illumination)
EC-Only	Applied 0.6 V vs RHE for 1 hr (no illumination)
Photo-Only	AM 1.5 illumination for 1 hr (open circuit)
Activated	Applied 0.6 V vs RHE during AM 1.5 illumination for 1 hr

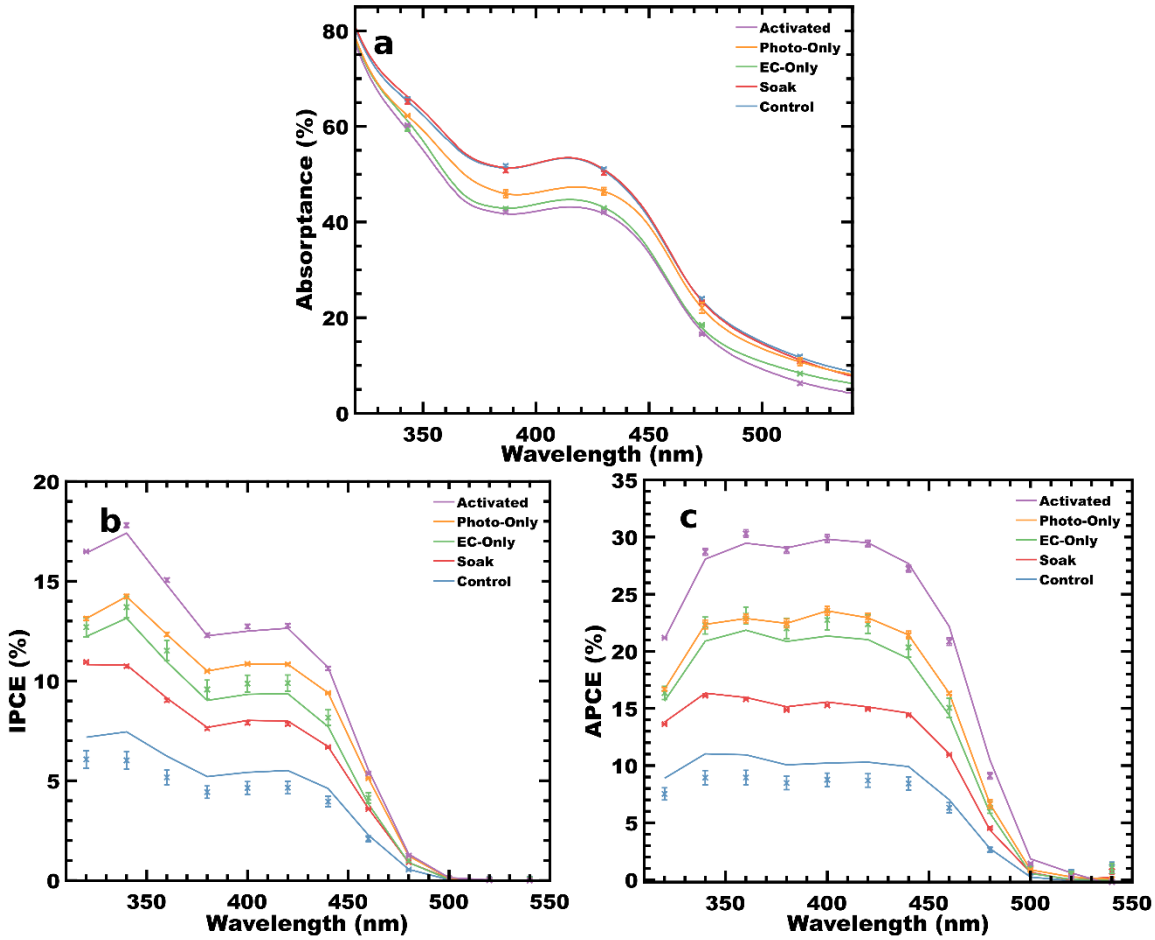

Figure 2.8 The absorptance, IPCE, and APCE varied with different components of the PEC activation treatment. IPCE and APCE were measured at 0.6 V vs RHE in 1.0 M potassium borate with 0.2 M Na_2SO_3 as hole scavenger.

X-ray photoelectron spectroscopy (XPS) was performed on 30nm-4k samples promptly after calcination as well as after the PEC activation treatment (Figure B.6; **Calcined** and **PEC Activated**, respectively). Changes to both the Bi and V oxidation states were detected at the sample surface as a result of the PEC activation treatment. Following calcination, films contained a minor component of reduced Bi^0 and V^{4+} in addition to the expected $BiVO_4$ states. The PEC activation treatment was found to fully oxidize these reduced states to Bi^{3+} and V^{5+}. This oxidation process is consistent with the observed oxidation current during PEC activation (Figure B.5). The ALD of bismuth titanates with $Bi(Ph)_3$ and water

was previously reported to result in a mixture of Bi^{3+} and Bi^{0}.[68] A recent also identified switchable oxidation states of $V^{4+/5+}$ during electrochemical cycling below 0.5 V vs RHE.[9] In contrast, a recently reported open-circuit illumination pretreatment identified the reduction of V from the +5 to the +4 state with a corresponding increase in performance.[62] These results highlight the connection of synthetic route and defect chemistries that can enhance the performance of $BiVO_4$ photoanodes.

Neither crystallographic nor surface morphology changes were observed for any of the treatments (Figures B.7 and B.8). While mechanistically intriguing, the detailed study of PEC activation is outside the scope of this SF-ALD study. The developed PEC activation treatment resulted in a marked improvement of MeOH-BVO film performance.

Conclusion

The uniform deposition of thin film m-$BiVO_4$ onto arbitrary hosts is necessary for the development of next-generation host-guest architectures for solar water splitting. The capability to deposit $BiVO_4$ by ALD enables the further development independent of substrate properties. Phase pure monoclinic-scheelite $BiVO_4$ was obtained by MeOH SF-ALD and the resulting films were highly photoactive. Photoactivity was improved by applying a novel PEC activation treatment. Development of a layer-by-layer technique for PEC-functional $BiVO_4$ with improved control over stoichiometry allows for the development of efficient multi-layer devices with advanced architectures.

Acknowledgements

We acknowledge the University of South Carolina for startup funds. This work made use of the South Carolina SAXS Collaborative, supported by the NSF Major Research Instrumentation program (award #DMR-1428620). We thank Arradiance for their dedicated ALD support and Colnatec for the design of a custom low-profile QCM array.

We thank Lijian He and the Mass Spectrometry Center at USC for assistance with composition analysis.

References

(1) Walter, M. G.; Warren, E. L.; McKone, J. R.; Boettcher, S. W.; Mi, Q.; Santori, E. A.; Lewis, N. S. Solar Water Splitting Cells. *Chem. Rev.* **2010**, *110*, 6446–6473.

(2) Kudo, A.; Ueda, K.; Kato, H.; Mikami, I. Photocatalytic O_2 Evolution under Visible Light Irradiation on $BiVO_4$ in Aqueous $AgNO_3$ Solution. *Catal. Letters* **1998**, *53*, 229–230.

(3) Tokunaga, S.; Kato, H.; Kudo, A. Selective Preparation of Monoclinic and Tetragonal $BiVO_4$ with Scheelite Structure and Their Photocatalytic Properties. *Chem. Mater.* **2001**, *13*, 4624–4628.

(4) Abdi, F. F.; Han, L.; Smets, A. H. M.; Zeman, M.; Dam, B.; van de Krol, R. Efficient Solar Water Splitting by Enhanced Charge Separation in a Bismuth Vanadate-Silicon Tandem Photoelectrode. *Nat. Commun.* **2013**, *4*, 2195–2202.

(5) Kim, T. W.; Choi, K.-S. Nanoporous BiVO4 Photoanodes with Dual-Layer Oxygen Evolution Catalysts for Solar Water Splitting. *Science.* **2014**, *343*, 990–994.

(6) Huang, Z.-F.; Pan, L.; Zou, J.-J.; Zhang, X.; Wang, L. Nanostructured Bismuth Vanadate-Based Materials for Solar-Energy-Driven Water Oxidation: A Review on Recent Progress. *Nanoscale* **2014**, *6*, 14044–14063.

(7) Shi, X.; Choi, I. Y.; Zhang, K.; Kwon, J.; Kim, D. Y.; Lee, J. K.; Oh, S. H.; Kim, J. K.; Park, J. H. Efficient Photoelectrochemical Hydrogen Production from Bismuth Vanadate-Decorated Tungsten Trioxide Helix Nanostructures. *Nat. Commun.* **2014**, *5*, 4775–4783.

(8) Pihosh, Y.; Turkevych, I.; Mawatari, K.; Uemura, J.; Kazoe, Y.; Kosar, S.; Makita,

K.; Sugaya, T.; Matsui, T.; Fujita, D.; *et al.* ESI: Photocatalytic Generation of Hydrogen by Core-Shell WO3/BiVO4 Nanorods with Ultimate Water Splitting Efficiency. *Sci. Rep.* **2015**.

(9) Kuang, Y.; Jia, Q.; Nishiyama, H.; Yamada, T.; Kudo, A.; Domen, K. A Front-Illuminated Nanostructured Transparent BiVO4 Photoanode for +2% Efficient Water Splitting. *Adv. Energy Mater.* **2016**, *6*, 1501645.

(10) Abdi, F. F.; van de Krol, R. Nature and Light Dependence of Bulk Recombination in Co-Pi-Catalyzed BiVO 4 Photoanodes. *J. Phys. Chem. C* **2012**, *116*, 9398–9404.

(11) Kayes, B. M.; Atwater, H. A.; Lewis, N. S. Comparison of the Device Physics Principles of Planar and Radial P-n Junction Nanorod Solar Cells. *J. Appl. Phys.* **2005**, *97*, 114302.

(12) Maiolo, J. R.; Kayes, B. M.; Filler, M. A.; Putnam, M. C.; Kelzenberg, M. D.; Atwater, H. A.; Lewis, N. S. High Aspect Ratio Silicon Wire Array Photoelectrochemical Cells. *J. Am. Chem. Soc.* **2007**, *129*, 12346–12347.

(13) Boettcher, S. W.; Spurgeon, J. M.; Putnam, M. C.; Warren, E. L.; Turner-Evans, D. B.; Kelzenberg, M. D.; Maiolo, J. R.; Atwater, H. A.; Lewis, N. S. Energy-Conversion Properties of Vapor-Liquid-Solid-Grown Silicon Wire-Array Photocathodes. *Science.* **2010**, *327*, 185–187.

(14) Zhang, L.; Reisner, E.; Baumberg, J. J. Al-Doped ZnO Inverse Opal Networks as Efficient Electron Collectors in $BiVO_4$ Photoanodes for Solar Water Oxidation. *Energy Environ. Sci.* **2014**, *7*, 1402.

(15) Su, J.; Guo, L.; Bao, N.; Grimes, C. A. Nanostructured WO_3/$BiVO_4$ Heterojunction Films for Efficient Photoelectrochemical Water Splitting. *Nano Lett.* **2011**, *11*,

1928–1933.

(16) Lin, Y.; Yuan, G.; Sheehan, S.; Zhou, S.; Wang, D. Hematite-Based Solar Water Splitting: Challenges and Opportunities. *Energy Environ. Sci.* **2011**, *4*, 4862.

(17) Lin, Y.; Zhou, S.; Sheehan, S. W.; Wang, D. Nanonet-Based Hematite Heteronanostructures for Efficient Solar Water Splitting. *J. Am. Chem. Soc.* **2011**, *133*, 2398–2401.

(18) Lin, Y.; Xu, Y.; Mayer, M. T.; Simpson, Z. I.; McMahon, G.; Zhou, S.; Wang, D. Growth of P-Type Hematite by Atomic Layer Deposition and Its Utilization for Improved Solar Water Splitting. *J. Am. Chem. Soc.* **2012**, *134*, 5508–5511.

(19) Mayer, M. T.; Du, C.; Wang, D. Hematite/Si Nanowire Dual-Absorber System for Photoelectrochemical Water Splitting at Low Applied Potentials. *J. Am. Chem. Soc.* **2012**, *134*, 12406–12409.

(20) Hamann, T. W. Splitting Water with Rust: Hematite Photoelectrochemistry. *Dalt. Trans.* **2012**, *41*, 7830.

(21) Klahr, B.; Gimenez, S.; Fabregat-Santiago, F.; Bisquert, J.; Hamann, T. W. Photoelectrochemical and Impedance Spectroscopic Investigation of Water Oxidation with "Co–Pi"-Coated Hematite Electrodes. *J. Am. Chem. Soc.* **2012**, *134*, 16693–16700.

(22) Zandi, O.; Klahr, B. M.; Hamann, T. W. Highly Photoactive Ti-Doped α-Fe2O3 Thin Film Electrodes: Resurrection of the Dead Layer. *Energy Environ. Sci.* **2013**, *6*, 634–642.

(23) Young, K. M. H.; Hamann, T. W. Enhanced Photocatalytic Water Oxidation Efficiency with Ni(OH)2 Catalysts Deposited on α-Fe2O3 via ALD. *Chem.*

Commun. **2014**, *50*, 8727.

(24) Zandi, O.; Beardslee, J. A.; Hamann, T. Substrate Dependent Water Splitting with Ultrathin α-Fe2O3 Electrodes. *J. Phys. Chem. C* **2014**, *118*, 16494–16503.

(25) Zandi, O.; Hamann, T. W. Enhanced Water Splitting Efficiency Through Selective Surface State Removal. *J. Phys. Chem. Lett.* **2014**, *5*, 1522–1526.

(26) Le Formal, F.; Tétreault, N.; Cornuz, M.; Moehl, T.; Grätzel, M.; Sivula, K. Passivating Surface States on Water Splitting Hematite Photoanodes with Alumina Overlayers. *Chem. Sci.* **2011**, *2*, 737–743.

(27) Hisatomi, T.; Le Formal, F.; Cornuz, M.; Brillet, J.; Tétreault, N.; Sivula, K.; Grätzel, M. Cathodic Shift in Onset Potential of Solar Oxygen Evolution on Hematite by 13-Group Oxide Overlayers. *Energy Environ. Sci.* **2011**, *4*, 2512.

(28) Steier, L.; Herraiz-Cardona, I.; Gimenez, S.; Fabregat-Santiago, F.; Bisquert, J.; Tilley, S. D.; Grätzel, M. Understanding the Role of Underlayers and Overlayers in Thin Film Hematite Photoanodes. *Adv. Funct. Mater.* **2014**, *24*, 7681–7688.

(29) Steier, L.; Luo, J.; Schreier, M.; Mayer, M. T.; Sajavaara, T.; Grätzel, M. Low-Temperature Atomic Layer Deposition of Crystalline and Photoactive Ultrathin Hematite Films for Solar Water Splitting. *ACS Nano* **2015**, *9*, 11775–11783.

(30) Hisatomi, T.; Dotan, H.; Stefik, M.; Sivula, K.; Rothschild, A.; Grätzel, M.; Mathews, N. Enhancement in the Performance of Ultrathin Hematite Photoanode for Water Splitting by an Oxide Underlayer. *Adv. Mater.* **2012**, *24*, 2699–2702.

(31) Stefik, M.; Cornuz, M.; Mathews, N.; Hisatomi, T.; Mhaisalkar, S.; Grätzel, M. Transparent, Conducting Nb:SnO2 for Host–Guest Photoelectrochemistry. *Nano Lett.* **2012**, *12*, 5431–5435.

(32) Riha, S. C.; DeVries Vermeer, M. J.; Pellin, M. J.; Hupp, J. T.; Martinson, A. B. F. Hematite-Based Photo-Oxidation of Water Using Transparent Distributed Current Collectors. *ACS Appl. Mater. Interfaces* **2013**, *5*, 360–367.

(33) Riha, S. C.; Racowski, J. M.; Lanci, M. P.; Klug, J. A.; Hock, A. S.; Martinson, A. B. F. Phase Discrimination through Oxidant Selection in Low-Temperature Atomic Layer Deposition of Crystalline Iron Oxides. *Langmuir* **2013**, *29*, 3439–3445.

(34) Klug, J. A.; Becker, N. G.; Riha, S. C.; Martinson, A. B. F.; Elam, J. W.; Pellin, M. J.; Proslier, T. Low Temperature Atomic Layer Deposition of Highly Photoactive Hematite Using Iron(III) Chloride and Water. *J. Mater. Chem. A* **2013**, *1*, 11607.

(35) Qiu, Y.; Leung, S.-F.; Zhang, Q.; Hua, B.; Lin, Q.; Wei, Z.; Tsui, K.; Zhang, Y.; Yang, S.; Fan, Z. Efficient Photoelectrochemical Water Splitting with Ultrathin Films of Hematite on Three-Dimensional Nanophotonic Structures. *Nano Lett.* **2014**, *14*, 2123–2129.

(36) Paracchino, A.; Laporte, V.; Sivula, K.; Grätzel, M.; Thimsen, E. Highly Active Oxide Photocathode for Photoelectrochemical Water Reduction. *Nat. Mater.* **2011**, *10*, 456–461.

(37) Paracchino, A.; Mathews, N.; Hisatomi, T.; Stefik, M.; Tilley, S. D.; Grätzel, M. Ultrathin Films on Copper(i) Oxide Water Splitting Photocathodes: A Study on Performance and Stability. *Energy Environ. Sci.* **2012**, *5*, 8673.

(38) Tilley, S. D.; Schreier, M.; Azevedo, J.; Stefik, M.; Grätzel, M. Ruthenium Oxide Hydrogen Evolution Catalysis on Composite Cuprous Oxide Water Splitting Photocathodes. *Adv. Funct. Mater.* **2014**, *24*, 303–311.

(39) Azevedo, J.; Steier, L.; Dias, P.; Stefik, M.; Sousa, C. T.; Araújo, J. P.; Mendes, A.;

Graetzel, M.; Tilley, S. D. On the Stability Enhancement of Cuprous Oxide Water Splitting Photocathodes by Low Temperature Steam Annealing. *Energy Environ. Sci.* **2014**, *7*, 4044–4052.

(40) Wang, T.; Luo, Z.; Li, C.; Gong, J. Controllable Fabrication of Nanostructured Materials for Photoelectrochemical Water Splitting via Atomic Layer Deposition. *Chem. Soc. Rev.* **2014**, *43*, 7469–7484.

(41) Hu, S.; Shaner, M. R.; Beardslee, J. A.; Lichterman, M.; Brunschwig, B. S.; Lewis, N. S. Amorphous TiO2 Coatings Stabilize Si, GaAs, and GaP Photoanodes for Efficient Water Oxidation. *Science.* **2014**, *344*, 1005–1009.

(42) Huang, Z.-F.; Song, J.; Pan, L.; Zhang, X.; Wang, L.; Zou, J.-J. Tungsten Oxides for Photocatalysis, Electrochemistry, and Phototherapy. *Adv. Mater.* **2015**, *27*, 5309–5327.

(43) Stefik, M. Atomic Layer Deposition of Bismuth Vanadates for Solar Energy Materials. *ChemSusChem* **2016**, *9*, 1727–1735.

(44) Yanguas-Gil, A.; Peterson, K. E.; Elam, J. W. Controlled Dopant Distribution and Higher Doping Efficiencies by Surface-Functionalized Atomic Layer Deposition. *Chem. Mater.* **2011**, *23*, 4295–4297.

(45) Yanguas-Gil, A.; Libera, J. A.; Elam, J. W. Modulation of the Growth Per Cycle in Atomic Layer Deposition Using Reversible Surface Functionalization. *Chem. Mater.* **2013**, *25*, 4849–4860.

(46) Feng, H.; Libera, J. A.; Stair, P. C.; Miller, J. T.; Elam, J. W. Subnanometer Palladium Particles Synthesized by Atomic Layer Deposition. *ACS Catal.* **2011**, *1*, 665–673.

(47) Seaman, C. H. Calibration of Solar Cells by the Reference Cell Method—The Spectral Mismatch Problem. *Sol. Energy* **1982**, *29*, 291–298.

(48) Toma, F. M.; Cooper, J. K.; Kunzelmann, V.; McDowell, M. T.; Yu, J.; Larson, D. M.; Borys, N. J.; Abelyan, C.; Beeman, J. W.; Yu, K. M.; *et al.* Mechanistic Insights into Chemical and Photochemical Transformations of Bismuth Vanadate Photoanodes. *Nat. Commun.* **2016**, *7*, 12012.

(49) Kim, T. W.; Choi, K.-S. Improving Stability and Photoelectrochemical Performance of BiVO4 Photoanodes in Basic Media by Adding a ZnFe2O4 Layer. *J. Phys. Chem. Lett.* **2016**, *7*, 447–451.

(50) Badot, J. C.; Ribes, S.; Yousfi, E. B.; Vivier, V.; Pereira-Ramos, J. P.; Baffier, N.; Lincot, D. Atomic Layer Epitaxy of Vanadium Oxide Thin Films and Electrochemical Behavior in Presence of Lithium Ions. *Electrochem. Solid-State Lett.* **1999**, *3*, 485.

(51) Abdi, F. F.; Savenije, T. J.; May, M. M.; Dam, B.; van de Krol, R. The Origin of Slow Carrier Transport in BiVO 4 Thin Film Photoanodes: A Time-Resolved Microwave Conductivity Study. *J. Phys. Chem. Lett.* **2013**, *4*, 2752–2757.

(52) Pala, R. A.; Leenheer, A. J.; Lichterman, M.; Atwater, H. A.; Lewis, N. S. Measurement of Minority-Carrier Diffusion Lengths Using Wedge-Shaped Semiconductor Photoelectrodes. *Energy Environ. Sci.* **2014**, *7*, 3424–3430.

(53) Dotan, H.; Sivula, K.; Grätzel, M.; Rothschild, A.; Warren, S. C. Probing the Photoelectrochemical Properties of Hematite (α-Fe2O3) Electrodes Using Hydrogen Peroxide as a Hole Scavenger. *Energy Environ. Sci.* **2011**, *4*, 958–964.

(54) Zhong, D. K.; Choi, S.; Gamelin, D. R. Near-Complete Suppression of Surface

Recombination in Solar Photoelectrolysis by “Co-Pi” Catalyst-Modified W:$BiVO_4$. *J. Am. Chem. Soc.* **2011**, *133*, 18370–18377.

(55) Abdi, F. F.; Firet, N.; van de Krol, R. Efficient BiVO4 Thin Film Photoanodes Modified with Cobalt Phosphate Catalyst and W-Doping. *ChemCatChem* **2013**, *5*, 490–496.

(56) Cesar, I.; Sivula, K.; Kay, A.; Zboril, R.; Grätzel, M. Influence of Feature Size, Film Thickness, and Silicon Doping on the Performance of Nanostructured Hematite Photoanodes for Solar Water Splitting. *J. Phys. Chem. C* **2009**, *113*, 772–782.

(57) Sivula, K.; Formal, F. Le; Grätzel, M. WO3−Fe2O3 Photoanodes for Water Splitting: A Host Scaffold, Guest Absorber Approach. *Chem. Mater.* **2009**, *21*, 2862–2867.

(58) Itoh, K.; Bockris, J. O. Thin Film Photoelectrochemistry: Iron Oxide. *J. Electrochem. Soc.* **1984**, *131*, 126612–126671.

(59) Peters, K.; Lokupitiya, H. N.; Sarauli, D.; Labs, M.; Pribil, M.; Rathouský, J.; Kuhn, A.; Leister, D.; Stefik, M.; Fattakhova-Rohlfing, D. Nanostructured Antimony-Doped Tin Oxide Layers with Tunable Pore Architectures as Versatile Transparent Current Collectors for Biophotovoltaics. *Adv. Funct. Mater.* **2016**, *26*, 6682–6692.

(60) Rossell, M. D.; Agrawal, P.; Borgschulte, A.; Hébert, C.; Passerone, D.; Erni, R. Direct Evidence of Surface Reduction in Monoclinic BiVO 4. *Chem. Mater.* **2015**, *27*, 3593–3600.

(61) Li, T.; He, J.; Peña, B.; Berlinguette, C. P. Curing BiVO4 Photoanodes with Ultraviolet Light Enhances Photoelectrocatalysis. *Angew. Chemie Int. Ed.* **2016**, *55*, 1769–1772.

(62) Trześniewski, B. J.; Smith, W. A. Photocharged BiVO4 Photoanodes for Improved Solar Water Splitting. *J. Mater. Chem. A* **2016**, *4*, 2919–2926.

(63) Wang, G.; Ling, Y.; Lu, X.; Qian, F.; Tong, Y.; Zhang, J. Z.; Lordi, V.; Rocha Leao, C.; Li, Y. Computational and Photoelectrochemical Study of Hydrogenated Bismuth Vanadate. *J. Phys. Chem. C* **2013**, *117*, 10957–10964.

(64) Jiang, H.; Dai, H.; Meng, X.; Ji, K.; Zhang, L.; Deng, J. Porous Olive-like BiVO4: Alcoho-Hydrothermal Preparation and Excellent Visible-Light-Driven Photocatalytic Performance for the Degradation of Phenol. *Appl. Catal. B Environ.* **2011**, *105*, 326–334.

(65) Bard, A. J.; Bocarsly, A. B.; Fan, F. R. F.; Walton, E. G.; Wrighton, M. S. The Concept of Fermi Level Pinning at Semiconductor/Liquid Junctions. Consequences for Energy Conversion Efficiency and Selection of Useful Solution Redox Couples in Solar Devices. *J. Am. Chem. Soc.* **1980**, *102*, 3671–3677.

(66) Du, C.; Zhang, M.; Jang, J.; Liu, Y.; Liu, G.; Wang, D. Observation and Alteration of Surface States of Hematite Photoelectrodes. *J. Phys. Chem. C* **2014**, *118*, 17054–17059.

(67) Klahr, B.; Hamann, T. Water Oxidation on Hematite Photoelectrodes: Insight into the Nature of Surface States through In Situ Spectroelectrochemistry. *J. Phys. Chem. C* **2014**, *118*, 10393–10399.

(68) Schuisky, M.; Kukli, K.; Ritala, M.; Hårsta, A.; Leskelä, M. Atomic Layer CVD in the Bi–Ti–O System. *Chem. Vap. Depos.* **2000**, *6*, 139–145.

CHAPTER 3:
ALD OF SPACE-EFFICIENT SnO_2 UNDERLAYERS FOR $BiVO_4$ HOST-GUEST ARCHITECTURES FOR PHOTOASSISTED WATER SPLITTING[7]

[7] Lamm, B.; Zhou, L.; Rao, P.; Stefik, M. *ChemSusChem* **2019**, DOI: 10.1002/cssc.201802566. Reproduced here with permission from the publisher.

Abstract

Bismuth vanadate ($BiVO_4$) is promising for solar-assisted water splitting. The performance of $BiVO_4$ is limited by charge separation for >70 nm films or by light harvesting for <700 nm films. To resolve this mismatch, host-guest architectures use thin film coatings on 3D scaffolds. Recombination, however, is exacerbated at the extended host-guest interface. Underlayers are used to limit this recombination with a host-underlayer-guest series. Such underlayers consume precious pore volume where typical SnO_2 underlayers are optimized with 65-80 nm. Here we examine conformal and ultrathin SnO_2 underlayers with low defect density produced by atomic layer deposition (ALD). This shifts the optimized thickness to just 8 nm with significantly improved space-efficiency. The materials chemistry thus determines the dimension optimization. Lastly, we demonstrate host-guest architectures with an applied bias photon-to-charge efficiency of 0.71%, a new record for a photoanode absorber prepared by ALD.

Introduction

Bismuth vanadate has for the past decade been studied as a photoanode for photoelectrochemical (PEC) water splitting,[1] with continuous performance gains over time.[2–11] The monoclinic-scheelite phase (m-$BiVO_4$) is the highest efficiency allotrope, with a conduction band edge near 0 V *vs.* the reversible hydrogen electrode (RHE). The valence band edge is near 2.4 V *vs.* RHE and the band gap is 2.4 eV.[2,12,13] This band alignment provides holes in the valence band with excess potential to photo-oxidize water (1.23 V *vs.* RHE) while electrons have a potential almost suitable for hydrogen evolution (0 V *vs.* RHE), requiring mild external bias.

Bismuth vanadate requires an optical thickness of ~700 nm for efficient light harvesting that is much larger than the sum of the limiting carrier diffusion length and the depletion

width.[5,13,14] Electron transport is generally cited as the limiting carrier for charge separation with a transport length of ~70 nm.[5,13,14] This combination of characteristics makes solid, compact $BiVO_4$ films inherently inefficient. In contrast, the "host-guest" approach (Figure 3.1c) decouples this mismatch of carrier transport from optical absorption by using $BiVO_4$ thin films ("guest") upon a transparent, conductive scaffold ("host").[3,8,10] This approach is sometimes called "extremely thin absorber" (ETA).[3,15–18] Recombination is, however, exacerbated with such high surface area devices where carriers are generated in close proximity to recombination sites at the host-guest interface (Figure 3.1a). A well-known method to mitigate recombination at such interfaces is to use an underlayer to block minority carriers (Figure 3.1b). For n-type materials like $BiVO_4$, the underlayer is sometimes called a hole blocking layer or a "hole mirror."[6,19–25] Previous works have commonly utilized tin oxide (SnO_2)[2,14,19,21–23,25–32] and tungsten oxide (WO_3),[3,30,33] where SnO_2 is perhaps the most studied underlayer material for $BiVO_4$. Other materials that have been used as interfacial layers in $BiVO_4$ photoanodes include TiO_2,[34,35] Lu_2O_3,[20] and GaO_xN_{1-x};[36] SnO_2 was selected for this study based on its suitable band alignment relative to $BiVO_4$, stability, low-cost, and as-yet unexplored investigation as a $BiVO_4$ underlayer using atomic layer deposition (ALD). Popular synthetic methods for SnO_2, e.g. spray pyrolysis, yield optimal PEC performance with 65-80 nm of underlayer thickness.[2,21] With such a large film thickness, clearly more is at play than rectification. The optimal underlayer will (1) fully cover the host interface, preventing access to recombination sites located in the FTO, (2) not provide a new set of defects that promote recombination, and (3) have minimal thickness to limit the resistance for electron transport to the electrical contact. The optimal underlayer thickness for different synthesis routes is of minor

importance for flat compact films; however, it poses a significant limitation for practical use in 3D host-guest architectures with limited free-volume. Consider a design with 30 nm $BiVO_4$, 80 nm SnO_2, and a 3D porous host – it would require a 250 nm pore diameter to accommodate such a coating while leaving behind a nominal 30 nm final pore size. Such thick underlayers thus limit host-guest implementation by requiring large feature sizes that impose a poor balance of roughness factor to the out-of-plane transport length. Furthermore, such a scenario would require >50 vol% of non-photoactive material. The consequences of such spatially-inefficient and material-inefficient designs are shown schematically in Figure 3.1c/d. There are clear and significant benefits for the rational development of space-efficient underlayers.

Here we examine the efficacy of conformal and low carrier density SnO_2 thin films prepared by ALD as underlayers for $BiVO_4$ PEC films. The use of an ALD synthesis method enables an optimized PEC performance with just an 8 nm underlayer. This result highlights the role of conformal character and minimal carrier density (i.e. low defect density) upon developing space-efficient underlayers. Finally, we demonstrate enhanced performance for host-guest architectures built upon antimony-doped tin oxide supports with a 0.71% applied bias proton-to-charge efficiency (ABPE) and a 3.7x improved photocurrent at 1.23 V *vs.* RHE as compared to the analogous flat film design.

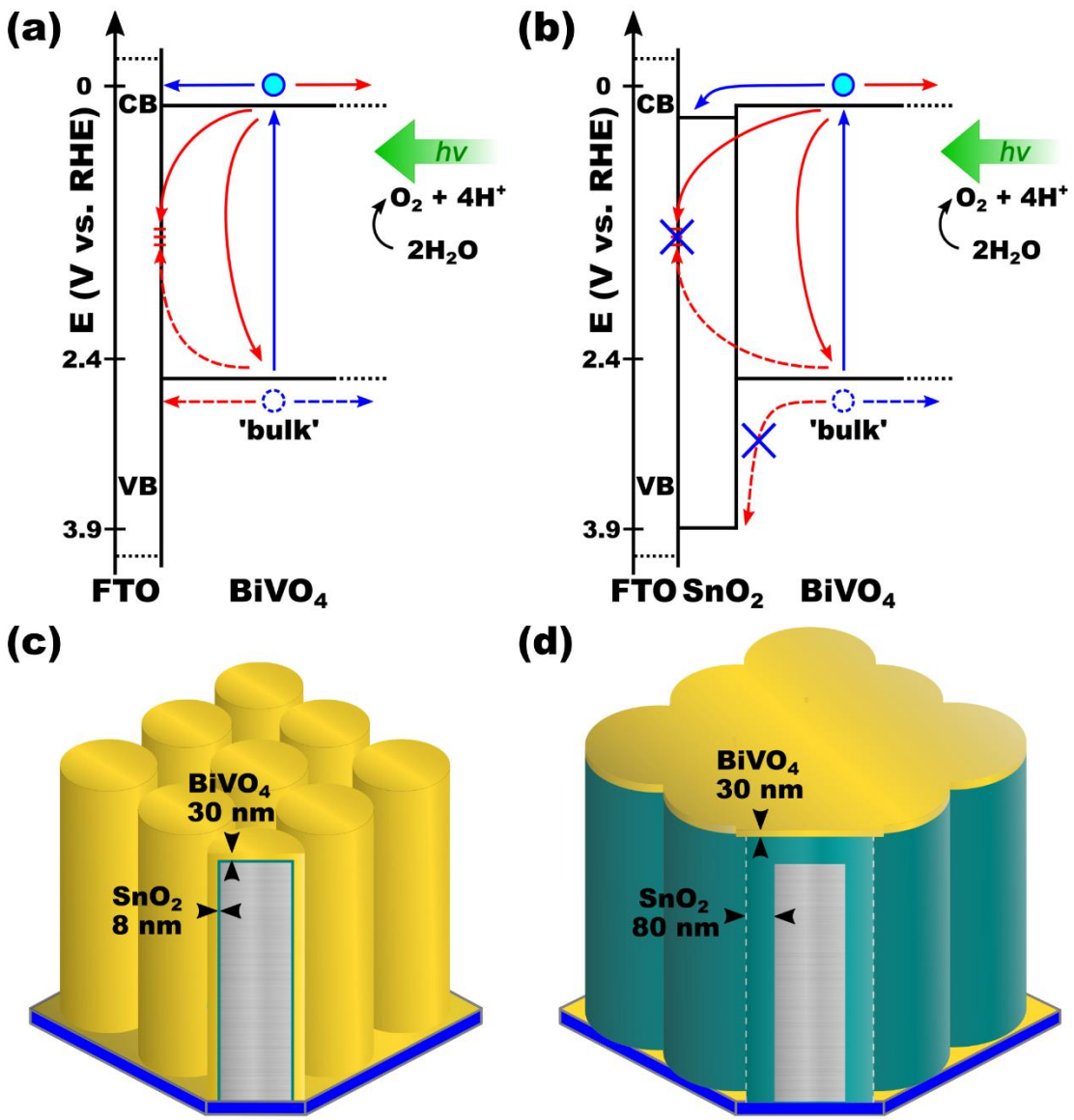

Figure 3.1 Recombination at the FTO interface with $BiVO_4$ (a) is mitigated by addition of an underlayer composed of SnO_2 (b). The importance of a space-efficient underlayer is shown graphically where limited pore dimensions are only compatible with space-efficient underlayers (c) whereas typical thicker underlayers would fully occupy the free pore volume, preventing realization of a host-guest architecture (d). Here $BiVO_4$ is drawn as yellow, SnO_2 as teal, and ATO nanowires are gray.

Results and Discussion

Photogenerated holes within $BiVO_4$ would ideally all react at the water interface, producing solar fuel. However, holes generated in $BiVO_4$ near the electron-rich FTO can undergo recombination and reduce the quantum efficiency. FTO-absorber interfaces are

known to broadly promote recombination for diverse PEC materials,[19,37–41] suggesting that the defects from deliberate fluorine incorporation are recombination sites. Previous reports utilized undoped SnO_2 as an underlayer for $BiVO_4$ where optimal thicknesses were ~80 nm,[2,21] and thinner SnO_2 underlayers did not efficiently inhibit recombination. Common synthetic routes for SnO_2 such as spray pyrolysis result in non-conformal underlayers with relatively high carrier concentrations (10^{19}-10^{21} cm^{-3}, Table C.1). These high carrier concentrations perhaps are a result of using $SnCl_4$, resulting in halide defects similar to FTO and high free-carrier densities. We hypothesize that space-efficient underlayers will require conformal coating techniques with low defect density. The SnO_2 produced by well-known ALD protocols yields an ideal candidate to test this hypothesis with a conformal deposition technique that results in an order of magnitude reduced carrier density (Table C.1).[42,43] The free carriers in SnO_2 come from multiple candidate defects, including oxygen vacancies, tin interstitials, and extrinsic dopants such as Sb^{5+}, F^{-}, and Cl^{-}.[44,45] While these defects improve conductivity in SnO_2, they are also possible recombination sites for PEC devices. Here, the use of a halide-free SnO_2 precursor (TDMASn) prevents halide-doping[44,45] while the use of a strong oxidizing agent (ozone) suppresses the formation of oxygen vacancies, thus avoiding several of the candidate recombination centers. ALD also has the advantage of being a self-limiting deposition technique that facilitates conformal surface coatings within 3D porous substrates having a high roughness factor.[42,43,46]

PEC performance vs. SnO_2 thickness

Looking towards space-efficient underlayers, we examined the efficacy of thin 2-32 nm SnO_2 underlayers with low defect density prepared by ALD. With a SnO_2 growth rate of 0.692 Å per cycle, this corresponds to samples made using 30-480 SnO_2 cycles of $(TDMASn\text{-}O_3)_x$; where sample names and corresponding characteristics are described in

Table 3.1. The inclusion of an SnO_2 underlayer had no observed effect on the $BiVO_4$ crystal structure, as measured by grazing-incidence wide angle X-ray scattering (GIWAXS; Figure 3.2a). Here the only GIWAXS changes noted are the increased intensity of peaks indexed to tetragonal SnO_2 (cassiterite), corresponding to an increasing SnO_2 thickness. Additionally, the SnO_2 underlayer had no apparent effect on UV-vis absorptance in the measured wavelength range, regardless of underlayer thickness (Figure 3.2b). Here the UV absorption by the FTO-coated substrates obscures the absorption of such thin ALD SnO_2 films. Consistent with prior reports,[5,7] the growth of $BiVO_4$ by SF-ALD resulted in conformal films (Figure 3.3). The growth rate here was determined by SEM to be 0.0746 Å per cycle when grown upon FTO or SnO_2.

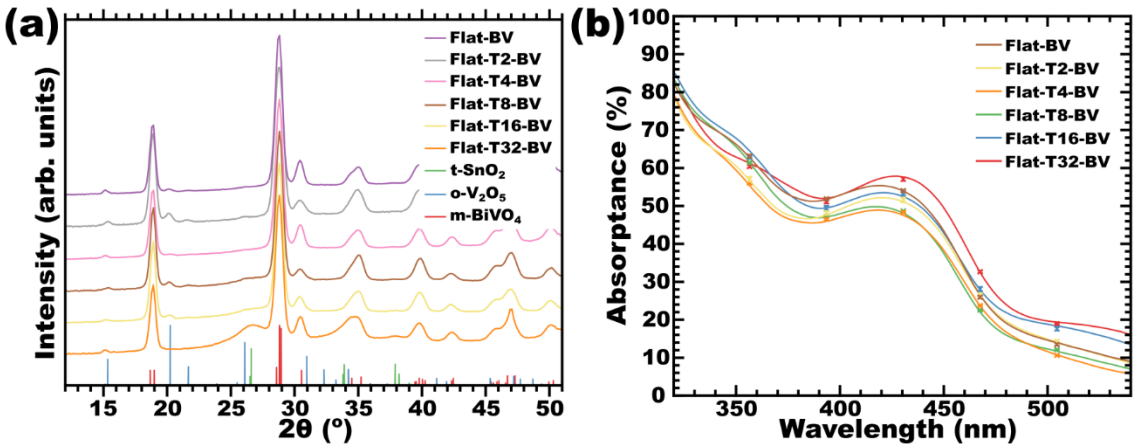

Figure 3.2. GIWAXS measurements of flat $BiVO_4$ samples with and without underlayers (a) as well as the corresponding UV-visible absorptance spectra (b).

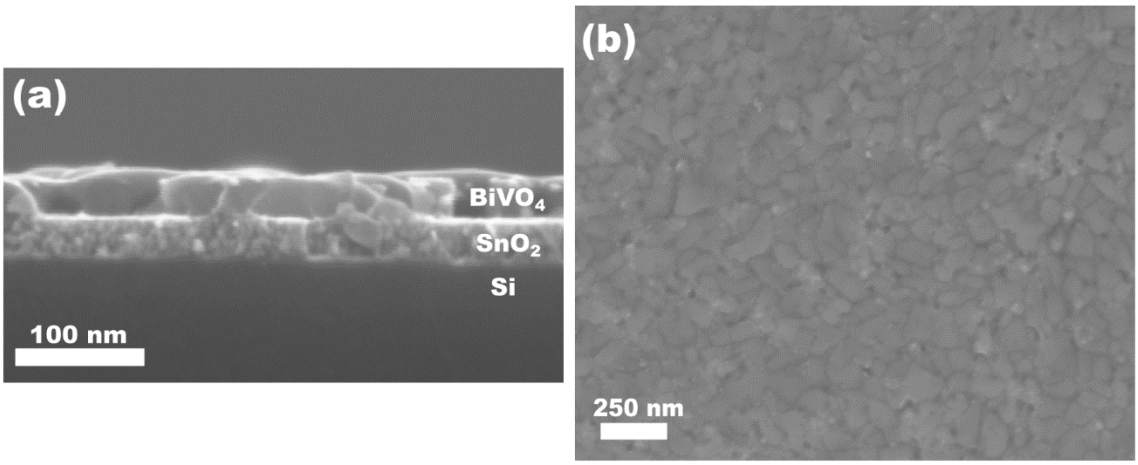

Figure 3.3. SEM images of sample Flat-T32-BV on Si in cross-section (a) and of sample Flat-T8-BV on FTO from top-view (b).

Table 3.1. Flat sample nomenclature and synthesis descriptions.

Name	Substrate	SnO_2 cycles [#] and thickness [nm]	$BiVO_4$ cycles [#] and thickness [nm]
Flat-BV	TEC-15 FTO	0-0	4000-30
Flat-T2-BV	TEC-15 FTO	30-2	4000-30
Flat-T4-BV	TEC-15 FTO	60-4	4000-30
Flat-T8-BV	TEC-15 FTO	120-8	4000-30
Flat-T16-BV	TEC-15 FTO	240-16	4000-30
Flat-T32-BV	TEC-15 FTO	480-32	4000-30

The charge separation efficiency (φ_{sep}) was measured as a function of the ALD SnO_2 underlayer thickness. Here, the PEC performance was measured in the presence of a hole-scavenging sulfite electrolyte to pin the charge injection efficiency at nearly 100% ($\varphi_{inj} \approx 1$). Thus, the measured photocurrents represent the product of the light harvesting efficiency (LHE) and the voltage-dependent φ_{sep} (Equations 3.1 and 3.2):[47,48]

$$J_{H2O}(\mathrm{V}) = J_{abs} \cdot \phi_{sep}(\mathrm{V}) \cdot \phi_{inj}(\mathrm{V}) \tag{3.1}$$

$$J_{sulfite}(\mathrm{V}) = J_{abs} \cdot \phi_{sep}(\mathrm{V}) \tag{3.2}$$

Where J_{abs} is the photon absorption rate expressed as a current density (determined by the illumination spectra and LHE). The SnO_2 underlayers absorbed little light since SnO_2 is a wide-bandgap material (E_g ~3.6-4.0 V)[46,49–51] and used here as very thin layers. Thus, with

constant $BiVO_4$ film thickness (constant LHE and J_{abs}) the improvements to photocurrent were attributed solely to improvements to φ_{sep} by reducing the rate of interfacial charge recombination. Complete J-V curves are presented for this sample series in Figure 3.4a. For the sake of brevity, we focus the discussion on the most important regime of performance under low applied bias voltage. Sample Flat-BV (without underlayer) exhibited a photocurrent of 0.19 mA cm^{-2} at 0.7 V *vs.* RHE, corresponding to φ_{sep}= 6.9% (Figure 3.4b). The addition of a SnO_2 underlayer significantly improved the photocurrent and φ_{sep} monotonically until reaching a performance maximum with an 8 nm thick SnO_2 underlayer. This sample (denoted Flat-T8-BV) gave a photocurrent of 0.41 mA cm^{-2} at 0.7 V *vs.* RHE, corresponding to φ_{sep}= 15.1%. This represents a 2.2x improvement in performance attributed to improved charge separation efficiency with deployment of an optimized underlayer. Samples with yet thicker underlayers, e.g. 16 and 32 nm, exhibited decreased performance, attributed to the ohmic resistance of the undoped SnO_2. This is especially evident in performance of electrodes with a 32 nm SnO_2 underlayer, where PEC performance is reduced to well below that of Flat-BV across most potentials. The thickness trend here is in stark contrast to other reported SnO_2 underlayers that do not exhibit a maximum in performance until a total thickness of ~80 nm. We attribute the difference for ALD SnO_2 to the improved film conformality and the reduced defect concentration evidenced by the low free carrier concentration (Table C.1). The lower performance of very thin films presented here (i.e. 2 and 4 nm SnO_2) could have several causes: (1) there may be pinholes at the early nucleation stage (island growth) of ALD until a conformal layer is established, (2) the crystallization of amorphous ALD SnO_2 may induce pinhole formation for very thin films, SEM images evidence such roughness from the

crystallization process (Figure C.1), and (3) fluorine diffusion from the FTO substrate can induce recombination centers in very thin SnO_2 films. Such diffusion of fluorine into SnO_2 is reported to have a negligible spatial extent for the thermal conditions used here.[52] These performance trends with underlayer thickness were also apparent in the applied bias photon-to-charge efficiencies (defined by Equation C.1)[6] in Figure 3.4c. Here the maximum performance was found for sample Flat-T8-BV with an ABPE of 0.213% at 0.7 V *vs.* RHE as compared to just 0.10% for Flat-BV. An optimal of all performance metrics was found for the 8 nm thick ALD SnO_2, thick enough to suppress recombination and thin enough to avoid excessive resistance.

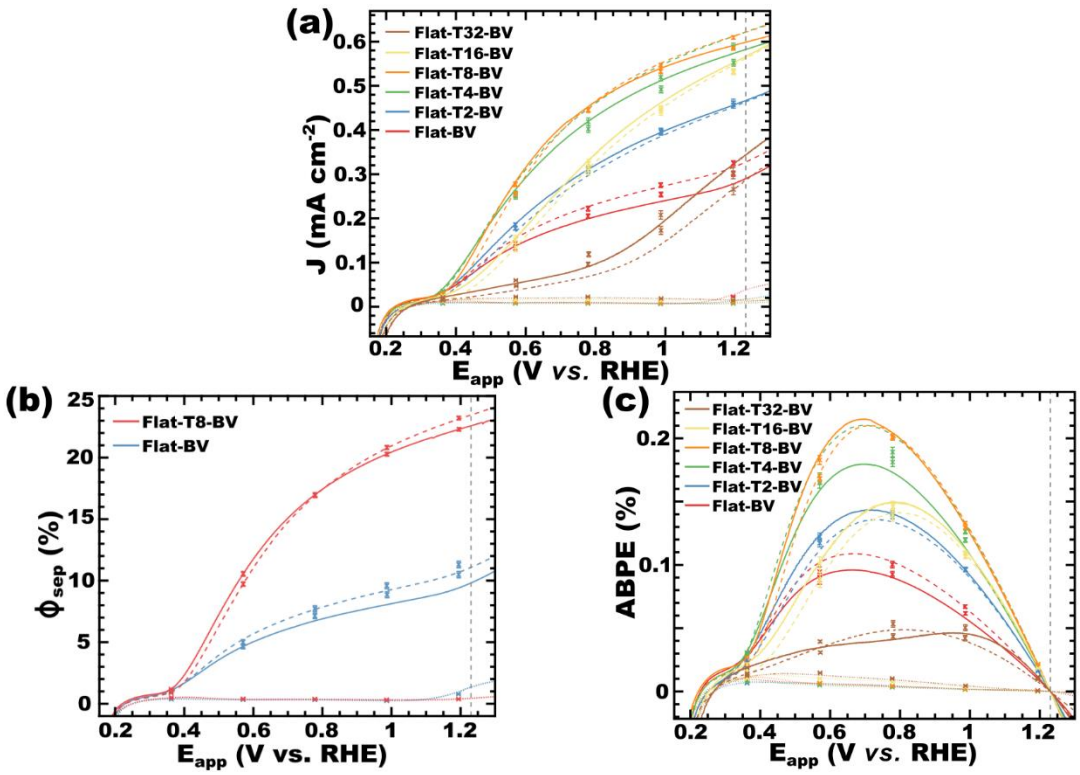

Figure 3.4. Flat $BiVO_4$ PEC performance was measured with different ALD SnO_2 underlayer thicknesses. The photocurrent (a), φ_{sep} (b), and ABPE (c) were measured. The electrolyte was 1.0 M potassium borate with 0.2 M Na_2SO_3 as hole scavenger with a pH of 9.36. Simulated AM1.5 sunlight was used for illuminated measurements. The dark current (dotted), photocurrent with backside illumination (dashed), and photocurrent with frontside illumination (solid) are presented.

PEC performance of host-guest ATO-NTs/SnO_2/$BiVO_4$

The optimized ALD underlayers were applied towards host-guest nanostructures to enhance the photocurrent response. Many previous reports have used cathodic electrodeposition of $BiVO_4$, or precursors thereof.[3,4,13,53–56] The application of cathodic currents is perhaps challenging subsequent to deposition of an underlayer intended to block holes. In contrast, ALD is capable of conformal depositions regardless of the electronic structure of any preceding layers. Our recently developed SF-ALD of $BiVO_4$ is uniquely suited to enable host-guest strategies that include underlayers. A series of 3D nanostructured transparent conductors were used as hosts for the SF-ALD of 30 nm films of $BiVO_4$. The hosts were composed of antimony-doped tin oxide nanotubes (ATO-NTs) prepared by hydrothermal growth and solution deposition, which had variable length from 2.2-2.8 μm.

Host-guest nanostructures were prepared with and without use of SnO_2 underlayers (Table 3.2). SEM micrographs of the resulting host-guest nanostructures are shown in (Figures 3.5 and 3.6). The SF-ALD of $BiVO_4$ appeared to reach the bottom of the ATO films where there was considerable roughness from the ATO nanotube synthesis. The expected $BiVO_4$ thickness of 30 nm was visible with nanotube cross-sections after cleaving the tops of the nanotubes (Figure 3.6). The $BiVO_4$ had some porosity as a result of densification and perhaps loss of residual organics during calcination. The PEC performance was investigated as a function of the prepared architectures. Comparison of host-guest sample ATO2.2-BV (without underlayer) to the corresponding compact Flat-

~17 (Table 3.2). In contrast, the 30 nm thick Flat-BV sample only absorbed 15% of light with 500 nm wavelength (Figure 3.2b). The addition of the optimized underlayer was found to significantly increase PEC performance. Sample ATO2.2-T8-BV yielded a photocurrent 1.33 $mAcm^{-2}$ at 0.7 V *vs.* RHE, a 1.6x result as compared to ATO2.2-BV having the same architecture without an underlayer. This difference in performance for $BiVO_4$ deposited on undoped ALD SnO_2 versus ATO, again suggest a role of free-carrier producing defects upon enhancing interfacial recombination.

Table 3.2 3D Host-guest sample nomenclature and synthesis descriptions.

Name	ATO nanotube length (um)	SnO_2 cycles [#] and thickness [nm]	$BiVO_4$ cycles [#] and thickness [nm]	Roughness factor*	Optical thickness [nm]*
ATO2.2-BV	2.2	0-0	4000-30	15.4	527.9
ATO2.2-T8-BV	2.2	120-8	4000-30	15.4	562.4
ATO2.8-T8-BV	2.8	120-8	4000-30	19.4	707.6
*Calculated from a simplified geometric estimate (see SI for more details).					

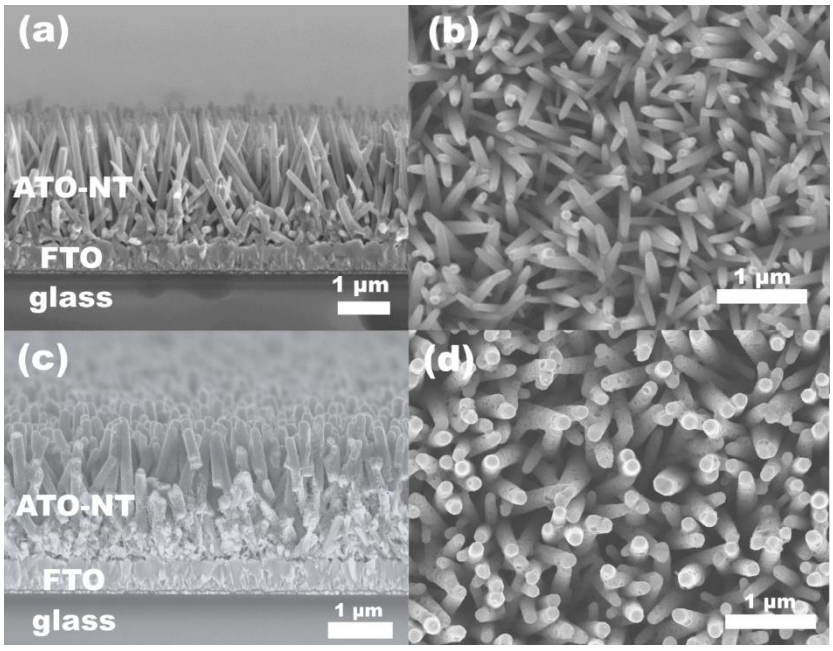

Figure 3.5. SEM images of ATO-NTs before (a, b) and after $BiVO_4$ SF-ALD (c, d). Sample ATO2.2-T8-BV is shown in panels c and d.

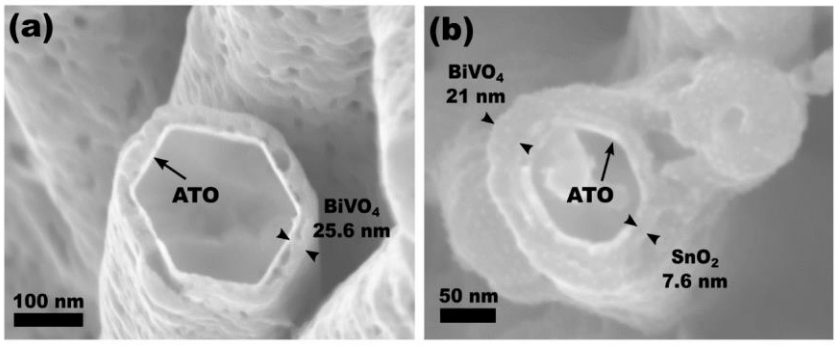

Figure 3.6. Top-view SEM images of samples ATO2.2-BV (a) and ATO2.2-T8-BV (b) after light abrasion to break open nanotubes.

With the beneficial effect of an underlayer demonstrated for these host-guest architectures, we next examined optimization of light harvesting efficiency. A series of samples were compared with increasing nanotube length: ATO2.2-T8-BV and ATO2.8-T8-BV. The photocurrent response was nearly identical with a peak photocurrent of 2.1 mA cm^{-2} at 1.23 V vs RHE (Figure 3.7a). Comparing the estimated optical thickness for these two samples indicates that both are rather close to the ideal dimension of 700 nm for efficient light harvesting of 90% of the below-bandgap AM1.5G spectrum.[6] The lack of an effect from nanotube length and lack of an effect from thus optical thickness here suggests that light harvesting efficiency is not the limiting factor here, but rather the bulk recombination rate of SF-ALD $BiVO_4$. Further improvements to this performance would thus require new developments to manage bulk defect chemistry within $BiVO_4$.[6,17,57–59] The ABPEs were calculated for all host-guest structures investigated with a maximum in performance for samples ATO2.2-T8-BV and ATO2.8-T8-BV having 0.71 % ABPE at 0.71 V vs RHE (Figure 3.7b). These results highlight the advantage of including a space-efficient hole-blocking underlayer within 3D host-guest nanostructures.

The applied bias photon-to-charge efficiency is one of the most important metrics for PEC device performance as it includes the energetic cost of the applied bias.[6] The

performance of PEC devices where the photoabsorber was prepared by ALD have often been lower than other synthetic methodologies. In light of these challenges, it is insightful to compare the performance here to other ALD derived PEC photoanodes. The 0.71% ABPE for sample ATO2.2-T8-BV represents the highest reported PEC performance of any photoanode material produced by ALD, to best of the authors' knowledge (Table 3.3). Interestingly, sample Flat-T8-BV is also the highest performing compact film produced by ALD, highlighting that careful underlayer design is crucial for general performance improvements.

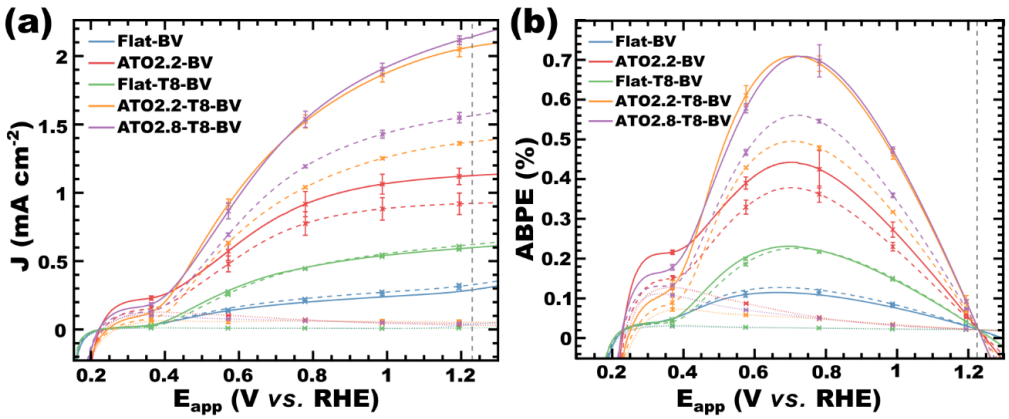

Figure 3.7. Host-Guest PEC performance was measured with and without the optimized underlayer and as a function of nanotube length. The photocurrent (a) and ABPE (b) were measured. The electrolyte was 1.0 M potassium borate with 0.2 M Na_2SO_3 as hole scavenger with a pH of 9.36. Simulated AM1.5 sunlight was used for illuminated measurements. The dark current (dotted), photocurrent with backside illumination (dashed), and photocurrent with frontside illumination (solid) are presented.

Table 3.3 PEC performance of photoanodes with absorber produced by ALD.

Material	ABPE [%]	Photocurrent at 1.23 V vs RHE [$mAcm^{-2}$]
$BiVO_4$ (ATO2.2-T8-BV)	0.71	2.1
WO_3 (host-guest)[60]	0.62	2.1
$BiVO_4$ (Flat-T8-BV)	0.213	0.62
$CuWO_4$ (compact)[61]	0.12	1.1
α-Fe_2O_3 (host-guest)[62]	0.091	1.5
Ta_3N_5 (compact)[63]	0.095	0.79
α-Fe_2O_3 (compact)[64]	0.023	0.32

Conclusion

Bismuth vanadate requires an optical thickness of ~700 nm for efficient light harvesting that is much larger than the limiting carrier transport length of 70 nm.[5,13,14] The host-guest approach decouples this mismatch of carrier transport from optical absorption;[3,8,10] however, recombination at the host-guest interface is exacerbated with such high surface area devices. Tin oxide is a popular underlayer material for $BiVO_4$, acting as a hole-blocking layer typically optimized at 65-80 nm.[2,21] Such thick underlayers, however, consume precious pore volume from the overall 3D host-guest design. The efficacy of low carrier density SnO_2 underlayers were investigated for $BiVO_4$ PEC performance. The use of an ALD synthesis method resulting in more conformal coatings with lower defect densities and enabled optimized PEC performance with only an 8 nm underlayer. Such thin underlayers yield considerably improved space-efficiency for deployment within reasonable host-guest architectures. The materials chemistry was shown to influence the underlayer thickness optimization. Host-guest architectures built upon ATO-nanotubes were demonstrated. SnO_2 underlayers improved the performance where an overall 3.7x improved photocurrent was feasible at 1.23 V vs RHE.

Experimental Methods

Materials

Tetrakis(dimethylamino) tin (TDMASn, 99%), triphenyl bismuth ($BiPh_3$, 99%), and vanadium(V) oxytriisopropoxide (VTIP, 98%) were used as received from STREM. Deionized ultra-filtered (DIUF) water (Fisher), methanol (ACS Grade, Fisher), 2-propanol (70% lab grade, BDH), H_3BO_3 (ACS Grade, VWR Life Science), Na_2SO_3 (ACS Grade, Macron), and KOH (ACS Grade, Fisher) were used as received. TEC-15 fluorine-doped tin oxide coated glass (FTO) was purchased from Hartford Glass. The FTO substrates were cleaned extensively before used with 2-propanol and DIUF water before sonication in

soapy water (Decon Contrex, 2 wt%), followed by additional rinses with water and 2-propanol, followed by sonication in 2-propanol. Polished n-doped silicon wafers with (100) orientation were purchased from University Wafers, USA. The cleaned FTO substrates and silicon wafers were calcined using a Barnstead Thermolyne muffle furnace at 450 ^{o}C for 1 h immediately prior to deposition. High-temperature grade Kapton tape was purchased from McMaster-Carr, USA. Ultra-high purity nitrogen (99.999%) and oxygen (99.5%) were used as received from Praxair.

ATO nanotube synthesis

The hydrothermal growth of ZnO nanorod array (NRA) template was adapted from previous reports.[10,65,66] Arrays of ZnO nanowires were synthesized on 3x3 cm^2 FTO substrates (Hartford Glass, IN), that were cleaned thoroughly by acetone + isopropyl alcohol + deionized water sonication before coating with a seed layer (5 mM acetate dihydrate in ethanol) by spin coating at 2000 rpm for 30 s. Samples with seed layer were annealed at 350 ^{o}C for 30 min.

ZnO nanowires were grown by immersing seeded substrates in aqueous solutions containing 25 mM zinc nitrate hexahydrate (98%, Sigma Aldrich) and 25 mM hexamethylenetetramine (99%, Sigma Aldrich) at 90-95 ^{o}C for 1 hour and 2 hours. To obtain longer nanowire arrays, 1-hour and 2-hour grown substrates were introduced to fresh solution (20 mM zinc nitrate hydrate and 20 mM hexamethylenetetramine) and grown for additional 2 hours. The total growth time for the two types of samples were 2 hours and 3 hours (1 hour followed by 2 hours).

The Sb:SnO_2 nanotube arrays were synthesized by coating Sb:SnO_2 layers onto the ZnO nanowires template. A Sb:SnO_2 solution containing 0.1225 g $SnCl_2$ (98%, Sigma Aldrich) and 0.01 g $SbCl_3$ (99%, Sigma Aldrich) in 10 mL 2-methoxyethanol (99%, Alfa Aesar)

was drop cast onto the ZnO nanowire templates. After 4 layers of Sb:SnO_2 coating, the substrates were annealed in a furnace in air at 550 ^oC for 2 hours to crystallize the Sb:SnO_2 nanotube shell. Then, the ZnO nanowires template with the Sb:SnO_2 shell was etched in acetic acid (99.7%, Sigma Aldrich) for 2 hours and thoroughly washed in deionized water to remove the ZnO nanowires template from the substrates. After first time growth, substrates were again repeatedly drop casted with Sb:SnO_2 solution, annealed in furnace and etched in acetic acid one more time to make the Sb:SnO_2 nanotube arrays with thicker walls.

Atomic layer deposition of tin oxide and bismuth vanadate films

Samples were masked using Kapton tape to define the deposition region on the back and partially on the front to provide clean electrical contacts for PEC measurements. TDMASn was loaded into a stainless steel cylinder in an argon glovebox. The cylinders were sealed and connected to an Arradiance Gemstar-8 reactor. Nitrogen was used as a carrier gas and the purging gas. A Nano ozone generator (Absolute Ozone, Canada) was used to supply ~10 wt% ozone. The ozone generator was primed with flowing O_2 prior to deposition. Nitrogen was used as both the carrier gas and the purging gas. Precursor dosing was controlled using Swagelok ALD valves. The TDMASn was heated to 55 ^oC. The oxidant and precursor manifolds were heated to 100 and 130 ^oC, respectively. The reactor chamber was set to 115 ^oC. The TDMASn and ozone had pulse times of 1500 and 100 ms, respectively. The reactor chamber was isolated before each pulse to contain the precursors for 1 s after exposure ("exposure mode"). Excess precursors were purged after each exposure using 200 sccm nitrogen for 10 s. The deposition was organized into a macrocycle of $(TDMASn\text{-}O_3)_a$ where 'a' controlled total thickness deposited. Tin oxide films on silicon

wafers and FTO were calcined prior to bismuth vanadate deposition. A comprehensive ALD protocol is provided in Table C.2.

Bismuth vanadate deposition followed a previously published surface functionalized ALD (SF-ALD) procedure,[5] following from the original ALD bismuth vanadate demonstration.[7] The $BiPh_3$ and VTIP cylinders were heated to 130 and 45 °C, respectively. The reactor manifolds and chamber were set to 130 °C. Both metal precursors had a pulse time of 2 s, methanol had a pulse time of 50 ms, and water had a pulse time of 25 ms prior to methanol and 100 ms prior to $BiPh_3$. A vapor-boosting 20 ms pulse of nitrogen was added to the $BiPh_3$ cylinder just prior to each pulse. The reactor was isolated in exposure mode for 1 s. Excess precursors were purged after each exposure using 200 sccm nitrogen for 10 s. The deposition was organized into a macrocycle of $(methanol/VTIP/water/BiPh_3/water)_b$ where methanol was used to control composition and 'b' controlled total thickness deposited; a comprehensive ALD protocol is provided in Table C.3.

Film treatments

The ALD films were heated to induce crystallization. Samples were heated at 5 °C min^{-1} to 200 °C, followed by 10 °C min^{-1} to 450 °C, held constant at 450 °C for 1 h, and allowed to cool in the furnace.

Prior to linear sweep voltammetry (LSV), chronoamperometry (CA), and absorptance measurements, films on FTO were exposed to an external bias of 0.6 V *vs.* RHE (–0.153 V *vs.* Ag/AgCl at pH 9.36) under AM 1.5 illumination for 1 h (termed PEC activation).[5,6] Films on ATO NTs were exposed to an identical procedure for 2 h.

Diffraction

X-ray diffraction experiments were conducted using a SAXSLab Ganesha at the South Carolina SAXS Collaborative. A Xenocs GeniX 3D microfocus source was used with a Cu target to generate a monochromatic beam with a 0.154 nm wavelength. The instrument was calibrated using silicon powder (NIST 640d). Scattering data were processed from the scattering vector $q = 4\pi\lambda^{-1}\sin\theta$ where λ is the X-ray wavelength and 2θ is the total scattering angle. A Pilatus 300 K detector (Dectris) was used to collect the two-dimensional (2D) scattering patterns. Samples were measured with the beam at an incident angle of 8^{o} relative to the film plane. SAXSGUI software was used to radially integrate the 2D patterns to produce 1D profiles.

Photoelectrochemical and electrochemical measurements

LSVs were measured using a three-electrode potentiostat (BioLogic SP-150) with a Ag/AgCl/KCl (saturated) reference electrode (Pine Instruments) and a platinum wire counter electrode (Pine Instruments). Samples on FTO substrates were clamped with a titanium sheet to provide an ohmic contact. The electrodes were placed into a cell made of polyether ether ketone (PEEK) with a fused-silica window. Simulated sunlight was generated using a 75 W xenon arc lamp (OBB, Horiba) that passed through a water infrared filter (OBB, Horiba), a KG-3 filter (317-710 nm pass, Edmund Optics), and a BG-40 filter with an antireflective coating (335-610 nm pass, Thorlabs). This combination of filters removed much of the UV light where the Xe lamp has the most spectral mismatch from the AM1.5 spectrum. The transmitted light was collimated using a fused-silica lens (Thorlabs) and passed through an engineered diffuser with a top-hat profile to provide a homogenous intensity profile with a slight 10^{o} divergence. The transmitted light was corrected for brightness in the 335-610 nm spectral range to generate a photocurrent

identical to AM 1.5G sunlight. The illumination intensity was measured using a calibrated UV-enhanced silicon photodiode (Thorlabs) equipped with a neutral reflective filter (optical density 1.0, Thorlabs) to maintain a linear and calibrated photodiode response. This calibration practice provides accurate solar simulation in terms of both spectral distribution and brightness with a minimal correction factor.[67] PEC measurements were performed in 1 M potassium borate with 0.2 M sodium sulfite (Na_2SO_3) as hole scavenger at pH 9.35. It has been well established that potassium phosphate buffers dissolve $BiVO_4$ at working pH values;[4,68,69] however, $BiVO_4$ photoanodes are stable in alkaline borate buffers. The potassium borate solution was prepared by adjusting the pH of 1 M H_3BO_3 in DIUF water to 9.35 ± 0.02 with KOH as confirmed by a calibrated Thermo Scientific OrionStar A211 pH meter. The sulfite acted as a hole scavenge to provide quantitative charge injection from the semiconductor to the electrolyte for the measurement of film performance without catalysts. The samples were scanned from -0.600 to 0.650 V *vs.* Ag/AgCl reference electrode at 10 mV s^{-1}. Multiple scans were completed at each condition to confirm reproducibility and the second scan results were reported. For host-guest samples on ATO nanotubes, N_2 sparging was used during all PEC measurements to circulate the electrolyte and dislodge gas bubbles trapped at the surface.

Quantum efficiencies were calculated based on chronoamperometry (CA) measurements made with monochromatic light while using the same potassium phosphate buffer described above. Illumination was generated using a 150 W xenon lamp (OBB, Horiba) that passed through an 180^o monochromator with a 5 mm slit width and 1200 grates per mm diffraction grating (OBB, Horiba). Transmitted light was collimated using a fused-silica lens (Thorlabs) and passed through an engineered diffusor with a top-hat profile to

provide a homogenous intensity profile with a slight 10^{o} divergence. CA measurements were recorded at 0.4784 V *vs.* Ag/AgCl reference electrode (1.23 V *vs.* RHE) unless otherwise noted. All electrochemical potentials E were reported versus the reversible hydrogen electrode (RHE) using the formula E(*vs.* RHE) = E(*vs.* Ag/AgCl) + E_{ref}(Ag/AgCl) + 0.059 V x pH where E_{ref} = 0.197 V in this case.

For both CA and LSV measurements, representative samples of a given set were plotted with the mean (indicated as '*x*') and bars for the error of the mean.

Optoelectronic properties

The optical response of thin films was measured using a Shimadzu UV-2450. A sandwich configuration of FTO-water-fused quartz was used to minimize light scattering differences between the blank measurement of bare FTO and samples coated onto FTO. Identical measurements on FTO were used to establish the baseline for the measurements of the optical properties of the deposited films alone.

Morphology

A Zeiss Ultra Plus scanning electron microscope (SEM) was operated at 5 kV using an in-lens secondary electron detector to observe the film surface and cross-sectional acquisition. ALD growth rates were calculated based upon cross-sectional SEM imaging of films in the 20-100 nm thickness range.

Hall Effect Measurements

Electronic properties were measured via a Hall probe (MMR Technologies K2500) with 100 nm Al contacts connected by magnetic sputtering to a 500 nm thick SnO_2 sample on quartz. Measurements were made with a 12.5 kG magnetic field and 5.14 nA current. The sample was made by five consecutive 100 nm ALD depositions described above, with heat treatments between each deposition.

Acknowledgements

B.L. and M.S. acknowledge support by the National Science Foundation (DMR-1752615). L.Z. and P.M.R. acknowledge support by the National Science Foundation (DMR-1609538). The authors would like to thank Binod Giri for assistance with Hall effect measurements.

References

(1) Kudo, A.; Ueda, K.; Kato, H.; Mikami, I. Photocatalytic O_2 Evolution under Visible Light Irradiation on $BiVO_4$ in Aqueous $AgNO_3$ Solution. *Catal. Letters* **1998**, *53*, 229–230.

(2) Abdi, F. F.; Han, L.; Smets, A. H. M.; Zeman, M.; Dam, B.; van de Krol, R. Efficient Solar Water Splitting by Enhanced Charge Separation in a Bismuth Vanadate-Silicon Tandem Photoelectrode. *Nat. Commun.* **2013**, *4*, 2195–2202.

(3) Pihosh, Y.; Turkevych, I.; Mawatari, K.; Uemura, J.; Kazoe, Y.; Kosar, S.; Makita, K.; Sugaya, T.; Matsui, T.; Fujita, D.; *et al.* Photocatalytic Generation of Hydrogen by Core-Shell $WO_3/BiVO_4$ Nanorods with Ultimate Water Splitting Efficiency. *Sci. Rep.* **2015**, *5*, 11141.

(4) Kuang, Y.; Jia, Q.; Nishiyama, H.; Yamada, T.; Kudo, A.; Domen, K. A Front-Illuminated Nanostructured Transparent $BiVO_4$ Photoanode for >2% Efficient Water Splitting. *Adv. Energy Mater.* **2016**, *6*, 1501645.

(5) Lamm, B.; Sarkar, A.; Stefik, M. Surface Functionalized Atomic Layer Deposition of Bismuth Vanadate for Single-Phase Scheelite. *J. Mater. Chem. A* **2017**, *5*, 6060–6069.

(6) Lamm, B.; Trześniewski, B. J.; Döscher, H.; Smith, W. A.; Stefik, M. Emerging Postsynthetic Improvements of BiVO 4 Photoanodes for Solar Water Splitting. *ACS*

Energy Lett. **2018**, *3*, 112–124.

(7) Stefik, M. Atomic Layer Deposition of Bismuth Vanadates for Solar Energy Materials. *ChemSusChem* **2016**, *9*, 1727–1735.

(8) Shi, X.; Choi, I. Y.; Zhang, K.; Kwon, J.; Kim, D. Y.; Lee, J. K.; Oh, S. H.; Kim, J. K.; Park, J. H. Efficient Photoelectrochemical Hydrogen Production from Bismuth Vanadate-Decorated Tungsten Trioxide Helix Nanostructures. *Nat. Commun.* **2014**, *5*, 4775–4783.

(9) Butler, K. T.; Dringoli, B. J.; Zhou, L.; Rao, P. M.; Walsh, A.; Titova, L. V. Ultrafast Carrier Dynamics in $BiVO_4$ Thin Film Photoanode Material: Interplay between Free Carriers, Trapped Carriers and Low-Frequency Lattice Vibrations. *J. Mater. Chem. A* **2016**, *4*, 18516–18523.

(10) Zhou, L.; Yang, Y.; Zhang, J.; Rao, P. M. Photoanode with Enhanced Performance Achieved by Coating $BiVO_4$ onto ZnO-Templated Sb-Doped SnO_2 Nanotube Scaffold. *ACS Appl. Mater. Interfaces* **2017**, *9*, 11356–11362.

(11) Zhou, L.; Zhao, C.; Giri, B.; Allen, P.; Xu, X.; Joshi, H.; Fan, Y.; Titova, L. V.; Rao, P. M. High Light Absorption and Charge Separation Efficiency at Low Applied Voltage from Sb-Doped SnO2/BiVO4 Core/Shell Nanorod-Array Photoanodes. *Nano Lett.* **2016**, *16*, 3463–3474.

(12) Tokunaga, S.; Kato, H.; Kudo, A. Selective Preparation of Monoclinic and Tetragonal $BiVO_4$ with Scheelite Structure and Their Photocatalytic Properties. *Chem. Mater.* **2001**, *13*, 4624–4628.

(13) Kim, T. W.; Choi, K.-S. K.-S. Nanoporous $BiVO_4$ Photoanodes with Dual-Layer Oxygen Evolution Catalysts for Solar Water Splitting. *Science.* **2014**, *343*, 990–994.

(14) Abdi, F. F.; Van De Krol, R. Nature and Light Dependence of Bulk Recombination in Co-Pi-Catalyzed $BiVO_4$ Photoanodes. *J. Phys. Chem. C* **2012**, *116*, 9398–9404.

(15) Hisatomi, T.; Dotan, H.; Stefik, M.; Sivula, K.; Rothschild, A.; Grätzel, M.; Mathews, N. Enhancement in the Performance of Ultrathin Hematite Photoanode for Water Splitting by an Oxide Underlayer. *Adv. Mater.* **2012**, *24*, 2699–2702.

(16) Sivula, K.; Le Formal, F.; Grätzel, M. Solar Water Splitting: Progress Using Hematite (α-Fe2O3) Photoelectrodes. *ChemSusChem* **2011**, *4*, 432–449.

(17) Tolod, K.; Hernández, S.; Russo, N. Recent Advances in the $BiVO_4$ Photocatalyst for Sun-Driven Water Oxidation: Top-Performing Photoanodes and Scale-Up Challenges. *Catalysts* **2017**, *7*, 13.

(18) Grätzel, M. Photoelectrochemical Cells. *Nature* **2001**, *414*, 338–344.

(19) Liang, Y.; Tsubota, T.; Mooij, L. P. A.; van de Krol, R. Highly Improved Quantum Efficiencies for Thin Film BiVO4 Photoanodes. *J. Phys. Chem. C* **2011**, *115*, 17594–17598.

(20) Zhang, W.; Yan, D.; Tong, X.; Liu, M. Ultrathin Lutetium Oxide Film as an Epitaxial Hole-Blocking Layer for Crystalline Bismuth Vanadate Water Splitting Photoanodes. *Adv. Funct. Mater.* **2018**, *28*, 1705512.

(21) Byun, S.; Kim, B.; Jeon, S.; Shin, B. Effects of a SnO 2 Hole Blocking Layer in a BiVO 4 -Based Photoanode on Photoelectrocatalytic Water Oxidation. *J. Mater. Chem. A* **2017**, *5*, 6905–6913.

(22) Chatchai, P.; Murakami, Y.; Kishioka, S. -y.; Nosaka, A. Y.; Nosaka, Y. FTO⁄SnO[Sub 2]⁄BiVO[Sub 4] Composite Photoelectrode for Water Oxidation under Visible Light Irradiation. *Electrochem. Solid-State Lett.* **2008**, *11*, H160–

H163.

(23) Alarcón-Lladó, E.; Chen, L.; Hettick, M.; Mashouf, N.; Lin, Y.; Javey, A.; Ager, J. W. $BiVO_4$ Thin Film Photoanodes Grown by Chemical Vapor Deposition. *Phys. Chem. Chem. Phys.* **2014**, *16*, 1651–1657.

(24) Chen, L.; Alarcón-Lladó, E.; Hettick, M.; Sharp, I. D.; Lin, Y.; Javey, A.; Ager, J. W. Reactive Sputtering of Bismuth Vanadate Photoanodes for Solar Water Splitting. *J. Phys. Chem. C* **2013**, *117*, 21635–21642.

(25) Bhat, S. S. M.; Suh, J. M.; Choi, S.; Hong, S.-P.; Lee, S. A.; Kim, C.; Moon, C. W.; Lee, M. G.; Jang, H. W. Substantially Enhanced Front Illumination Photocurrent in Porous SnO 2 Nanorods/Networked BiVO 4 Heterojunction Photoanodes. *J. Mater. Chem. A* **2018**, *6*, 14633–14643.

(26) Liang, Y.; Messinger, J. Improving $BiVO_4$ Photoanodes for Solar Water Splitting through Surface Passivation. *Phys. Chem. Chem. Phys.* **2014**, *16*, 12014.

(27) Sharp, I. D.; Cooper, J. K.; Toma, F. M.; Buonsanti, R. Bismuth Vanadate as a Platform for Accelerating Discovery and Development of Complex Transition-Metal Oxide Photoanodes. *ACS Energy Lett.* **2017**, *2*, 139–150.

(28) Favaro, M.; Abdi, F. F.; Lamers, M.; Crumlin, E. J.; Liu, Z.; van de Krol, R.; Starr, D. E. Light-Induced Surface Reactions at the Bismuth Vanadate/Potassium Phosphate Interface. *J. Phys. Chem. B* **2018**, *122*, 801–809.

(29) Abdi, F. F.; Savenije, T. J.; May, M. M.; Dam, B.; van de Krol, R. The Origin of Slow Carrier Transport in BiVO 4 Thin Film Photoanodes: A Time-Resolved Microwave Conductivity Study. *J. Phys. Chem. Lett.* **2013**, *4*, 2752–2757.

(30) Saito, R.; Miseki, Y.; Sayama, K. Highly Efficient Photoelectrochemical Water

Splitting Using a Thin Film Photoanode of BiVO4/SnO2/WO3 Multi-Composite in a Carbonate Electrolyte. *Chem. Commun.* **2012**, *48*, 3833.

(31) Trześniewski, B. J.; Smith, W. A. Photocharged BiVO 4 Photoanodes for Improved Solar Water Splitting. *J. Mater. Chem. A* **2016**, *4*, 2919–2926.

(32) Trześniewski, B. J.; Digdaya, I. A.; Nagaki, T.; Ravishankar, S.; Herraiz-Cardona, I.; Vermaas, D. A.; Longo, A.; Gimenez, S.; Smith, W. A. Near-Complete Suppression of Surface Losses and Total Internal Quantum Efficiency in $BiVO_4$ Photoanodes. *Energy Environ. Sci.* **2017**, *10*, 1517–1529.

(33) Pihosh, Y.; Turkevych, I.; Mawatari, K.; Asai, T.; Hisatomi, T.; Uemura, J.; Tosa, M.; Shimamura, K.; Kubota, J.; Domen, K.; *et al.* Nanostructured WO3/BiVO4 Photoanodes for Efficient Photoelectrochemical Water Splitting. *Small* **2014**, *10*, 3692–3699.

(34) Zhang, H.; Cheng, C. Three-Dimensional FTO/TiO 2 /BiVO 4 Composite Inverse Opals Photoanode with Excellent Photoelectrochemical Performance. *ACS Energy Lett.* **2017**, *2*, 813–821.

(35) Gu, J.; Huang, Q.; Yuan, Y.; Ye, K.-H.; Wang, Z.; Mai, W. In Situ Growth of a TiO 2 Layer on a Flexible Ti Substrate Targeting the Interface Recombination Issue of BiVO 4 Photoanodes for Efficient Solar Water Splitting. *J. Mater. Chem. A* **2017**, *5*, 20195–20201.

(36) Kang, B. K.; Han, G. S.; Baek, J. H.; Lee, D. G.; Song, Y. H.; Kwon, S. Bin; Cho, I. S.; Jung, H. S.; Yoon, D. H. Nanodome Structured BiVO 4 /GaO x N 1− x Photoanode for Solar Water Oxidation. *Adv. Mater. Interfaces* **2017**, *4*, 1700323.

(37) Steier, L.; Herraiz-Cardona, I.; Gimenez, S.; Fabregat-Santiago, F.; Bisquert, J.;

Tilley, S. D.; Grätzel, M. Understanding the Role of Underlayers and Overlayers in Thin Film Hematite Photoanodes. *Adv. Funct. Mater.* **2014**, *24*, 7681–7688.

(38) Hisatomi, T.; Brillet, J.; Cornuz, M.; Le Formal, F.; Tétreault, N.; Sivula, K.; Grätzel, M. A Ga 2 O 3 Underlayer as an Isomorphic Template for Ultrathin Hematite Films toward Efficient Photoelectrochemical Water Splitting. *Faraday Discuss.* **2012**, *155*, 223–232.

(39) Prévot, M. S.; Li, Y.; Guijarro, N.; Sivula, K. Improving Charge Collection with Delafossite Photocathodes: A Host–guest CuAlO2/CuFeO2 Approach. *J. Mater. Chem. A* **2016**, *4*, 3018–3026.

(40) Bärtsch, M.; Sarnowska, M.; Krysiak, O.; Willa, C.; Huber, C.; Pillatsch, L.; Reinhard, S.; Niederberger, M. Multicomposite Nanostructured Hematite–Titania Photoanodes with Improved Oxygen Evolution: The Role of the Oxygen Evolution Catalyst. *ACS Omega* **2017**, *2*, 4531–4539.

(41) Murcia-López, S.; Fàbrega, C.; Monllor-Satoca, D.; Hernández-Alonso, M. D.; Penelas-Pérez, G.; Morata, A.; Morante, J. R.; Andreu, T. Tailoring Multilayered BiVO 4 Photoanodes by Pulsed Laser Deposition for Water Splitting. *ACS Appl. Mater. Interfaces* **2016**, *8*, 4076–4085.

(42) Stefik, M.; Cornuz, M.; Mathews, N.; Hisatomi, T.; Mhaisalkar, S.; Grätzel, M. Transparent, Conducting Nb:SnO2 for Host–Guest Photoelectrochemistry. *Nano Lett.* **2012**, *12*, 5431–5435.

(43) Elam, J. W.; Baker, D. A.; Hryn, A. J.; Martinson, A. B. F.; Pellin, M. J.; Hupp, J. T. Atomic Layer Deposition of Tin Oxide Films Using Tetrakis(Dimethylamino) Tin. *J. Vac. Sci. Technol. A Vacuum, Surfaces, Film.* **2008**, *26*, 244.

(44) Kykyneshi, R.; Zeng, J.; Cann, D. P. Transparent Conducting Oxides Based on Tin Oxide. In *Handbook of Transparent Conductors*; Springer US: Boston, MA, 2011; Vol. 22, pp. 171–191.

(45) Aboaf, J. A.; Marcotte, V. C.; Chou, N. J. Chemical Composition and Electrical Properties of Tin Oxide Films Prepared by Vapor Deposition. *J. Electrochem. Soc.* **1973**, *120*, 701.

(46) Mullings, M. N.; Hägglund, C.; Bent, S. F. Tin Oxide Atomic Layer Deposition from Tetrakis(Dimethylamino)Tin and Water. *J. Vac. Sci. Technol. A Vacuum, Surfaces, Film.* **2013**, *31*, 061503.

(47) Dotan, H.; Sivula, K.; Grätzel, M.; Rothschild, A.; Warren, S. C. Probing the Photoelectrochemical Properties of Hematite (α-Fe_2O_3) Electrodes Using Hydrogen Peroxide as a Hole Scavenger. *Energy Environ. Sci.* **2011**, *4*, 958–964.

(48) Zhong, D. K.; Choi, S.; Gamelin, D. R. Near-Complete Suppression of Surface Recombination in Solar Photoelectrolysis by " Co-Pi " Catalyst-Modified W : BiVO 4. *J. Am. Chem. Soc.* **2011**, *133*, 18370–18377.

(49) Batzill, M.; Diebold, U. The Surface and Materials Science of Tin Oxide. *Prog. Surf. Sci.* **2005**, *79*, 47–154.

(50) Davazoglou, D. Optical Properties of SnO2 Thin Films Grown by Atmospheric Pressure Chemical Vapour Deposition Oxiding SnCl4. *Thin Solid Films* **1997**, *302*, 204–213.

(51) Spence, W. The Uv Absorption Edge of Tin Oxide Thin Films. *J. Appl. Phys.* **1967**, *38*, 3767–3770.

(52) Wan, C. F.; McGrath, R. D.; Keenan, W. F.; Tung, Y. S.; Frank, S. N. Doping Tin-

Oxide Films by Ion Implantation. *J. Electrochem. Soc.* **1988**, *135*, 985.

(53) McDonald, K. J.; Choi, K.-S. A New Electrochemical Synthesis Route for a BiOI Electrode and Its Conversion to a Highly Efficient Porous BiVO4 Photoanode for Solar Water Oxidation. *Energy Environ. Sci.* **2012**, *5*, 8553.

(54) Lee, D. K.; Choi, K.-S. Enhancing Long-Term Photostability of BiVO4 Photoanodes for Solar Water Splitting by Tuning Electrolyte Composition. *Nat. Energy* **2018**, *3*, 53–60.

(55) Govindaraju, G. V.; Wheeler, G. P.; Lee, D.; Choi, K.-S. Methods for Electrochemical Synthesis and Photoelectrochemical Characterization for Photoelectrodes. *Chem. Mater.* **2017**, *29*, 355–370.

(56) Kim, T. W.; Ping, Y.; Galli, G. A.; Choi, K.-S. Simultaneous Enhancements in Photon Absorption and Charge Transport of Bismuth Vanadate Photoanodes for Solar Water Splitting. *Nat. Commun.* **2015**, *6*, 8769.

(57) Li, Z.; Luo, W.; Zhang, M.; Feng, J.; Zou, Z. Photoelectrochemical Cells for Solar Hydrogen Production: Current State of Promising Photoelectrodes, Methods to Improve Their Properties, and Outlook. *Energy Environ. Sci.* **2013**, *6*, 347–370.

(58) Tan, H. L.; Amal, R.; Ng, Y. H. Alternative Strategies in Improving the Photocatalytic and Photoelectrochemical Activities of Visible Light-Driven $BiVO_4$: A Review. *J. Mater. Chem. A* **2017**, *5*, 16498–16521.

(59) Park, Y.; McDonald, K. J.; Choi, K.-S. Progress in Bismuth Vanadate Photoanodes for Use in Solar Water Oxidation. *Chem. Soc. Rev.* **2013**, *42*, 2321–2337.

(60) Liu, R.; Lin, Y.; Chou, L.-Y.; Sheehan, S. W.; He, W.; Zhang, F.; Hou, H. J. M.; Wang, D. Water Splitting by Tungsten Oxide Prepared by Atomic Layer Deposition

and Decorated with an Oxygen-Evolving Catalyst. *Angew. Chemie Int. Ed.* **2011**, *50*, 499–502.

(61) Gao, Y.; Zandi, O.; Hamann, T. W. Atomic Layer Stack Deposition-Annealing Synthesis of CuWO 4. *J. Mater. Chem. A* **2016**, *4*, 2826–2830.

(62) Lin, Y.; Zhou, S.; Sheehan, S. W.; Wang, D. Nanonet-Based Hematite Heteronanostructures for Efficient Solar Water Splitting. *J. Am. Chem. Soc.* **2011**, *133*, 2398–2401.

(63) Hajibabaei, H.; Zandi, O.; Hamann, T. W. Tantalum Nitride Films Integrated with Transparent Conductive Oxide Substrates via Atomic Layer Deposition for Photoelectrochemical Water Splitting. *Chem. Sci.* **2016**, *7*, 6760–6767.

(64) Steier, L.; Luo, J.; Schreier, M.; Mayer, M. T.; Sajavaara, T.; Grätzel, M. Low-Temperature Atomic Layer Deposition of Crystalline and Photoactive Ultrathin Hematite Films for Solar Water Splitting. *ACS Nano* **2015**, *9*, 11775–11783.

(65) Law, M.; Greene, L. E.; Johnson, J. C.; Saykally, R.; Yang, P. Nanowire Dye-Sensitized Solar Cells. *Nat. Mater.* **2005**, *4*, 455–459.

(66) Greene, L. E.; Law, M.; Tan, D. H.; Montano, M.; Goldberger, J.; Somorjai, G.; Yang, P. General Route to Vertical ZnO Nanowire Arrays Using Textured ZnO Seeds. *Nano Lett.* **2005**, *5*, 1231–1236.

(67) Seaman, C. H. Calibration of Solar Cells by the Reference Cell Method—The Spectral Mismatch Problem. *Sol. Energy* **1982**, *29*, 291–298.

(68) Toma, F. M.; Cooper, J. K.; Kunzelmann, V.; McDowell, M. T.; Yu, J.; Larson, D. M.; Borys, N. J.; Abelyan, C.; Beeman, J. W.; Yu, K. M.; *et al.* Mechanistic Insights into Chemical and Photochemical Transformations of Bismuth Vanadate

Photoanodes. *Nat. Commun.* **2016**, *7*, 12012.

(69) Kim, T. W.; Choi, K.-S. Improving Stability and Photoelectrochemical Performance of BiVO 4 Photoanodes in Basic Media by Adding a ZnFe 2 O 4 Layer. *J. Phys. Chem. Lett.* **2016**, *7*, 447–451.

CHAPTER 4:
PERSISTENT MICELLE TEMPLATES FOR TUNABLE POROUS CARBONS

Abstract

Porous carbon materials offer a flexible platform, with applications in filtration, catalysis, and microelectronics. Tuning important feature sizes of these materials (e.g. pore size, wall thickness) is important for applications where multiple transport pathways are active (e.g. solute diffusion in electrolyte, charge transport through material), such as supercapacitors. Persistent micelle templates (PMT) have proven useful in the independent tuning of nanometer-scale features such as wall thickness and pore size. To date, PMT has maintained kinetic control of polymer chain exchange through the solvent, via the Flory-Huggins χ parameter. Here, PMT is applied for the first time with carbon materials where phase partitioning dramatically changes solvent conditions, resulting a low-water content organic phase without sufficient χ barrier towards chain exchange. A new kinetic barrier was advanced based upon chain mobility by using block polymer micelles with a glassy core.

Introduction

Porous carbon materials have long been utilized for a variety of applications, from filtration to catalyst supports to electronic devices.[1] To date, porous carbons have primarily been synthesized through direct carbonization, ice templates, hard templates, and soft templates.[2–4] Of the templating methods, soft templates offer the simplest route for synthesis of mesoporous carbons, offering tight control over pore sizes and not requiring hazardous etching steps.[1]

Synthesis of porous carbon materials has benefitted from block copolymer (BCP) templating; however, much of the work on carbon-BCP templates has been restricted to using Pluronics as the structure directing agent,[5–7] limiting the pore sizes accessible from soft templates. Pluronics are widely available and very affordable, though the low

molecular weight of the hydrophobic poly(propylene oxide) block (~3.7 kg mol^{-1}) limits the final pore size to ~6 nm.[7] Additionally, while larger BCPs (such as PEO-*b*-PMMA and PEO-*b*-PS) give access to larger pore sizes,[8,9] especially in combination with secondary techniques like freeze drying or ice templating,[10] the tuning of material (e.g. phenolic resin) and template at a minimum alters wall thickness and pore size simultaneously due to changes in the microphase separation equilibrium,[11–16] while more drastic changes to template architecture have been noted in the literature – for example, transitions from randomly packed spheres to lamellae.[7]

Persistent micelle templates, a self-assembly technique developed by the Stefik group, prevents the equilibrium-driven rearrangement of polymers during self-assembly by creating a kinetic barrier to polymer chain transfer.[17,18] To date, this barrier has been imposed by the solvent conditions of the system, where a static or mildly agitated solution does not induce polymer chain exchange. However, chain exchange can be selectively permitted by providing more energy to the system, typically in the form of sonication.[18] PMT has proven useful in creating fully tunable metal oxide materials, where wall thickness and pore size can be controlled independently.[19] Material tunability allows for simultaneous optimization of orthogonal properties such as solute diffusion rates and conductivity. Carbon persistent micelle templates (CPMT) are designed to expand the advantages achieved with PMT of metal oxides by substituting the material templated from a metal oxide (e.g. TiO_2, SnO_2, Nb_2O_5, etc.) for phenolic resins.

Phenolic resins are synthesized via polycondensation of a phenolic derivative (phenol, resorcinol, or phloroglucinol, with one, two, or three substituent alcohols) and a bridging agent, typically formaldehyde.[6] This reaction is easily run in a variety of solvents (e.g.

alcohols, THF, acetone),[5,20,21] and is typically catalyzed under basic or acidic conditions.[22–24] Resorcinol-formaldehyde (RF) resins are attractive for the increased rate of reaction compared to phenol-formaldehyde resins as well as access to a facilely tunable crosslinking chemistry.[6,23] The presence of multiple alcohol groups on resorcinol activates three sites for hydroxymethylation (eq 2 in Scheme 4.1), leading to three potential bridging sites per resorcinol.

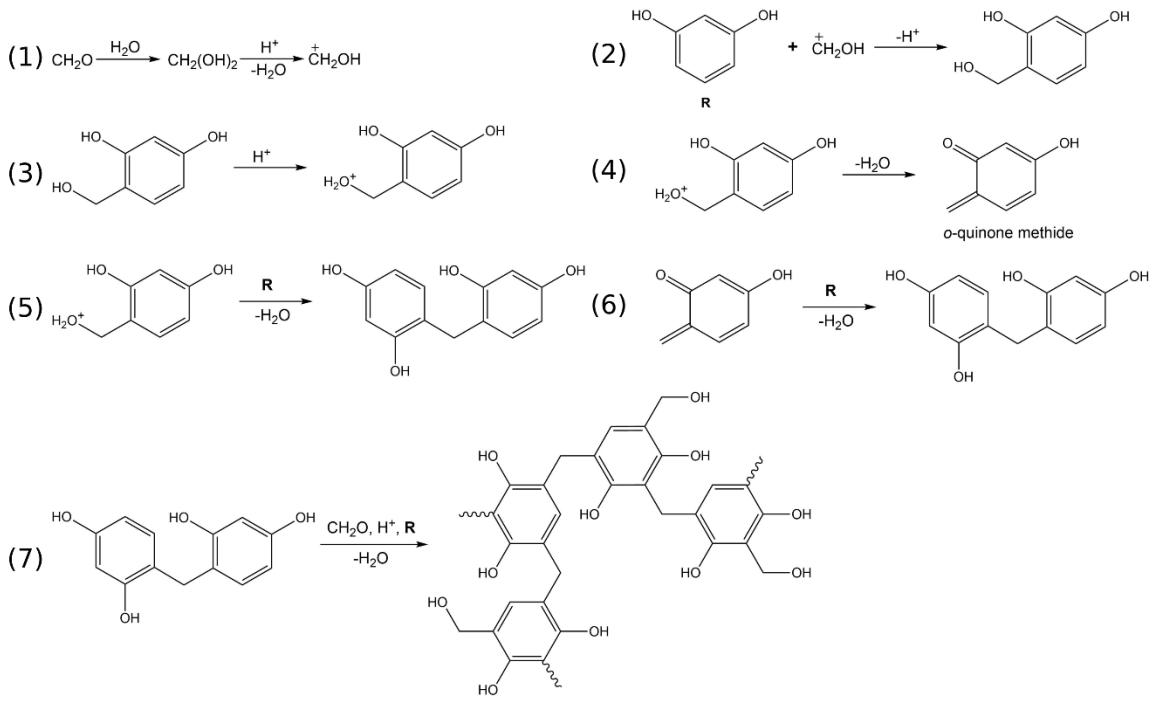

Scheme 4.1. A proposed mechanism for RF gel formation under acid catalysis. Reproduced with permission from Ref 12.

Results and Discussion

CPMT with PEO-*b*-PHA

Thin films

Thin films of this series, using PEO-*b*-PHA as a templating agent and methanol as the primary solvent, were useful in establishing appropriate conditions for RF resin synthesis. Primarily, these conditions are the aging conditions, resorcinol to formaldehyde mole ratio (R:F), and resorcinol to catalyst (HCl) mole ratio (R:C).

The summary of the simplest results is as follows: adjusting the R:F mole ratio from 1:1 to 1:3 controls the extent of crosslinking within the resin from one bridging functionality to a fully crosslinked RF system, while higher ratios (e.g. 1:6) affect the rate of reaction via the Le Chatlier's principle; adjusting the R:C mole ratio is used to affect the rate of reaction but will also affect the water content minimum. For methanol-based samples templated with PEO-*b*-PHA, the R:C ratio is held with majority resorcinol (RC values of 8 or 4).

It was quickly observed that thin films – particularly from spin coating – age quickly, becoming visibly pink within 25 min of aging at high catalyst loadings (Figure 4.1). The development of color in RF resins is a useful indicator for the extent of reaction, where the presence of the color indicates the presence of o-quinone methide intermediates.[23]

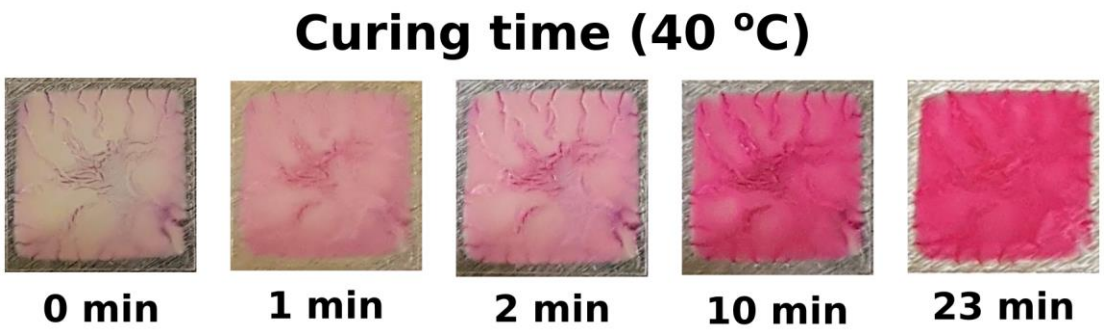

Figure 4.1. RF reaction progression with curing time at 40 °C in air. Sample CM01.

Structure control with PEO-*b*-PHA was minimal at best, where changes to equilibrium polymer phase (e.g. transitions from randomly packed spheres to lamellae) suggest dynamic chain exchange; however, the extent of reaction prior to casting (via spin coating, dip coating, etc.)[25] – designated "gel time" – and the water content were identified as significant parameters. From SAXS results (Figure 4.2), it was observed that relatively high water contents (10 wt%) and gel times of ~25 min produced the highest-order

structures. While the SAXS patterns are consistent with lamellae, instead of the desired persistent micelles, these water contents and gel times should still be relevant when casting solutions templated with glassy micelles (*vide infra*). Tested conditions that had little to no observed effect on structure include the curing time (in a humidity chamber) and dipping the spin coated film in acid prior to aging (Figure D.1).

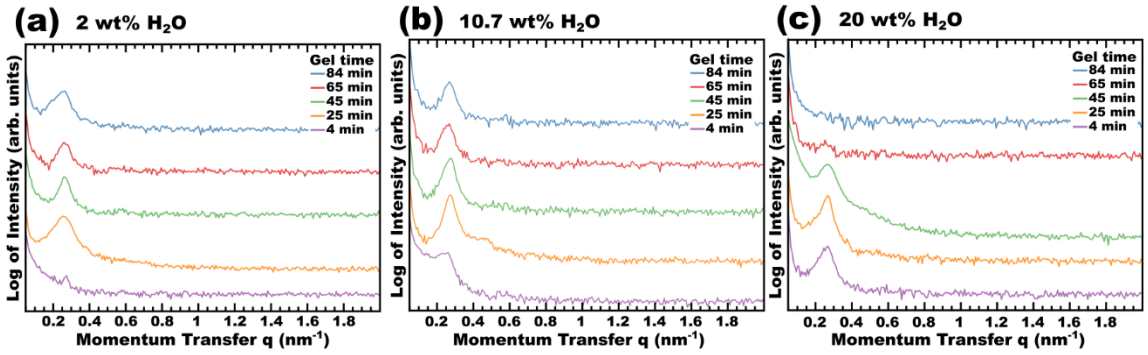

Figure 4.2. Effect of water content and gel time on RF resin organization.

Freeze-dried

Freeze drying was only trialed for two samples, both using butanol as the primary solvent. The motivation for using freeze drying as a secondary templating technique comes from research by the Giannelis group, where freeze drying resins templated with silica as a hard template in a butanol/water mixture produced hierarchical porous structures, resulting in mixed pore sizes of ~10 and ~2 nm were observed. The smaller pores were formed by the templating agent while the larger pores were induced by material displacement from ice crystals.[10]

Both freeze dried samples tested failed to achieve the desired results, and from SAXS appear to have become dynamic (Figure 4.3a). In the first sample, the failure seems to have been from an insufficiently high thermal gradient, as extensive sample loss occurred during freeze drying where the sample had been frozen in a dry ice bath with isopropanol. For the

second sample, insufficient time was given for RF polycondensation (that is, too little gel time) prior to freezing and vacuum drying (Figure 4.3b,c).

As freeze-drying was unsuccessful in both instances, this synthetic route was abandoned while the recipe was improved to prevent polymer rearrangement.

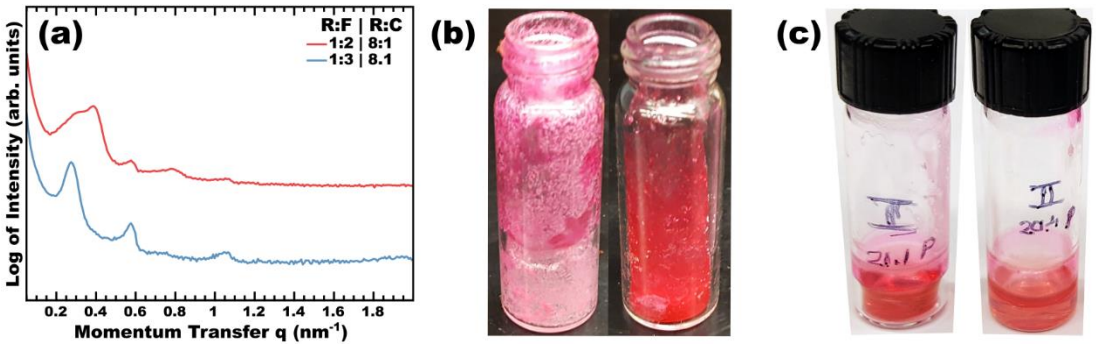

Figure 4.3. (a) SAXS of CB01, with a R:F mole ratio of 1:2 or 1:3; images of freeze dried CB01 (b) and CB02 (c) with RF 1:2 left and 1.3 right. Samples CB01 (a,b) and CB02 (c).

Phase-separation

As described in the previous subsection, freeze-drying of RF resins proved difficult to achieve, given the variety of variables at play. As it was identified that the resin templates were becoming dynamic (instead of persistent micelles), focus was turned to templating the resin to a fully crosslinked solid prior to solvent removal via freeze drying. Parameters tested include gel time, water content, and temperature during gelling. From the SAXS results corresponding to gel time and temperature (Figure 4.4a) and high water contents (Figure 4.4b), bulk carbon templates with PEO-*b*-PHA are consistently dynamic.

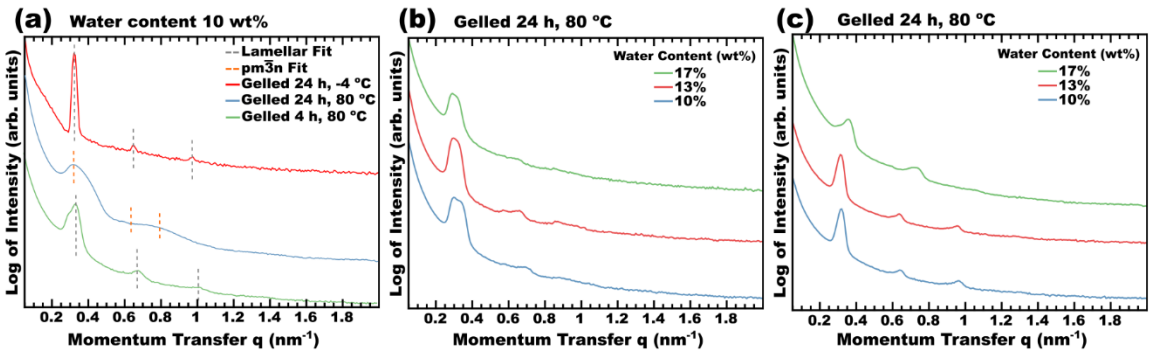

Figure 4.4. SAXS of phase-separation resins *versus* gel time and temperature (a), and water content at (b) 80 °C or (c) 60 °C. Samples CB15 (a) and CB18 (b,c).

Dynamic polymer templating can be easily identified by two methods, both of which are accessible by SEM: (1) changes to the pore size or (2) transition of the polymer architecture from, for example, spherical micelles to lamellae. Such a transition as the latter case was observed for samples of MT 0.4 and 3.0, at 10 wt% H_2O, RF 1:3, and R:C 4:1.

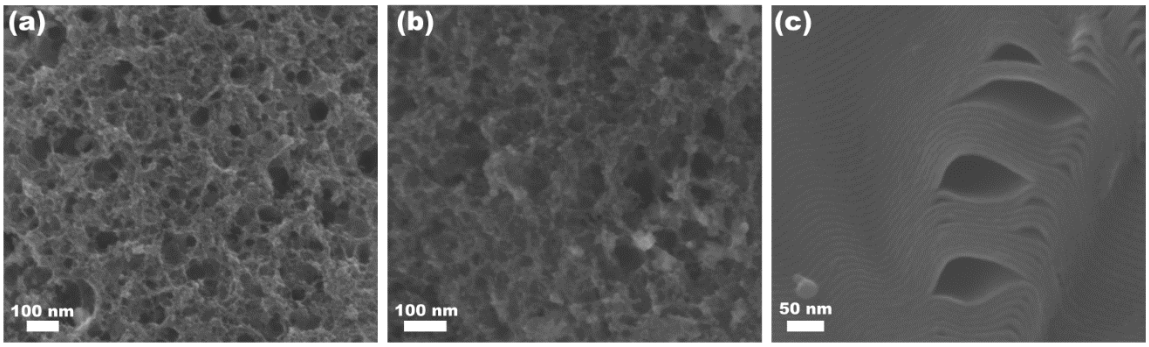

Figure 4.5. SEM of carbonized RF resins from freeze drying. M:T ratios of (a) 0.4, (b) 1.0, and (c) 2.4. Samples from CB08.

Summary

The initial trials with CPMT using PEO-*b*-PHA yielded interesting results, showing the importance of basic parameters like the mole ratios of resorcinol to formaldehyde and HCl, as well as the new parameter (gel time). However, it is obvious that some fundamental characteristic of RF resins is incompatible with PMT in its current configuration and requires an adaptation of the technique to prevent dynamic micelle transitions.

Following the observation, both here and in the literature, that extended gel times result in phase separation of the solvent and resin, it is hypothesized that the rate of polymer rearrangement is higher than the rate of resin polycondensation, regardless of reaction temperature. Because of the solvent phase separation, the solvent itself cannot be the handle to induce a kinetic barrier on polymer rearrangement. Further work (*vide infra*) will substitute the soft PEO-*b*-PHA templating agent with a copolymer containing a glassy core block (either PMMA or PS).

CPMT with PEO-*b*-PMMA

From the results described above using PEO-*b*-PHA as a templating agent, efforts with PEO-*b*-PMMA started with a focus on the parameters identified as most significant – i.e. RF, RC, and water content.

To disperse the polymer, the polymer was first micellized using a solvent exchange method described in the Experimental Methods section.[26] The recovered polymer micelles were soluble in methanol with slight heating (40 ^{o}C), with a mean particle hydrodynamic radius of 20 nm by DLS in a 96/4 wt% methanol-water solution (Figure D.2), down from 50 nm in pure, dry methanol.

Here, regardless of water content, R:C mole ratio, and aging temperature, reproducibility of structures (dynamic or otherwise) could not be achieved.

Problems with reproducibility in the PEO-b-PMMA system were initially suspected to stem from the interactions between the two blocks – i.e. PEO and PMMA. As has been shown previously in the literature, PEO and PMMA can intermix.[9] This intermixing can result in material crossover from the corona to the core. Further reading in the literature has suggested an alternative route for the loss of persistence due to solubility of PEO-*b*-PMMA in alcohol-water mixtures. As observed by Hoogenboom, *et al.*,[27] PS-*b*-PMMA

can be dissolved into an 80/20 mixture of ethanol and water, where this solvent ratio was shown to achieve a high loading of PMMA. If it is the case that PMMA is plasticized by water-alcohol mixtures, then this copolymer would be expected to suffer similar obstacles with templating as PEO-*b*-PHA. Additionally, PMMA solubility was also noted as dependent on the specific alcohol-water ratio used, which might be part of the problem observed with changing M:T ratios – as the increase in M:T requires an increase in formaldehyde present, and consequently water content.

CPMT with PEO-*b*-PS

Polystyrene is well known to be insoluble in alcohols and will thus remain glassy in solution as a copolymer with PEO. However, this very benefit is itself an obstacle to forming micelle templates. The problem arises in how to disperse PEO-*b*-PS in a nonsolvent for PS, and especially how to control the dispersity of the micelle population once the polymer is dispersed.

Polymer dispersion was first attempted by replicated the solvent exchange method used for PEO-*b*-PMMA; however, there were consistently both solubility and reproducibility problems using this method (dissolving polymer into THF and adding water dropwise, followed by collection via rotary evaporation). This solvent exchange technique was adjusted by several methods, including changing the addition order (e.g. THF into water), changing the pH of the water solution (substituting DI water for 3, 5, or 12 M HCl), substituting THF for acetone, and the addition rate of either water or HCl to the THF/polymer solution. The size of particles in solution was tracked by DLS throughout this process and consistently resulted in >1 μm-sized particles in solution. Importantly, it was confirmed that the polymer formed unimers in THF and aggregated in THF/water mixtures (Figure 4.6), demonstrating that micellization (and eventually aggregation) of

PEO-*b*-PS does occur in THF/H_2O mixtures and suggesting that this solvent system is still viable for formation of glassy persistent micelles. From these results, it is suspected that the presence of THF in the solvent mixture was plasticizing the PS cores, allowing for core-core aggregation and the observed micron-size particles.

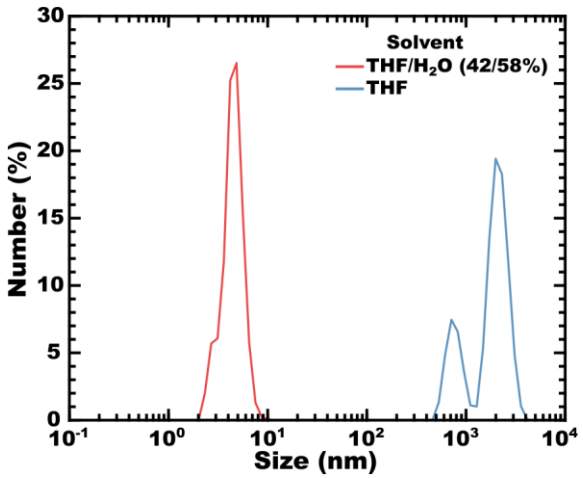

Figure 4.6. DLS of PEO-*b*-PS in THF and THF/H_2O.

To form glassy-core micelles while minimizing THF content in solution, the solvent exchange process was adapted to the method described by Skrabania, *et al.*[28] Briefly, polymer in a low boiling good solvent (THF) is added to a hot, high boiling bad solvent (90 ^oC water) dropwise. Enough time is given between drops to fully remove the good solvent (typically 8-10 s). Anecdotally, an audible popping can be heard when adding THF to water above 86 ^oC. As before, the hydrodynamic radius of particles in solution was tracked by DLS with polymer addition. As can be seen in Figure 4.7, the number of large particles grows quickly as the polymer concentration increases. It is hypothesized that this particle growth stems from the concentration of the polymer in both THF and in the water bath. As a drop of THF/polymer interacts with hot water, the THF is first diluted by water, forcing the polymer into a poor solvent, before the THF is boiled off. During this transition

from pure THF to pure water, the polymer unimers will be energetically driven to microphase separate from solution and will do so by forming micelles with other unimers from the THF drop (in the dilute water bath case) or will interact with particles already formed in water. Here, if the concentration of polymer particles in water is high enough, particles in water would be expected to increase in size as more polymer is included. Additionally, the dispersity of the particle sizes in pure water as the concentration of polymer in THF increases. Therefore, preforming micelles should be beneficial, and for a couple reasons: (1) avoiding the particle selection lottery described above, which lead to polymer particle growth in water, and (2) allowing for micelle dispersity control via sonication prior to impeding chain transfer by changing the cores from soft to glassy.

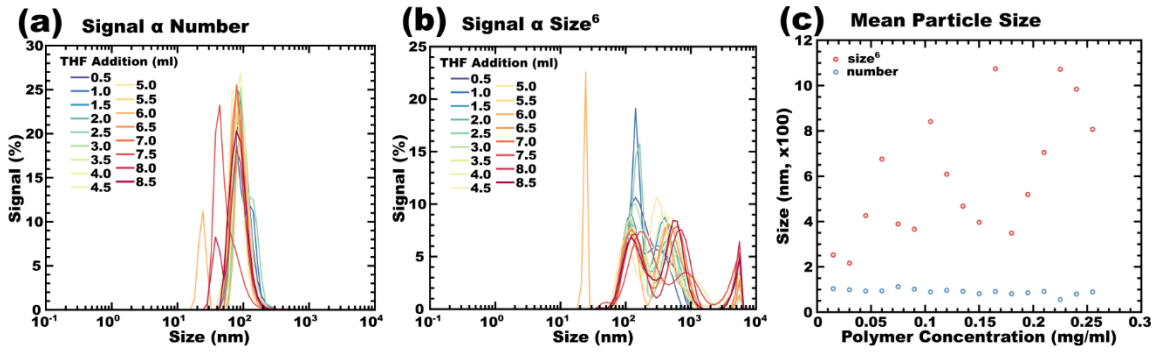

Figure 4.7. Hydrodynamic radius of particles with increasing polymer concentration during addition of THF to hot water. (a) Normalized *vs.* particle number, (b) normalized *vs.* (particle size)^6, and (c) mean particle size *vs.* polymer concentration.

Micelles preformed in a THF/4 wt% H_2O solution were added dropwise to hot water and micelle size was tracked by DLS with polymer concentration in water (Figure 4.8). Here it is observed that the micelle size remains much more consistent during polymer addition. This is seen in both the number-average data (Figure 4.8a), which is consistently around 100 nm, and size-weighted data (Figure 4.8b), where the particles are consistently a few hundred nanometers in hydrodynamic radius, and only a few large aggregates are

observed. Compare this with the previous tests using pure THF, where large aggregates at or above the detection limit become a significant contribution early in the measurements. Based on these results, the procedure for micellization seems best with a THF/4 wt% H_2O, where larger particles can be easily removed by filtration while preserving the bulk of the micelle population as ~100 nm particles. To improve the yield of polymer as free (non-aggregated) micelles, sonication of the final water solution should be tested.

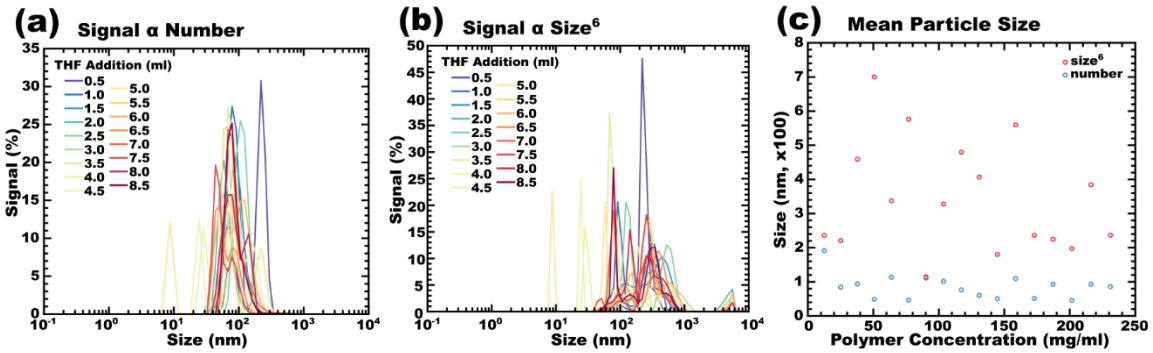

Figure 4.8. Hydrodynamic radius of particles with increasing polymer concentration during addition of THF/4 wt% H_2O to hot water. (a) Normalized *vs.* particle number, (b) normalized *vs.* (particle size)^6, and (c) mean particle size *vs.* polymer concentration.

Summary and Future Work

The development of carbon persistent micelle templating as revealed some drawbacks to the first generation of PMT processing, primarily defined by a fundamental dependence on solvent conditions. Here it was shown that with the removal of solvent in a soft system – either as a thin film or during phase separation processes – chain exchange is kinetically accessible for soft templating polymers, leading to dynamic micelles and equilibrium architecture transitions. To avoid this obstacle, PMT has been adapted to utilize copolymers containing a glassy hydrophobic block.

Once the process for creating glassy-core persistent micelles is finalized – establishing the processes for collection and utilization in templates – templating of carbon resins is

expected to proceed rapidly. Resin templates from bulk casting or thin films will be trialed first to establish effective gel times prior to curing or coating, followed by M:T weight ratio studies to track morphology changes (e.g. wall thickness).

To this point, the primary focus of this study was to extend the morphology tunability of PMT to porous carbon materials, depending on well-established chemistries for a carbon source – i.e. resorcinol-formaldehyde resins. However, the use of gaseous materials – HCl as catalyst and formaldehyde as reactant – represent a significant challenge to recipe flexibility when comparing thin films to bulk cast materials. Changing RF resin for a process that does not require gaseous components in solution would therefore be desirable. Phloroglucinol-glyoxylic acid (PG) resins are chemically similar to RF resins, except here glyoxylic acid functions as both crosslinking moiety and catalyst. It should also be noted that removing formaldehyde (a known carcinogen) has the additional benefit of making CPMT more attractive industrially, especially if less-toxic solvents can be utilized (e.g., ethanol or water in exchange of methanol).

Materials and Methods

All chemicals were acquired from commercial sources and used without further purification except where noted.

Morphology

A Zeiss Ultra Plus scanning electron microscope (SEM) was operated at 5 kV using an in-lens secondary electron detector to observe the film surface and cross-sectional acquisition.

Diffraction

X-ray diffraction experiments were conducted using a SAXSLab Ganesha at the South Carolina SAXS Collaborative. A Xenocs GeniX 3D microfocus source was used with a Cu target to generate a monochromatic beam with a 0.154 nm wavelength. The instrument was

calibrated using silicon powder (NIST 640d). Scattering data were processed from the scattering vector $q = 4\pi\lambda^{-1}\sin\theta$ where λ is the X-ray wavelength and 2θ is the total scattering angle. A Pilatus 300 K detector (Dectris) was used to collect the two-dimensional (2D) scattering patterns. Samples were measured with the beam at an incident angle of 8^{o} relative to the film plane. SAXSGUI software was used to radially integrate the 2D patterns to produce 1D profiles.

Polymer Characterization

All proton nuclear magnetic resonance (^{1}H NMR) spectra were recorded on a Bruker Avance III HD 300. NMR samples were prepared in deuterated chloroform ($CDCl_3$) as a concentration of ~1 wt%. Molecular weight (M_n) and molar mass dispersity (Đ) were determined using a Waters gel permeation chromatography (GCP) instrument equipped with a 515 HPLC pump, a 2410 refractive index detector, and three styragel columns (HR1, HR3, and HR4 in the effective molecular weight range of 0.1-5, 0.5-30, and 5-600 kg mol^{-1}, respectively). THF was used as the eluent at 30 ^{o}C at a flow rate of 1 ml min^{-1}. The GPC was calibrated with PS standards (2570, 1090, 579, 246, 130, 67.5, 34.8, 18.1, 10.4, 3.4, 1.6 kg mol^{-1}) obtained from Polymer Laboratories. GPC samples were prepared by dissolving the sample in THF at a concentration of 2.0 mg ml^{-1} and were filtered (0.2 um PTFE) prior to injection, unless noted otherwise. Dynamic light scattering measurements of micelle hydrodynamic diameter were measured using a Zetasizer Nanoseries ZEN3690 instrument.

Synthesis of PEO-*b*-PHA

The poly(ethylene oxide)-*b*-poly(hexyl acrylate), PEO-*b*-PHA, was synthesized by atom transfer radical polymerization (ATRP) using methods described elsewhere.[17,18]

Synthesis of PEO-*b*-PMMA

A poly(ethylene oxide)-*b*-poly(methyl methacrylate), PEO-b-PMMA, diblock copolymer was synthesized by a two-step synthesis starting from a Steglich esterification of poly(ethylene glycol)methyl ether to form a macroinitiator, followed by a neat atom transfer radical polymerization (ATRP) at 70 ˚C to grow the PMMA block. The procedure is described elsewhere in detail.[17] The molar mass of PMMA (M_n = 13.4 kg mol^{-1}) was determined by ^{1}H NMR by comparison to the known PEO macroinitiator (M_n = 5.0 kg mol^{-1}). The molar mass dispersity ($Đ_{PMMA}$ = 1.13) was characterized by GPC. GPC samples were prepared in THF at concentrations of 10 mg mL^{-1}, filtered through a 0.2 μm syringe filter prior to injection.

Synthesis of PEO-*b*-PS

The poly(ethylene oxide)-*b*-polystyrene, PEO-b-PS, was synthesized via activators regenerated by electron transfer for atom transfer radical polymerization (ARGET-ATRP).[29] The synthesis used the reagent ratio of [styrene] : [PEO-Br] : [Me_6TREN] : [Cu(II)] : [Sn(EH)] = 200 : 1 : 0.105 : 0.005 : 0.1. The reaction was run neat. The PEO-Br macroinitiator (5 kg mol^{-1}, 2.0 g) was dissolved in 9 ml of styrene monomer (filtered over alumina to remove inhibitor) and deaerated by three cycles of freezing in liquid nitrogen, pumping to <50 mtorr, and thawing. The catalyst and reducing agent with ligand (dissolved in toluene) were added during the last thaw cycle. The solution was stirred at room temperature for 30 min before initiating the polymerization by immersing the reaction vessel in a 90 ºC oil bath and stirred at 150 rpm for 20 h. The reaction mixture was cooled before exposing the solution to air. The crude polymerization solution was diluted with THF and precipitated into a 3-fold excess of cold methanol (-78 ºC using a dry ice bath). The collected polymer was dried on filter paper overnight. The molar mass of PS (M_n =

31.3 kg mol^{-1}) was determined by ^{1}H NMR by comparison to the known PEO macroinitiator (M_n = 5.0 kg mol^{-1}). The molar mass dispersity ($Đ_{PS}$ = 1.12) was determined by GPC.

CPMT with PEO-*b*-PHA

When using PEO-*b*-PHA as the templating agent, RF resins were synthesized using two solvent systems, using methanol (designated as samples CM00) or *tert*-butanol (designated as samples CB00). Primarily for this template series, CM series of samples were dried as thin films from spin coating, drop casting, or dip coating; while the CB series was either freeze-dried or synthesized via phase separation method.

For each sample, a two-part solution was created. The "template" solution combined polymer, solvent (i.e. methanol or butanol), and water; while the "material" solution contained resorcinol, solvent, water, and HCl. The water content for both solutions was held constant to ensure consistent water content regardless of M:T ratio for a given sample. The desired ratios of Template and Material solutions were combined; at this point, the sample solution is inert until formaldehyde is added. The addition of formaldehyde corresponds to the start of "gel time."

The details of the experiments highlighted within this chapter can be found in Appendix D.

CPMT with PEO-*b*-PMMA

Templating with PEO-*b*-PMMA followed a similar method as described above for PEO-*b*-PHA, with the most significant change relating to the polymer solubility. While PEO-*b*-PHA could be dissolved directly into methanol or butanol, PEO-*b*-PMMA was first micellized in water by solvent exchange (described later) and collected as a powder. This

micelle powder was dispersed in either dry methanol or dilute methanol-water solutions (e.g. 4 wt% water).

Polymer micelles were formed and collected via a solvent exchange method.[26] Briefly, ca. 50 mg of polymer was dissolved in 5 ml THF and added dropwise to stirring water (40 ml, 500 rpm) at room temperature. The THF/water solution was placed on a rotary evaporated and concentrated over the course of several hours. The rotary evaporator bath was heated no higher than 45 ^{o}C. Micellized polymer powder were transferred to a 20 ml vial for storage.

CPMT with PEO-*b*-PS

Micellization studies for PEO-b-PS followed either the method used for PEO-b-PMMA (described above) or an adapted method based on that described by Skrabania, *et al*.[28] Briefly, 50 mg of polymer is dissolved in 10 ml THF (anhydrous) and added dropwise to hot water while stirring (400 ml, 90 ^{o}C, 500 rpm). The follow-up test, using THF/4 wt% H_2O, followed the same general procedure: polymer was dissolved in anhydrous THF, sonicated 10 min. Water was added to give a 4 wt% solution and the solution was sonicated for an additional 10 min. This THF/H_2O/polymer solution was added dropwise to 90 ^{o}C H_2O while stirring at 600 rpm. The water content (4 wt%) was selected based on the average particle size in solution (Figure D.3).

Trials substituting, for example, room temperature water for 12 M HCl did so on a volumetric basis. The details of the experiments highlighted within this chapter can be found in Appendix D.

Acknowledgments

I would like to acknowledge Kayla Lantz for providing the PEO-*b*-PHA and PEO-*b*-PMMA polymers used in this study.

References

(1) Sakintuna, B.; Yürüm, Y. Templated Porous Carbons: A Review Article. *Ind. Eng. Chem. Res.* **2005**, *44*, 2893–2902.

(2) Tamon, H.; Ishizaka, H.; Yamamoto, T.; Suzuki, T. Preparation of Mesoporous Carbon by Freeze Drying. *Carbon N. Y.* **1999**, *37*, 2049–2055.

(3) Ryoo, R.; Joo, S. H.; Jun, S. Synthesis of Highly Ordered Carbon Molecular Sieves via Template-Mediated Structural Transformation. *J. Phys. Chem. B* **1999**, *103*, 7743–7746.

(4) Liang, C.; Hong, K.; Guiochon, G. A.; Mays, J. W.; Dai, S. Synthesis of a Large-Scale Highly Ordered Porous Carbon Film by Self-Assembly of Block Copolymers. *Angew. Chemie Int. Ed.* **2004**, *43*, 5785–5789.

(5) Meng, Y.; Gu, D.; Zhang, F.; Shi, Y.; Cheng, L.; Feng, D.; Wu, Z.; Chen, Z.; Wan, Y.; Stein, A.; *et al.* A Family of Highly Ordered Mesoporous Polymer Resin and Carbon Structures from Organic−Organic Self-Assembly. *Chem. Mater.* **2006**, *18*, 4447–4464.

(6) Liang, C.; Dai, S. Synthesis of Mesoporous Carbon Materials via Enhanced Hydrogen-Bonding Interaction. *J. Am. Chem. Soc.* **2006**, *128*, 5316–5317.

(7) Wang, X.; Liang, C.; Dai, S. Facile Synthesis of Ordered Mesoporous Carbons with High Thermal Stability by Self-Assembly of Resorcinol−Formaldehyde and Block Copolymers under Highly Acidic Conditions. *Langmuir* **2008**, *24*, 7500–7505.

(8) Deng, Y.; Liu, J.; Liu, C.; Gu, D.; Sun, Z.; Wei, J.; Zhang, J.; Zhang, L.; Tu, B.; Zhao, D. Ultra-Large-Pore Mesoporous Carbons Templated from Poly(Ethylene Oxide)- b -Polystyrene Diblock Copolymer by Adding Polystyrene Homopolymer as a Pore Expander. *Chem. Mater.* **2008**, *20*, 7281–7286.

(9) Deng, Y.; Liu, C.; Gu, D.; Yu, T.; Tu, B.; Zhao, D. Thick Wall Mesoporous Carbons with a Large Pore Structure Templated from a Weakly Hydrophobic PEO–PMMA Diblock Copolymer. *J. Mater. Chem.* **2008**, *18*, 91–97.

(10) Sahore, R.; Estevez, L. P.; Ramanujapuram, A.; DiSalvo, F. J.; Giannelis, E. P. High-Rate Lithium-Sulfur Batteries Enabled by Hierarchical Porous Carbons Synthesized via Ice Templation. *J. Power Sources* **2015**, *297*, 188–194.

(11) Segalman, R. A. Patterning with Block Copolymer Thin Films. *Mater. Sci. Eng. R Reports* **2005**, *48*, 191–226.

(12) Shelton, C. K.; Epps, T. H. Block Copolymer Thin Films: Characterizing Nanostructure Evolution with in Situ X-Ray and Neutron Scattering. *Polymer (Guildf).* **2016**, *105*, 545–561.

(13) Epps, III, T. H.; O'Reilly, R. K. Block Copolymers: Controlling Nanostructure to Generate Functional Materials – Synthesis, Characterization, and Engineering. *Chem. Sci.* **2016**, *7*, 1674–1689.

(14) Kim, S.; Bates, C. M.; Thio, A.; Cushen, J. D.; Ellison, C. J.; Willson, C. G.; Bates, F. S. Consequences of Surface Neutralization in Diblock Copolymer Thin Films. *ACS Nano* **2013**, *7*, 9905–9919.

(15) Fasolka, M. J.; Mayes, A. M. Block Copolymer Thin Films: Physics and Applications. *Annu. Rev. Mater. Res.* **2001**, *31*, 323–355.

(16) Albert, J. N. L.; Epps, T. H. Self-Assembly of Block Copolymer Thin Films. *Mater. Today* **2010**, *13*, 24–33.

(17) Sarkar, A.; Stefik, M. How to Make Persistent Micelle Templates in 24 Hours and Know It Using X-Ray Scattering. *J. Mater. Chem. A* **2017**, *5*, 11840–11853.

(18) Lantz, K. A.; Sarkar, A.; Littrell, K. C.; Li, T.; Hong, K.; Stefik, M. Cavitation Enables Switchable and Rapid Block Polymer Exchange under High-χ N Conditions. *Macromolecules* **2018**, *51*, 6967–6975.

(19) Lantz, K. A.; Clamp, N. B.; van den Bergh, W.; Sarkar, A.; Stefik, M. Full Gamut Wall Tunability from Persistent Micelle Templates via Ex Situ Hydrolysis. *Small* **2019**, *Accpeted*, 1900393.

(20) Kosonen, H.; Valkama, S.; Nykänen, A.; Toivanen, M.; Brinke, G. Ten; Ruokolainen, J.; Ikkala, O.; ten Brinke, G.; Ruokolainen, J.; Ikkala, O. Functional Porous Structures Based on the Pyrolysis of Cured Templates of Block Copolymer and Phenolic Resin. *Adv. Mater.* **2006**, *18*, 201–205.

(21) Herou, S.; Ribadeneyra, M. C.; Madhu, R.; Araullo-Peters, V.; Jensen, A.; Schlee, P.; Titirici, M. Ordered Mesoporous Carbons from Lignin: A New Class of Biobased Electrodes for Supercapacitors. *Green Chem.* **2019**, *21*, 550–559.

(22) Matei Ghimbeu, C.; Vidal, L.; Delmotte, L.; Le Meins, J.-M.; Vix-Guterl, C. Catalyst-Free Soft-Template Synthesis of Ordered Mesoporous Carbon Tailored Using Phloroglucinol/Glyoxylic Acid Environmentally Friendly Precursors. *Green Chem.* **2014**, *16*, 3079.

(23) Mulik, S.; Sotiriou-leventis, C.; Leventis, N. Time-Efficient Acid-Catalyzed Synthesis of Resorcinol−Formaldehyde Aerogels. *Chem. Mater.* **2007**, *19*, 6138–6144.

(24) Tanaka, S.; Nishiyama, N.; Egashira, Y.; Ueyama, K. Synthesis of Ordered Mesoporous Carbons with Channel Structure from an Organic–organic Nanocomposite. *Chem. Commun.* **2005**, 2125–2127.

(25) Mukai, S. R.; Nishihara, H.; Yoshida, T.; Taniguchi, K.; Tamon, H. Morphology of Resorcinol–formaldehyde Gels Obtained through Ice-Templating. *Carbon N. Y.* **2005**, *43*, 1563–1565.

(26) Wang, D.; Peng, Z.; Liu, X.; Tong, Z.; Wang, C.; Ren, B. Synthesis and Micelle Formation of Triblock Copolymers of Poly(Methyl Methacrylate)-b-Poly(Ethylene Oxide)-b-Poly(Methyl Methacrylate) in Aqueous Solution. *Eur. Polym. J.* **2007**, *43*, 2799–2808.

(27) Hoogenboom, R.; Becer, C. R.; Guerrero-Sanchez, C.; Hoeppener, S.; Schubert, U. S. Solubility and Thermoresponsiveness of PMMA in Alcohol-Water Solvent Mixtures. *Aust. J. Chem.* **2010**, *63*, 1173.

(28) Skrabania, K.; Laschewsky, A.; Berlepsch, H. V.; Böttcher, C. Synthesis and Micellar Self-Assembly of Ternary Hydrophilic−Lipophilic−Fluorophilic Block Copolymers with a Linear PEO Chain. *Langmuir* **2009**, *25*, 7594–7601.

(29) Jakubowski, W.; Kirci-Denizli, B.; Gil, R. R.; Matyjaszewski, K. Polystyrene with Improved Chain-End Functionality and Higher Molecular Weight by ARGET ATRP. *Macromol. Chem. Phys.* **2008**, *209*, 32–39.

CHAPTER 5:
SUMMARY AND SUGGESTIONS FOR FUTURE WORK

Summary

In the researches for the work presented herein, we have improved multiple techniques used to synthesize nanometer scale devices. One of the principle objectives of this dissertation was to develop a controlled deposition technique for $BiVO_4$ that is compatible with anodic semiconductor underlayers like SnO_2, with a secondary objective of demonstrating a heterojunction $SnO_2/BiVO_4$ photoanode on a high-aspect ratio substrate. A second principle objective was to expand the utility of a recently developed templating method (PMT) by controllably templating carbonaceous materials.

We have successfully developed the first ALD process for single-phase$BiVO_4$.[1] In developing said process we have also recognized the importance of controlling and treating defect chemistries specific to the synthetic method used in fabricating $BiVO_4$ photoanodes. To highlight the significance of this observation, we examined a body of literature that described a variety of postsynthetic treatments used to control the defect chemistries of $BiVO_4$ as synthesized by various methods (electrodeposition, spray pyrolysis, spin coating, etc).[2] Finally, ALD was used to grow SnO_2 and $BiVO_4$ on high-aspect ratio antimony-doped tin oxide nanotubes (ATO-NTs) to achieve space efficient heterojunction photoanodes for solar water splitting,[3] demonstrating for the first time the substrate-conformed synthesis of ultrathin $BiVO_4$ in conjunction with a hole-blocking underlayer.

We have also expanded the level of control achieved with PMT by utilizing glassy micelles for templates. This enables a higher tolerance to changing solvent conditions, expanding PMT utility to nonaqueous media and phase-separation reactions. This was also the first demonstration of PMT with carbonaceous materials. Porous carbons were utilized as super capacitors, and the effects of altering the wall thickness to pore size ratio were examined.

Suggestions for Future Work

Future works should be focused on expanding the versatility of CPMTs, ideally to realize a product with commercial appeal. The practicality in purely metal oxide or carbonaceous templates is self-evident and creating hybrid templates using carbon/metal oxide or carbon/nanoparticle would expand PMT into a wide range of catalysts of interest in a variety of fields, such as fuel cells, redox flow batteries, and waste management. To make these methods industrially appealing, the PMT process needs to use greener materials, avoiding carcinogens (e.g. formaldehyde, THF) and other acutely toxic materials (e.g. methanol); additionally, scalable methodologies need to be demonstrated. Combining these approaches – developing industrially-relevant conditions and demonstrating hybrid PMTs – would significantly increase the visibility of this unique nanomaterials technique.

Future development of ALD $BiVO_4$ should investigate the specifics of PEC activation, and especially should seek to improve the charge separation efficiency of ALD $BiVO_4$ to increase the aspect ratio of ultrathin $BiVO_4$-based photoanodes. This would realize the balance of charge separation with optical thickness. As highlighted in the Introduction, further improvements to charge separation efficiency should be guided by the defect chemistries present in a given synthetic route, incentivizing research in this direction – for example, *in situ* XPS for both the PEC and ALD processes.[4,5] Such research could observe the formation of defects in real time during $BiVO_4$ growth and their changes during solar water splitting. Tracking the defects within $BiVO_4$ could allow for the development of targeted treatments to remediate detrimental defects and the insertion of beneficial defects – e.g. nitrogenation, etc., as described in the Introduction. Finally, combining ultrathin, charge-separation efficient $BiVO_4$ with an efficient charge-injection catalyst, such as CoPi or FeOOH/NiOOH,[6,7] in conjunction with the presented SnO_2 heterojunction could

optimize the three primary pathways (photon absorption, charge separation, and charge injection) for this photocatalyst and would have the opportunity to achieve the highest reported efficiency for a $BiVO_4$-based photoanode.

Additionally, in the realm of carbon PMT, altering the doping of carbon can result in altered electrode characteristics – for example, nitrogenation for N-doped carbon, oxygenation by acids after carbonization, or templating in the presence of metals to introduce magnetic properties.[8] The flexibility of porous carbons leaves a lot of room for growth in this direction, where developments of this technology would result in increased group recognition and the potential for commercialization.

References

(1) Lamm, B.; Sarkar, A.; Stefik, M. Surface Functionalized Atomic Layer Deposition of Bismuth Vanadate for Single-Phase Scheelite. *J. Mater. Chem. A* **2017**, *5*, 6060–6069.

(2) Lamm, B.; Trześniewski, B. J.; Döscher, H.; Smith, W. A.; Stefik, M. Emerging Postsynthetic Improvements of BiVO 4 Photoanodes for Solar Water Splitting. *ACS Energy Lett.* **2018**, *3*, 112–124.

(3) Lamm, B.; Zhou, L.; Rao, P.; Stefik, M. Atomic Layer Deposition of Space-Efficient SnO 2 Underlayers for BiVO 4 Host-Guest Architectures for Photoassisted Water Splitting. *ChemSusChem* **2019**. DOI: 10.1002/cssc.201802566.

(4) Favaro, M.; Abdi, F. F.; Lamers, M.; Crumlin, E. J.; Liu, Z.; van de Krol, R.; Starr, D. E. Light-Induced Surface Reactions at the Bismuth Vanadate/Potassium Phosphate Interface. *J. Phys. Chem. B* **2018**, *122*, 801–809.

(5) Head, A. R.; Chaudhary, S.; Olivieri, G.; Bournel, F.; Andersen, J. N.; Rochet, F.; Gallet, J.-J.; Schnadt, J. Near Ambient Pressure X-Ray Photoelectron Spectroscopy

Study of the Atomic Layer Deposition of TiO 2 on RuO 2 (110). *J. Phys. Chem. C* **2016**, *120*, 243–251.

(6) Ma, Y.; Le Formal, F.; Kafizas, A.; Pendlebury, S. R.; Durrant, J. R. Efficient Suppression of Back Electron/Hole Recombination in Cobalt Phosphate Surface-Modified Undoped Bismuth Vanadate Photoanodes. *J. Mater. Chem. A* **2015**, *3*, 20649–20657.

(7) Kim, T. W.; Choi, K.-S. Nanoporous BiVO4 Photoanodes with Dual-Layer Oxygen Evolution Catalysts for Solar Water Splitting. *Science.* **2014**, *343*, 990–994.

(8) Libbrecht, W.; Verberckmoes, A.; Thybaut, J. W.; Van Der Voort, P.; De Clercq, J. Soft Templated Mesoporous Carbons: Tuning the Porosity for the Adsorption of Large Organic Pollutants. *Carbon N. Y.* **2017**, *116*, 528–546.

APPENDIX A:
PERMISSION TO REPRINT

Chapter 1 Permission

Chapter 2 Permission

From the publisher's webpage (emphasis added):

"If you are not the author of this article and you wish to reproduce material from it in a third-party non-RSC publication you must formally request permission using Copyright Clearance Center. Go to our Instructions for using Copyright Clearance Center page for details.

Authors contributing to RSC publications (journal articles, books or book chapters) do not need to formally request permission to reproduce material contained in this article provided that the correct acknowledgement is given with the reproduced material.

Reproduced material should be attributed as follows:

- For reproduction of material from NJC:Reproduced from Ref. XX with permission from the Centre National de la Recherche Scientifique (CNRS) and The Royal Society of Chemistry.
- For reproduction of material from PCCP: Reproduced from Ref. XX with permission from the PCCP Owner Societies.
- For reproduction of material from PPS: Reproduced from Ref. XX with permission from the European Society for Photobiology, the European Photochemistry Association, and The Royal Society of Chemistry.
- For reproduction of material from all other RSC journals and books: Reproduced from Ref. XX with permission from The Royal Society of Chemistry.

If the material has been adapted instead of reproduced from the original RSC publication "Reproduced from" can be substituted with "Adapted from".

In all cases the Ref. XX is the XXth reference in the list of references.

If you are the author of this article you do not need to formally request permission to reproduce figures, diagrams etc. contained in this article in third party publications or in a thesis or dissertation provided that the correct acknowledgement is given with the reproduced material.

Reproduced material should be attributed as follows:

- For reproduction of material from NJC: [Original citation] - Reproduced by permission of The Royal Society of Chemistry (RSC) on behalf of the Centre National de la Recherche Scientifique (CNRS) and the RSC
- For reproduction of material from PCCP: [Original citation] - Reproduced by permission of the PCCP Owner Societies
- For reproduction of material from PPS: [Original citation] - Reproduced by permission of The Royal Society of Chemistry (RSC) on behalf of the European Society for Photobiology, the European Photochemistry Association, and RSC
- For reproduction of material from all other RSC journals: [Original citation] - Reproduced by permission of The Royal Society of Chemistry

If you are the author of this article you still need to obtain permission to reproduce the whole article in a third-party publication **with the exception of reproduction of the whole article in a thesis or dissertation.**

Information about reproducing material from RSC articles with different licences is available on our Permission Requests page.

Chapter 3 Permission

JOHN WILEY AND SONS LICENSE TERMS AND CONDITIONS

Mar 28, 2019

This Agreement between Mr. Benjamin Lamm ("You") and John Wiley and Sons ("John Wiley and Sons") consists of your license details and the terms and conditions provided by John Wiley and Sons and Copyright Clearance Center.

License Number	4557830447309
License date	Mar 28, 2019
Licensed Content Publisher	John Wiley and Sons
Licensed Content Publication	ChemSusChem
Licensed Content Title	Atomic Layer Deposition of Space-Efficient SnO2 Underlayers for BiVO4 Host–Guest Architectures for Photoassisted Water Splitting
Licensed Content Author	Benjamin Lamm, Lite Zhou, Pratap Rao, et al
Licensed Content Date	Jan 22, 2019
Licensed Content Volume	0
Licensed Content Issue	0
Licensed Content Pages	10
Type of Use	Dissertation/Thesis
Requestor type	Author of this Wiley article
Format	Print and electronic
Portion	Full article
Will you be translating?	No
Title of your thesis / dissertation	Nanoscale Control of Metal Oxide and Carbonaceous Functional Materials
Expected completion date	May 2019
Expected size (number of pages)	140
Requestor Location	Mr. Benjamin Lamm 541 Main St Rm 223 COLUMBIA, SC 29201 United States Attn: Mr. Benjamin Lamm
Publisher Tax ID	EU826007151
Total	**0.00 USD**
Terms and Conditions	

TERMS AND CONDITIONS

This copyrighted material is owned by or exclusively licensed to John Wiley & Sons, Inc. or one of its group companies (each a"Wiley Company") or handled on behalf of a society with which a Wiley Company has exclusive publishing rights in relation to a particular work (collectively "WILEY"). By clicking "accept" in connection with completing this licensing transaction, you agree that the following terms and conditions apply to this transaction (along with the billing and payment terms and conditions established by the Copyright Clearance Center Inc., ("CCC's Billing and Payment terms and conditions"), at the time that you opened your RightsLink account (these are available at any time at http://myaccount.copyright.com).

Terms and Conditions

- The materials you have requested permission to reproduce or reuse (the "Wiley Materials") are protected by copyright.

- You are hereby granted a personal, non-exclusive, non-sub licensable (on a stand-alone basis), non-transferable, worldwide, limited license to reproduce the Wiley Materials for the purpose specified in the licensing process. This license, **and any CONTENT (PDF or image file) purchased as part of your order,** is for a one-time use only and limited to any maximum distribution number specified in the license. The first instance of republication or reuse granted by this license must be completed within two years of the date of the grant of this license (although copies prepared before the end date may be distributed thereafter). The Wiley Materials shall not be used in any other manner or for any other purpose, beyond what is granted in the license. Permission is granted subject to an appropriate acknowledgement given to the author, title of the material/book/journal and the publisher. You shall also duplicate the copyright notice that appears in the Wiley publication in your use of the Wiley Material. Permission is also granted on the understanding that nowhere in the text is a previously published source acknowledged for all or part of this Wiley Material. Any third party content is expressly excluded from this permission.

- With respect to the Wiley Materials, all rights are reserved. Except as expressly granted by the terms of the license, no part of the Wiley Materials may be copied, modified, adapted (except for minor reformatting required by the new Publication), translated, reproduced, transferred or distributed, in any form or by any means, and no derivative works may be made based on the Wiley Materials without the prior permission of the respective copyright owner.**For STM Signatory Publishers clearing permission under the terms of the STM Permissions Guidelines only, the terms of the license are extended to include subsequent editions and for editions in other languages, provided such editions are for the work as a whole in situ and does not involve the separate exploitation of the permitted figures or extracts,** You may not alter, remove or suppress in any manner any copyright, trademark or other notices displayed by the Wiley Materials. You may not license, rent, sell, loan, lease, pledge, offer as security, transfer or assign the Wiley Materials on a stand-alone basis, or any of the rights granted to you hereunder to any other person.

- The Wiley Materials and all of the intellectual property rights therein shall at all times remain the exclusive property of John Wiley & Sons Inc, the Wiley Companies, or their respective licensors, and your interest therein is only that of having possession of and the right to reproduce the Wiley Materials pursuant to Section 2 herein during the continuance of this Agreement. You agree that you own no right, title or interest in or to the Wiley Materials or any of the intellectual property rights therein. You shall have no rights hereunder other than the license as provided for above in Section 2. No right, license or interest to any trademark, trade name, service mark or other branding ("Marks") of WILEY or its licensors is granted hereunder, and you agree that you shall not assert any such right, license or interest with respect thereto

- NEITHER WILEY NOR ITS LICENSORS MAKES ANY WARRANTY OR REPRESENTATION OF ANY KIND TO YOU OR ANY THIRD PARTY, EXPRESS, IMPLIED OR STATUTORY, WITH RESPECT TO THE MATERIALS OR THE ACCURACY OF ANY INFORMATION CONTAINED IN THE MATERIALS, INCLUDING, WITHOUT LIMITATION, ANY IMPLIED WARRANTY OF MERCHANTABILITY, ACCURACY, SATISFACTORY QUALITY, FITNESS FOR A PARTICULAR PURPOSE, USABILITY, INTEGRATION OR NON-INFRINGEMENT AND ALL SUCH WARRANTIES ARE HEREBY EXCLUDED BY WILEY AND ITS LICENSORS AND WAIVED BY YOU.

- WILEY shall have the right to terminate this Agreement immediately upon breach of this Agreement by you.

- You shall indemnify, defend and hold harmless WILEY, its Licensors and their respective directors, officers, agents and employees, from and against any actual or threatened claims, demands, causes of action or proceedings arising from any breach of this Agreement by you.

- IN NO EVENT SHALL WILEY OR ITS LICENSORS BE LIABLE TO YOU OR ANY OTHER PARTY OR ANY OTHER PERSON OR ENTITY FOR ANY SPECIAL, CONSEQUENTIAL, INCIDENTAL, INDIRECT, EXEMPLARY OR PUNITIVE DAMAGES, HOWEVER CAUSED, ARISING OUT OF OR IN CONNECTION WITH THE DOWNLOADING, PROVISIONING, VIEWING OR USE OF THE MATERIALS REGARDLESS OF THE FORM OF ACTION, WHETHER FOR BREACH OF CONTRACT, BREACH OF WARRANTY, TORT, NEGLIGENCE, INFRINGEMENT OR OTHERWISE (INCLUDING, WITHOUT LIMITATION, DAMAGES BASED ON LOSS OF PROFITS, DATA, FILES, USE, BUSINESS OPPORTUNITY OR CLAIMS OF THIRD PARTIES), AND WHETHER OR NOT THE PARTY HAS BEEN ADVISED OF THE POSSIBILITY OF SUCH DAMAGES. THIS LIMITATION SHALL APPLY NOTWITHSTANDING ANY FAILURE OF ESSENTIAL PURPOSE OF ANY LIMITED REMEDY PROVIDED HEREIN.

- Should any provision of this Agreement be held by a court of competent jurisdiction to be illegal, invalid, or unenforceable, that provision shall be deemed amended to achieve as nearly as possible the same economic effect as the original provision, and the legality, validity and enforceability of the remaining provisions of this Agreement shall not be affected or impaired thereby.

- The failure of either party to enforce any term or condition of this Agreement shall not constitute a waiver of either party's right to enforce each and every term and condition of this Agreement. No breach under this agreement shall be deemed waived or

excused by either party unless such waiver or consent is in writing signed by the party granting such waiver or consent. The waiver by or consent of a party to a breach of any provision of this Agreement shall not operate or be construed as a waiver of or consent to any other or subsequent breach by such other party.

- This Agreement may not be assigned (including by operation of law or otherwise) by you without WILEY's prior written consent.
- Any fee required for this permission shall be non-refundable after thirty (30) days from receipt by the CCC.
- These terms and conditions together with CCC's Billing and Payment terms and conditions (which are incorporated herein) form the entire agreement between you and WILEY concerning this licensing transaction and (in the absence of fraud) supersedes all prior agreements and representations of the parties, oral or written. This Agreement may not be amended except in writing signed by both parties. This Agreement shall be binding upon and inure to the benefit of the parties' successors, legal representatives, and authorized assigns.
- In the event of any conflict between your obligations established by these terms and conditions and those established by CCC's Billing and Payment terms and conditions, these terms and conditions shall prevail.
- WILEY expressly reserves all rights not specifically granted in the combination of (i) the license details provided by you and accepted in the course of this licensing transaction, (ii) these terms and conditions and (iii) CCC's Billing and Payment terms and conditions.
- This Agreement will be void if the Type of Use, Format, Circulation, or Requestor Type was misrepresented during the licensing process.
- This Agreement shall be governed by and construed in accordance with the laws of the State of New York, USA, without regards to such state's conflict of law rules. Any legal action, suit or proceeding arising out of or relating to these Terms and Conditions or the breach thereof shall be instituted in a court of competent jurisdiction in New York County in the State of New York in the United States of America and each party hereby consents and submits to the personal jurisdiction of such court, waives any objection to venue in such court and consents to service of process by registered or certified mail, return receipt requested, at the last known address of such party.

WILEY OPEN ACCESS TERMS AND CONDITIONS

Wiley Publishes Open Access Articles in fully Open Access Journals and in Subscription journals offering Online Open. Although most of the fully Open Access journals publish open access articles under the terms of the Creative Commons Attribution (CC BY) License only, the subscription journals and a few of the Open Access Journals offer a choice of Creative Commons Licenses. The license type is clearly identified on the article.

The Creative Commons Attribution License

The Creative Commons Attribution License (CC-BY) allows users to copy, distribute and transmit an article, adapt the article and make commercial use of the article. The CC-BY license permits commercial and non-

Creative Commons Attribution Non-Commercial License

The Creative Commons Attribution Non-Commercial (CC-BY-NC)License permits use, distribution and reproduction in any medium, provided the original work is properly cited and is not used for commercial purposes.(see below)

Creative Commons Attribution-Non-Commercial-NoDerivs License

The Creative Commons Attribution Non-Commercial-NoDerivs License (CC-BY-NC-ND) permits use, distribution and reproduction in any medium, provided the original work is properly cited, is not used for commercial purposes and no modifications or adaptations are made. (see below)

Use by commercial "for-profit" organizations

Use of Wiley Open Access articles for commercial, promotional, or marketing purposes requires further explicit permission from Wiley and will be subject to a fee.

Further details can be found on Wiley Online Library http://olabout.wiley.com/WileyCDA/Section/id-410895.html

APPENDIX B:
SUPPLEMENTAL INFORMATION TO CHAPTER 2

Estimation of Host-Guest Architecture Needed for Efficient Light Harvesting

Host-guest architectures allow the decoupling of optical absorption from carrier transport. Here we consider the characteristics needed for a host-guest architecture based upon 30 nm SF-ALD $BiVO_4$ films. Within the 2.4 eV bandgap of $BiVO_4$,[1–3] the AM 1.5 spectrum has the most photon flux near the band-edge at 510 nm. Considering a target of 90% light harvesting efficiency at the 510 nm band edge, the corresponding optical thickness may be calculated using Equation B.1:

$$A = \alpha l \tag{B.1}$$

where A, α, and *l* are the absorbance, attenuation coefficient, and optical thickness of the film. The attenuation of a 30 nm film may thus be used to calculate the optical thickness needed for 90% light harvesting via the attenuation coefficient. Here the absorbance was calculated from the measured absorptance value using Equation B.2:

$$A = -\log\left(1 - \frac{A_{\%}}{100}\right) \tag{B.2}$$

where $A_{\%}$ is the absorptance as a percentage. The attenuation coefficient of the 30 nm MeOH-SF-ALD film was thus calculated to be 0.001433 nm^{-1}(at λ=510 nm). This attenuation coefficient was thus used to calculate that 90% absorptance would occur with an optical thickness of 697 nm. This value provides considerable insight into the design of host-guest architectures with efficient light harvesting. For example, assuming all layers are normal to the incident light, this optical thickness corresponds to a roughness factor of (697 nm)/(30 nm)=23.2. In other words, 23.2 such 30 nm layers would be needed to reach the described light harvesting target.

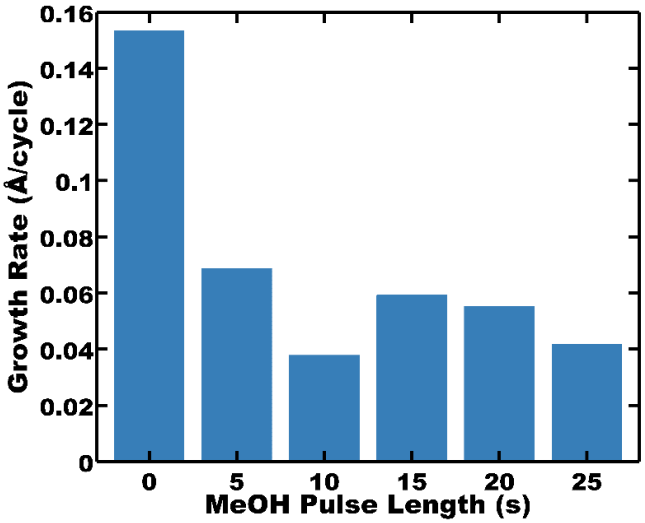

Figure B.1 The MeOH pulse length was optimized to saturate the inhibition of V_2O_5 growth using a pulse sequence of $[MeOH\text{-}VTIP\text{-}W]_x$.

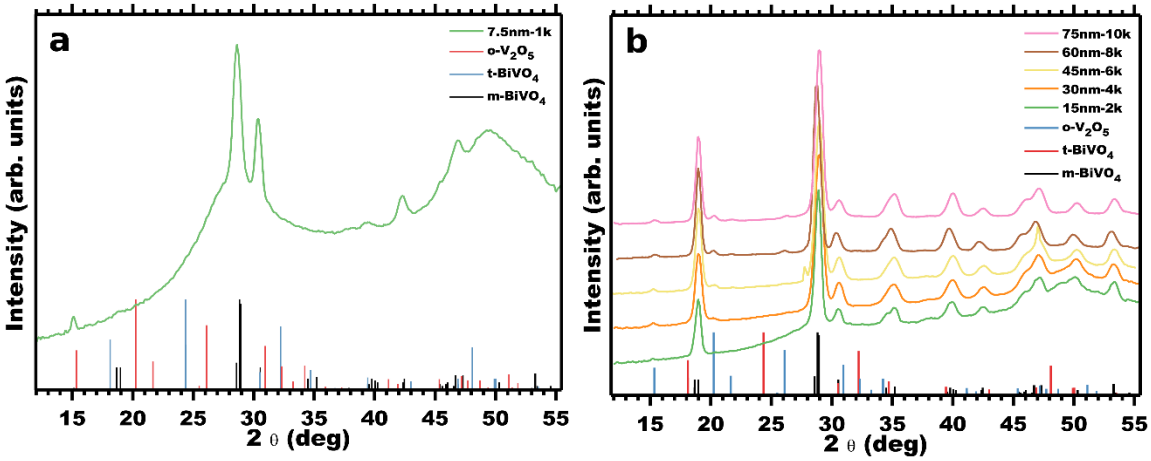

Figure B.2 GIWAXS of calcined MeOH-BVO films of 7.5 (a) and 15-75 nm (b) thickness. Sample descriptions in Table 2.4.

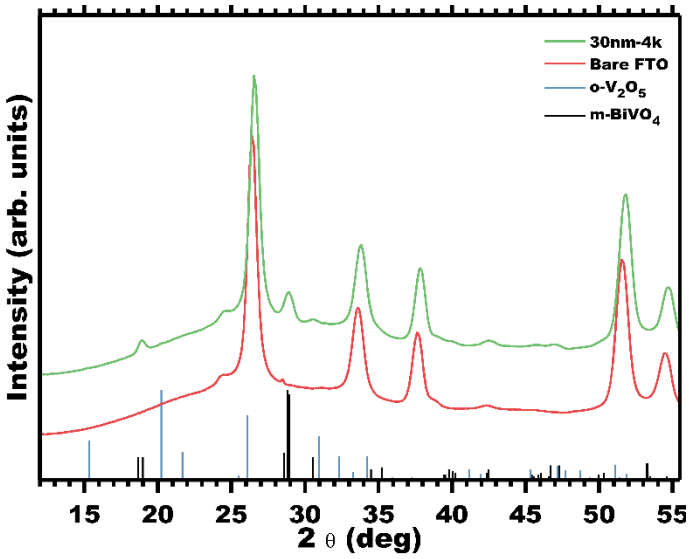

Figure B.3 GI-WAXS of bare FTO and FTO/$BiVO_4$ (30 nm, calcined MeOH-BVO where x=4,000 cycles).

Table B.1 Comparison of mean front-side photocurrent at 0.6 V vs RHE ($J_{J\text{-}V}$) to photocurrent calculated from IPCE (J_{IPCE}). Data is from calcined SF-BVO films. Samples are the same as those described in Table 2.4. J_{IPCE} was determined by multiplying IPCE (%) by the AM 1.5 spectrum ($mA/cm^2/nm$) before integrating over wavelength (nm).

Sample Name	$J_{J\text{-}V}$ (mA/cm^2)	J_{IPCE} (mA/cm^2)	Percent Difference
7.5nm-1k	0.010±0.002	0.003±0.001	63.9
15nm-2k	0.075±0.005	0.026±0.005	64.6
22.5nm-3k	0.11±0.01	0.043±0.007	62.4
30nm-4k	0.35±0.01	0.20±0.02	44.4
45nm-6k	0.31±0.02	0.18±0.03	42.2
60nm-8k	0.46±0.02	0.33±0.03	29.4
75nm-10k	0.57±0.03	0.66±0.03	15.2

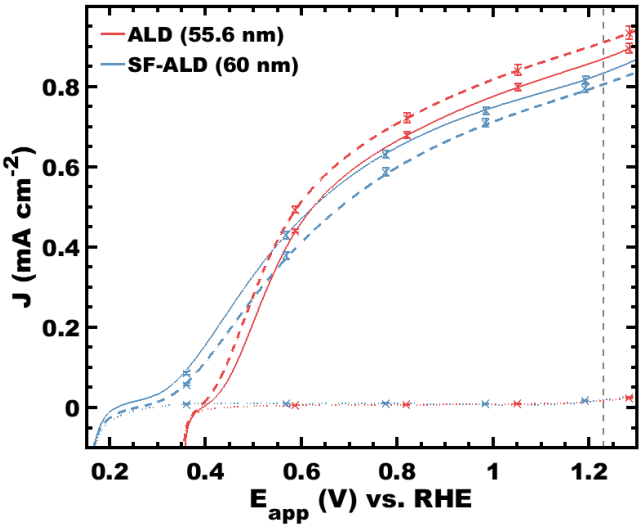

Figure B.4 The photocurrent performance of bismuth vanadate films prepared by conventional ALD and SF-ALD were compared under simulated AM 1.5 illumination. The conventional ALD procedure is identical to the SF-ALD procedure sans alcohol surface functionalization. The conventional ALD samples were 55.6 nm thick and were calcined at 450 °C for 1 hr and etched in 1 M NaOH to remove excess V_2O_5. The comparable SF-ALD samples were denoted at **60nm-8k** in the text.

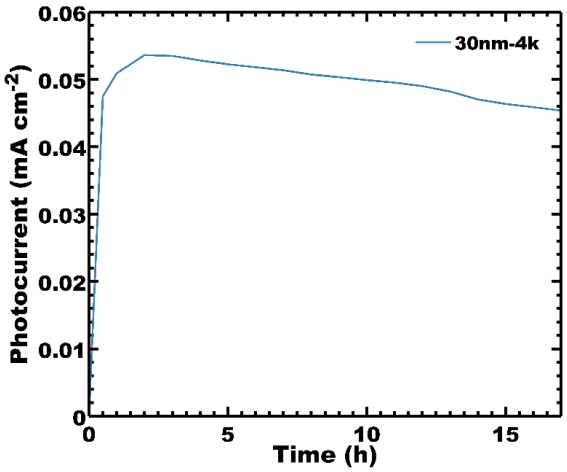

Figure B.5 Chronoamperometry of SF-ALD film 30nm-4k over 17hrs of continuous simulated AM 1.5 illumination at an applied potential of 0.6 V vs RHE. The electrolyte was 1.0 M potassium borate with a pH of 9.36 with 0.2 M Na_2SO_3 as hole scavenger.

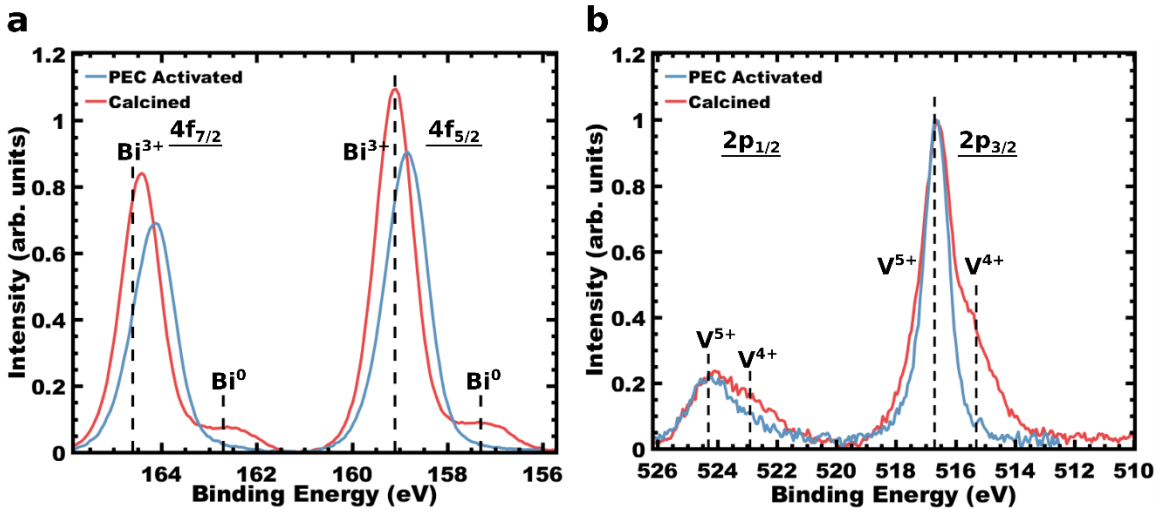

Figure B.6. XPS of calcined and PEC activated 30nm-4k films, showing regions for (a) Bi 4f and (b) V 2p.

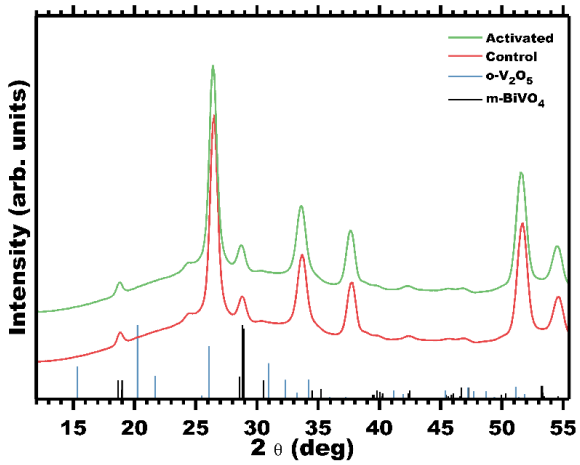

Figure B.7. GI-WAXS measurements on calcined 30 nm MeOH-BVO films without and with the photoelectrochemical activation. **Control** and **Activated** samples are the same as those described in Table 2.6.

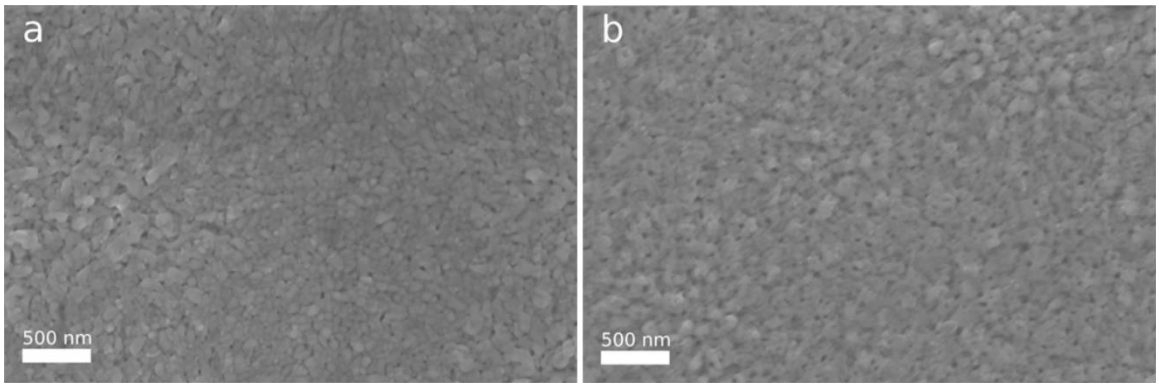

Figure B.8. Comparison of surface structure (a) before and (b) after photoelectrochemical activation. Images were acquired on calcined 30 nm MeOH-BVO films deposited on FTO.

Table B.2. All parameters used in the MeOH-SF-ALD deposition.

Step	Label	Device Index	Device Name	Action	Value	Branch
1		28	Pump		0	
2		9	EXPO_Heater	Set_to_On	0	
3		8	MFC_Flow	Set_to_Value	200	
4		1	VTIP Heater	Set_to_Value	45	
5		2	BiPh3 Heater	Set_to_Value	130	
6		4	Metal Precursor Manifold	Set_to_Value	130	
7		5	Oxidant Manifold	Set_to_Value	130	
8		7	Chamber_Door_Heat	Set_to_Value	130	
9		6	Chamber_Heat	Set_to_Value	130	
10		6	Chamber_Heat	Wait_Until_Set_Point_+/-	1	
11		22	Delay_(Sec.)		7200	
12	**DepoLoop**	22	Delay_(Sec.)		0.1	
13	**VLoop**	8	MFC_Flow	Set_to_Value	40	
14		8	MFC_Flow	Wait_Until_<	45	
15		10	EXPO_Actuator	Set_to_Closed	0	
16		22	Delay_(Sec.)		0.2	
17	MeOH	18	ALD_7_Actuator	Pulse_(mSec.)	25	
18		22	Delay_(Sec.)		1	
19		10	EXPO_Actuator	Set_to_Open	0	
20		8	MFC_Flow	Set_to_Value	200	
21		22	Delay_(Sec.)		10	
22		8	MFC_Flow	Set_to_Value	5	
23		8	MFC_Flow	Wait_Until_<	6	
24		22	Delay_(Sec.)		7	
25		10	EXPO_Actuator	Set_to_Closed	0	
26		22	Delay_(Sec.)		0.2	
27	VTIP	13	ALD_2_Actuator	Pulse_(mSec.)	2000	
28		22	Delay_(Sec.)		1	
29		10	EXPO_Actuator	Set_to_Open	0	
30		8	MFC_Flow	Set_to_Value	200	
31		22	Delay_(Sec.)		10	
32		8	MFC_Flow	Set_to_Value	40	
33		8	MFC_Flow	Wait_Until_<	45	

34		10	EXPO_Actuator	Set_to_Closed	0	
35		22	Delay_(Sec.)		0.2	
36	water	16	ALD_5_Actuator	Pulse_(mSec.)	25	
37		22	Delay_(Sec.)		1	
38		10	EXPO_Actuator	Set_to_Open	0	
39		8	MFC_Flow	Set_to_Value	200	
40		22	Delay_(Sec.)		10	
41		24	Loop_n_Times	Number	1	**VLoop**
42	**BiLoop**	8	MFC_Flow	Set_to_Value	40	
43		8	MFC_Flow	Wait_Until_<	45	
44		11	N2_Inject		0	
45		10	EXPO_Actuator	Set_to_Closed	0	
46		22	Delay_(Sec.)		0.2	
47	BiPH3	14	ALD_3_Actuator	Pulse_(mSec.)	2000	
48		22	Delay_(Sec.)		1	
49		10	EXPO_Actuator	Set_to_Open	0	
50		8	MFC_Flow	Set_to_Value	200	
51		22	Delay_(Sec.)		10	
52		8	MFC_Flow	Set_to_Value	40	
53		8	MFC_Flow	Wait_Until_<	45	
54		10	EXPO_Actuator	Set_to_Closed	0	
55		22	Delay_(Sec.)		0.2	
56	water	16	ALD_5_Actuator	Pulse_(mSec.)	25	
57		22	Delay_(Sec.)		1	
58		10	EXPO_Actuator	Set_to_Open	0	
59		8	MFC_Flow	Set_to_Value	200	
60		22	Delay_(Sec.)		10	
61		24	Loop_n_Times	Number	1	**BiLoop**
62		24	Loop_n_Times	Number	3000	**DepoLoop**
63		22	Delay_(Sec.)		3600	
64		8	MFC_Flow	Set_to_Value	5	

APPENDIX C:
SUPPLEMENTAL INFORMATION TO CHAPTER 3

Table C.1 Comparison of electrical properties for SnO_2 from different synthetic methods.

Method	Precursors	Conductivity (σ); [Scm^{-1}]	Mobility (μ); [$cm^2V^{-1}s^{-1}$]	Carrier concentration; [# cm^{-3}]
Spray pyrolysis[1]	$SnCl_4$, air	25	4	3.3×10^{19}
Spray pyrolysis[2]	$SnCl_4$, air	87	6.1	8.8×10^{21}
CVD (at 450 °C)[3]	$SnCl_4$, H_2O	142	9.6	9.1×10^{19}
CVD (at 450 °C)[4]	$SnCl_4$, air	18	--	--
ALD[5]	TDMASn, O_3	2.9	2.8	6.8×10^{18}
ALD[6]	TDMASn, O_3	3.6	--	--
ALD (this work)	TDMASn, O_3	2.4×10^{-4}	0.229	7.7×10^{15}

Applied-bias photon-to-charge efficiency (ABPE)

ABPE was calculated using:

$$\mathrm{ABPE}(\%) = \left[\frac{J_{photo}(\mathrm{mA\ cm^{-2}}) \times (E_{rc} - E_{app})(\mathrm{V})}{P_{photo}(\mathrm{mW\ cm^{-2}})}\right]_{\mathrm{AM\ 1.5G}} \times 100 \qquad \text{(C1)}$$

where J_{photo} is the measured photocurrent at a given applied potential (E_{app}), P_{photo} is the power density of AM 1.5G (100 mW cm^{-2}). E_{rc} corresponds to the cell potential of the redox couple, in this case 1.23 V_{RHE} for water splitting.

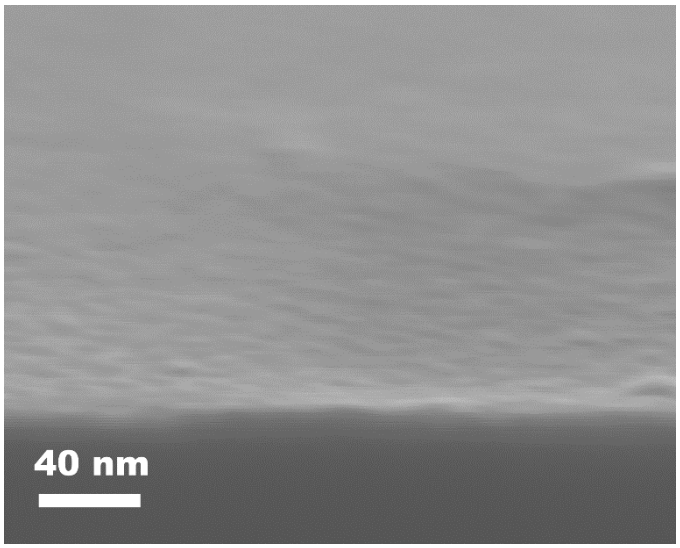

Figure C.1. SEM micrograph of conformal 2 nm SnO_2 on a Si wafer following heat treatment, at 8° tilt relative to the probe.

Roughness factor and Optical thickness calculations

Roughness factor (R_f) is the ratio of total surface area to the projected substrate area. The R_f for cylindrical nanotubes on a flat substrate can be calculated using:

$$R_f = h\pi d\rho + 1 \tag{C2}$$

where *h* and *d* correspond to the height and diameter of nanotubes, and ρ represents the areal tube density. In this study, ρ was found to be 10.44 nanotubes μm^{-2} based on SEM measurements.

The optical thickness, *l*, includes the increase in optical absorptance when thin absorber layers of thickness *n* are deposited on a 3D host with roughness factor >1. Ignoring diffusive scattering, the optical thickness of samples in this study were estimated using the total volume of $BiVO_4$ calculated from simple geometric considerations:

$$l = V_{BVO,cyl} \cdot \rho + n \tag{C3}$$

where

$$V_{BVO,cyl} = h\pi\left(R^2 - r^2\right) \tag{C4}$$

and where *R* corresponds to the combined host-guest nanotube radius and *r* corresponds to the host-only nanotube radius.

Table C.2 ALD of SnO_2 with TDMASn and O_3

Step	Label	Device Index	Device Name	Action	Value	Branch
1		28	Pump		0	
2		9	EXPO_Heater	Set_to_On	0	
3		8	MFC_Flow	Set_to_Value	200	
4		0	Precursor_1_Heat	Set_to_Value	55	
5		4	Manifold_1_Heat	Set_to_Value	100	
6		5	Manifold_2_Heat	Set_to_Value	130	
7		7	Chamber_Door_Heat	Set_to_Value	115	
8		6	Chamber_Heat	Set_to_Value	115	
9		6	Chamber_Heat	Wait_Until_Set_Point_+/-	1	
10	**clean**	17	ALD_6_Actuator	Pulse_(mSec.)	100	

11		22	Delay_(Sec.)		10	
12		24	Loop_n_Times	Number	100	**clean**
13		22	Delay_(Sec.)		1200	
14	**loopA**	8	MFC_Flow	Set_to_Value	5	
15		8	MFC_Flow	Wait_Until_<	6	
16		22	Delay_(Sec.)		7	
17		10	EXPO_Actuator	Set_to_Closed	0	
18		22	Delay_(Sec.)		0.2	
19	SNDMA	12	ALD_1_Actuator	Pulse_(mSec.)	1500	
20		22	Delay_(Sec.)		1	
21		10	EXPO_Actuator	Set_to_Open	0	
22		8	MFC_Flow	Set_to_Value	200	
23		22	Delay_(Sec.)		10	
24		8	MFC_Flow	Set_to_Value	40	
25		8	MFC_Flow	Wait_Until_<	45	
26		10	EXPO_Actuator	Set_to_Closed	0	
27		22	Delay_(Sec.)		0.2	
28	ozone	17	ALD_6_Actuator	Pulse_(mSec.)	100	
29		22	Delay_(Sec.)		1	
30		10	EXPO_Actuator	Set_to_Open	0	
31		8	MFC_Flow	Set_to_Value	200	
32		22	Delay_(Sec.)		10	
33		24	Loop_n_Times	Number	120	**loopA**
34		22	Delay_(Sec.)		10	
35		8	MFC_Flow	Set_to_Value	5	

Table C.3 SF-ALD of $BiVO_4$

Step	Label	Device Index	Device Name	Action	Value	Branch
1		28	Pump		0	
2		9	EXPO_Heater	Set_to_On	0	
3		1	Precursor_2_Heat	Set_to_Value	45	
4		2	Precursor_3_Heat	Set_to_Value	130	
5		4	Manifold_1_Heat	Set_to_Value	130	
6		5	Manifold_2_Heat	Set_to_Value	130	
7		7	Chamber_Door_Heat	Set_to_Value	130	
8		6	Chamber_Heat	Set_to_Value	130	
9		6	Chamber_Heat	Wait_Until_Set_Point_+/-	1	
10		8	MFC_Flow	Set_to_Value	200	
11		22	Delay_(Sec.)		7200	
12	**DepoLoop**	22	Delay_(Sec.)		0.1	
13	**VLoop**	8	MFC_Flow	Set_to_Value	40	
14		8	MFC_Flow	Wait_Until_<	45	
15		10	EXPO_Actuator	Set_to_Closed	0	
16		22	Delay_(Sec.)		0.2	
17	MeOH	18	ALD_7_Actuator	Pulse_(mSec.)	50	
18		22	Delay_(Sec.)		2	
19		10	EXPO_Actuator	Set_to_Open	0	
20		8	MFC_Flow	Set_to_Value	200	
21		22	Delay_(Sec.)		10	

22		8	MFC_Flow	Set_to_Value	5	
23		8	MFC_Flow	Wait_Until_<	6	
24		22	Delay_(Sec.)		7	
25		10	EXPO_Actuator	Set_to_Closed	0	
26		22	Delay_(Sec.)		0.2	
27	VTIP	13	ALD_2_Actuator	Pulse_(mSec.)	2000	
28		22	Delay_(Sec.)		1	
29		10	EXPO_Actuator	Set_to_Open	0	
30		8	MFC_Flow	Set_to_Value	200	
31		22	Delay_(Sec.)		10	
32		8	MFC_Flow	Set_to_Value	40	
33		8	MFC_Flow	Wait_Until_<	45	
34		10	EXPO_Actuator	Set_to_Closed	0	
35		22	Delay_(Sec.)		0.2	
36	water	16	ALD_5_Actuator	Pulse_(mSec.)	100	
37		22	Delay_(Sec.)		1	
38		10	EXPO_Actuator	Set_to_Open	0	
39		8	MFC_Flow	Set_to_Value	200	
40		22	Delay_(Sec.)		10	
41		24	Loop_n_Times	Number	1	**VLoop**
42	**BiLoop**	8	MFC_Flow	Set_to_Value	40	
43		8	MFC_Flow	Wait_Until_<	45	
44		11	N2_Inject		0	
45		10	EXPO_Actuator	Set_to_Closed	0	
46		22	Delay_(Sec.)		0.2	
47	BiPH3	14	ALD_3_Actuator	Pulse_(mSec.)	2000	
48		22	Delay_(Sec.)		1	
49		10	EXPO_Actuator	Set_to_Open	0	
50		8	MFC_Flow	Set_to_Value	200	
51		22	Delay_(Sec.)		10	
52		8	MFC_Flow	Set_to_Value	40	
53		8	MFC_Flow	Wait_Until_<	45	
54		10	EXPO_Actuator	Set_to_Closed	0	
55		22	Delay_(Sec.)		0.2	
56	water	16	ALD_5_Actuator	Pulse_(mSec.)	25	
57		22	Delay_(Sec.)		1	
58		10	EXPO_Actuator	Set_to_Open	0	
59		8	MFC_Flow	Set_to_Value	200	
60		22	Delay_(Sec.)		10	
61		24	Loop_n_Times	Number	1	**BiLoop**
62		24	Loop_n_Times	Number	4000	**DepoLoop**
63		22	Delay_(Sec.)		7200	
64		8	MFC_Flow	Set_to_Value	5	

References

(1) Shanthi, E.; Dutta, V.; Banerjee, A.; Chopra, K. L. Electrical and Optical Properties of Undoped and Antimony-doped Tin Oxide Films. *J. Appl. Phys.* **1980**, *51*, 6243–6251.

(2) Kasar, R. R.; Deshpande, N. G.; Gudage, Y. G.; Vyas, J. C.; Sharma, R. Studies and Correlation among the Structural, Optical and Electrical Parameters of Spray-

Deposited Tin Oxide (SnO2) Thin Films with Different Substrate Temperatures. *Phys. B Condens. Matter* **2008**, *403*, 3724–3729.

(3) Aboaf, J. A.; Marcotte, V. C.; Chou, N. J. Chemical Composition and Electrical Properties of Tin Oxide Films Prepared by Vapor Deposition. *J. Electrochem. Soc.* **1973**, *120*, 701.

(4) Davazoglou, D. Optical Properties of SnO2 Thin Films Grown by Atmospheric Pressure Chemical Vapour Deposition Oxiding SnCl4. *Thin Solid Films* **1997**, *302*, 204–213.

(5) Stefik, M.; Cornuz, M.; Mathews, N.; Hisatomi, T.; Mhaisalkar, S.; Grätzel, M. Transparent, Conducting Nb:SnO2 for Host–Guest Photoelectrochemistry. *Nano Lett.* **2012**, *12*, 5431–5435.

(6) Elam, J. W.; Baker, D. A.; Hryn, A. J.; Martinson, A. B. F.; Pellin, M. J.; Hupp, J. T. Atomic Layer Deposition of Tin Oxide Films Using Tetrakis(Dimethylamino) Tin. *J. Vac. Sci. Technol. A Vacuum, Surfaces, Film.* **2008**, *26*, 244.

(7) Lamm, B.; Trześniewski, B. J.; Döscher, H.; Smith, W. A.; Stefik, M. Emerging Postsynthetic Improvements of BiVO 4 Photoanodes for Solar Water Splitting. *ACS Energy Lett.* **2018**, *3*, 112–124.

APPENDIX D:
SUPPLEMENTAL INFORMATION TO CHAPTER 4

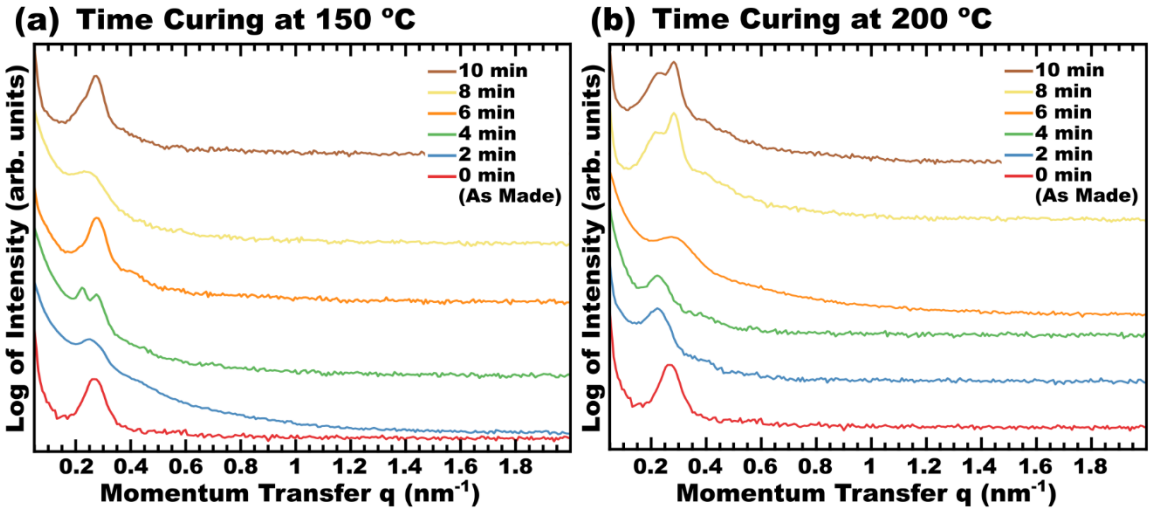

Figure D.1. Effect of curing time at (a) 150 or (b) 200 ºC on RF resin morphology. PEO-*b*-PHA as template; samples from CM05.

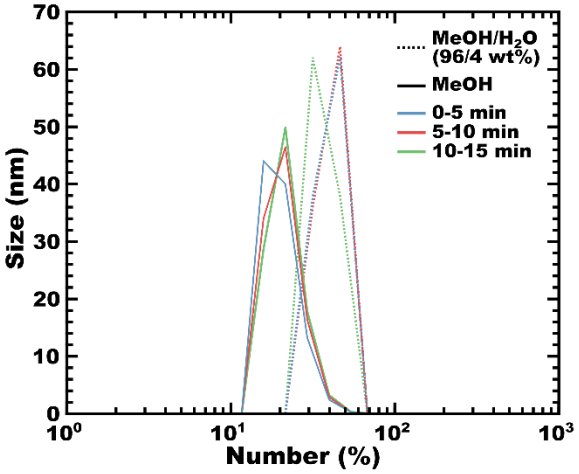

Figure D.2. Effect of dispersing solvent on PEO-*b*-PMMA micelle size. Solid lines: dry methanol – Dashed lines: MeOH/H_2O (96/4 wt%) mixture.

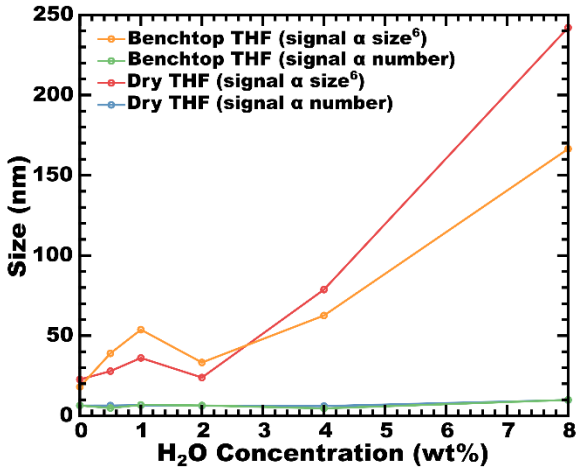

Figure D.3. Effect water concentration in THF on polymer micelle size distribution.

Selected Experiments from CPMT with PEO-*b*-PHA

CM01

Spin coated solutions were mixed by combining two solutions: one of polymer in methanol and the other of resorcinol in methanol. This combined solution was divided into four aliquots, where different amounts of 0.25 M HCl in methanol (made by diluting concentrated HCl with methanol) were added. Solutions were sonicated 10 min. Formaldehyde (37 wt% aqueous) was added immediately prior to spin coating.

Spin coating took place in a home-built humidity-controlled spin coater at ~15% relative humidity (RH) at 500 rpm for 20 s. Spin-coated substrates (glass coverslips) were aged in air at room temperature.

Drop casting took place in air at room temperature. Two drops of sample solution were applied to glass coverslips; substrates dried at room temperature.

It was noted that samples became pinkish-red after ~2 min post spin coating. Drop-cast samples took longer to dry and set (becoming red/pink after ~23 min). Spin coated samples had better clarity in general compared to drop cast samples.

All films were set to age at 150 ^{o}C for 20 h while flowing 15% RH.

CM05

Solutions were made following the procedure described above. This experiment looked at aging parameters; in particular, (i) the effect of holding a sample in the spin coater (under controlled humidity) for a set time prior to aging and (ii) aging temperature (either 150 or 200 ^{o}C) overnight.

CB01 and CB02

Polymer was dissolved in t-butanol and combined with HCl. Samples of resorcinol were weighed out to separate vials and dissolved in aliquots from the butanol solution. It was noted that the resorcinol was difficult to dissolve in butanol, requiring 10 min sonication. Formalin (37 % aqueous formaldehyde) was added to the solutions 30 min before freesing in a dry ice/isopropanol bath. Frozen solvent was sublimed by placing frozen solutions in a room temperature vacuum oven overnight.

CB15 and CB18

CB15 examined the effect of gel temperatures at 80 or -4 ^{o}C over 24 h. Polymer was dissolved in solvent and HCl; this solution was used to dissolve resorcinol, with sonication for 15 min to dissolve resorcinol. Formaldehyde (37% aq) was added prior to dividing the solution into two vials for gelling.

CB18 examined the effect of higher weight-contents of water in solution. The standard water content prior to this test was 10 wt% (prior to formalin addition) and 26 wt% (after formalin addition). Tested contents here were 10, 13.5, and 17 wt% (26, 28, and 31 wt% after formalin addition). As before, polymer was dissolved in butanol and HCl. This polymer/butanol solution was used to dissolve resorcinol (sonication 15 min). After adding formalin, solutions were gelled at 60 or 80 ^{o}C.

CB08

This experiment examined the effect of changing the material to template (M:T) mass ratio on the resulting material structure from a range of 0.2-3.0. Material is resorcinol and template is polymer AK2 from Kayla Lantz.

For M:T series, two stock solutions – one for material, the other for template – are mixed at the desired ratios. The template stock solution (made up of polymer at 0.15 g/ml, butanol, and water) was varied while the material stock was held constant (resorcinol, HCl, butanol, and water). The water content of both solutions was kept as similar as possible to maintain a constant water content for all ratios.

CB08 stock solutions started at 10 wt% water, R:C ratio of 4.00:1, R:F ratio of 1:3.00, and resorcinol concentration of 0.60 M.